UNIVERSITY OF SOUTHAMPTON

FACULTY OF ENGINEERING, SCIENCE AND MATHEMATICS

School of Chemistry

Rapid Screening of Proton Exchange Membrane Fuel Cell Cathode Catalysts

by

Piotr Marcin Kleszyk

Thesis for the degree of Doctor of Philosophy

June 2009

UNIVERSITY OF SOUTHAMPTON

ABSTRACT

FACULTY OF ENGINEERING, SCIENCE AND MATHEMATICS

School of Chemistry

Doctor of Philosophy

RAPID SCREENING OF PROTON EXCHANGE MEMBRANE FUEL CELL CATHODE CATALYSTS

By Piotr Marcin Kleszyk

One of the major bottlenecks in catalyst development for proton exchange membrane fuel cell (PEMFC) is the lack of fast high-throughput testing methods. Fast screening techniques enable a large number of catalysts to be tested in a relatively short time under the same conditions.

This project was focused on developing systems for screening catalysts used for the oxygen reduction reaction (ORR) at the cathode of PEMFCs. The first system developed was the 64 channel pin electrode array, using liquid electrolyte. The developed method improved both the quality and reproducibility of the data and has been used to rank catalyst samples, as well as to optimize loadings and the preparative methods of inks. The second system developed was a 25 channel array fuel cell, which operated under conditions analogous to real fuel cell environments. Both methods allowed trends in characteristics and activities of a series of catalysts to be established more rapidly than individual single-electrode methods such as half cell, rotating disc electrode (RDE) or fuel cell. The results from the two high-throughput methods are compared to those of the single channel systems. The mass and specific activities towards reduction of oxygen were studied using a series of Pt/C and PtCo/C catalysts. The catalytic properties of the Pt based carbon-supported catalysts were related to their structure e.g. particle size and lattice parameter, which were obtained mainly using X-ray diffraction (XRD). It was found that the results acquired using parallel screening methods were similar to those collected with a RDE and a fuel cell.

The thesis concludes with suggestions regarding the future improvement/development of high-throughput techniques. For the 64 channel array system the problem associated with the corrosion of the components should be solved. Similarly, the major changes for the array fuel cell would be to modify a heating system and further development of the anode flow field.

TABLE OF CONTENTS

DECLARATION OF AUTHORSHIP

I, **Piotr Marcin Kleszyk** declare that the thesis entitled:

Rapid Screening of Proton Exchange Membrane Fuel Cell Cathode Catalysts

and the work presented in it are my own. I confirm that:

- This work was done wholly or mainly while in candidature for a research degree at this University;
- Where any part of this thesis has previously been submitted for a degree or any other qualification at this University or any other institution, this has been clearly stated;
- Where I have consulted the published work of others, this is always clearly attributed;
- Where I have quoted from the work of others, the source is always given. With the exception of such quotations, this thesis is entirely my own work;
- I have acknowledged all main sources of help;
- Where the thesis is based on work done by myself jointly with others, I have made clear exactly what was done by others and what I have contributed myself;

Signed: _____

Date: June 2009

ACKNOWLEDGEMENTS

First of all, I would like to thank my supervisor, Professor Andrea Russell, for all the advice, guidance, motivation, encouragement and support she has provided for me throughout the period of my PhD. In addition, I would like to thank my advisor, Professor John Owen, whose feedback and great attitude helped me with the completion of my project. This study was mainly made in collaboration with Johnson Matthey, and for this reason I would like give special thanks to all of those from JM Technology Centre who helped me: Dave Thompsett, Sarah Ball, Brian Theobald, Ed Wright and Sarah Hudson.

I am also grateful to the NuVant Systems team, especially Eugene Smotkin whose knowledge amazed me, and to those with whom I was working, Tim Hall and Corey Grace. For the good job they have done I must thank the staff of the mechanical workshop, Alan Glass and the glassblowers, Przemysław Tryc and Lee Mulholland, who built and made my cell components. Moreover, thanks to the staff from the school office for making my life easier and for creating a good working environment. I would like to thank the members of the Russell group. Firstly, thanks to Gaël for the enthusiasm he contributes in every aspect of our student life, including after work activities. I would like to thank Peter, whose accuracy and teaching skills influenced my life at the beginning of my PhD. He introduced me to the world of football on Southampton Common, which became part of my life for nearly four years. Thanks also to Praba, who has made me feel so comfortable. Many thanks to former members: 'Lovely' Suzanne, Colin 'The King', Dave 'The Quin', Dai, Li, Helen, 'Fabulous' Fab and Katie. I would also like to thank the rest of the Russell group members: Stephen, Jon, Anna, Beatrice and Noelia. Thanks to all my friends for making my time here a really pleasant experience.

Finally, I would like to thank my parents and my brothers for their support and love.

LIST OF SYMBOLS

a	lattice parameter
c_O^σ	concentrations of O species (mol cm^{-3})
c_R^σ	concentrations of R species (mol cm^{-3})
c^∞	the concentration of electroactive species in the bulk solution (mol cm^{-3})
D	the diffusion coefficient ($cm^2\ s^{-1}$)
D_O	the diffusion coefficient of O ($cm^2\ s^{-1}$)
d	distance between the planes (spacing of the atoms)
$E°$	standard potential (V)
E_e^O	the standard reduction potential for the redox couple (V)
ECA	the electrochemical area ($m^2_{Pt} g^{-1}_{Pt}$)
$EPSA$	the effective platinum surface area ($cm^2_{Pt} cm^{-2}$)
F	Faraday's constant (96485 C mol^{-1})
$Flux$	the flux of species to the electrode surface
h, k, l	crystallographic planes parameters indexes
I	electrode current density (A m^{-2})
I_O	exchange current density (A m^{-2})
I_L	limiting current density (A cm^{-2})
I_k	the true kinetic current density (A cm^{-2})
k	constant dependent on the crystalline shape and in the way which $\beta_{0.5}$ and L are defined, and is usually assigned the value 0.9
$\vec{k}$	the rate constant for the electron transfer reaction
k_m	the mass transport coefficient
L	the effective crystal (particle size) diameter (nm)
n	the number of electrons transferred
n	an integer
Pt_{area}	Platinum real surface area (cm^2_{Pt})
R	gas constant (8.314 J $mol^{-1}\ K^{-1}$)
R_T	resistance (Ω)

r_i	ionic resistance (Ω)
r_e	electronic resistance (Ω)
r_c	contact resistance (Ω)
T	the temperature (K)
x	the distance from the electrode surface (mm)
α	α - known as transfer coefficient, which is dimensionless (subscripts $_A$ and $_C$ indicate anodic and cathodic processes, respectively).
$\beta_{0.5}$	the width of the diffraction peak at half height, measured in radians
η	overpotential $E - E_e$ (V)
η_O	activation overpotential (V)
η_{iR}	ohmic overpotential (V)
$\eta_{concentration}$	mass transport overpotential (V)
θ	angle of incidence (theta)
θ_o	the position of peak maximum
λ	the wavelength of incident X-ray beam (nm)
υ	kinematic viscosity ($cm^2\ s^{-1}$)
ω	the angular rotation rate of the disc (s^{-1})

Contents

Chapter One: Introduction

The fuel cell is an electrochemical device for the direct conversion of the chemical energy of a fuel into electricity. This chapter will briefly review fuel cell technology and explain the main principles of operation. The major parameters which determine properties of the catalysts that make up the anode and cathode of low temperature fuel cells will be reviewed. Moreover, the methods of catalyst screening used in PEMFC testing will be introduced.

1 General introduction

In this century, our civilisation faces decreasing resources of fossil fuels and uranium ores, which are natural non-renewable sources of energy. At the moment, to maintain or increase the level of our economy and lifestyle a substitution of engines dependent on fossil fuels needs to be performed. For sure, renewable energy such as wind, solar, tidal, biomass and geothermal energy could be a great substitution for current conventional fossil fuels and nuclear power stations. One of the most promising replacements of combustion engines for cars is the fuel cell. The proton exchange membrane fuel cell (PEMFC) is the main type developed for this purpose. There is no doubt that the main source of hydrogen essential in fuel cell technology comes from hydrocarbons. However, fossil fuels can be used more efficiently in fuel cells than in combustion engines. Hydrogen can also be produced from water using renewable methods such as hydroelectric turbines, windmills, solar panels and biogas instead of burning fossil fuels. Unfortunately, the energy systems based on renewable sources do not produce hydrogen locally for the customer. For this reason, hydrogen must be stored as a buffer between generation and the costumer. Widespread use of PEMFCs must overcome this problem.

The mass production of fuel cells currently faces market barriers due to their early stage of development, but the potential exists for them to be more economically viable in the near future. Dispersed and efficient power production and the extremely low emission electric vehicles are the main points dominating the present applicability scenario of fuel cells. These aspects of long-term energy storage are important for the use of fuel cells in smaller stationary applications, remote locations and households. Fuel cells have a number of social and environmental qualities. Fuel cells can meet the very important criterion of zero CO_2 emission (at least locally). This factor plays a significant role in fuel cell development, putting the technology in front of others in consideration of environmental protection and the prevention of the climate change process.

The fuel cell concept was first introduced in 1839 by Sir William Robert Grove, who realized that reversing the electrolysis process could result in electricity production [1]. Grove's discovery was not noticeable in an era of fossil fuelled engines until the time when NASA pushed the technology forward in the 1960s. Due to their relatively low weight, complexity and low toxicity, fuel cells were used in space shuttles to produce electricity, heat and water.

All types of fuel cells operate on the same basic concept of the electrochemical reaction of fuel and oxygen to produce water, direct current electricity, and heat. Essentially fuel cells consist of an anode, the electrolyte, a cathode, the external electrical circuit, and a fuel/air supply. Fuel is delivered to the anode and oxygen or air is delivered to the cathode. Ions migrate through the electrolyte and electrons flow through the external circuit, creating the electrical current.

The five major types of fuel cells are the alkaline fuel cell (AFC), phosphoric acid fuel cell (PAFC), molten carbonate fuel cell (MCFC), solid oxide fuel cell (SOFC), direct methanol fuel cell (DMFC) and polymer electrolyte membrane fuel cell (PEMFC).

Polymer electrolyte membrane fuel cells (PEMFC) are described in detail in section 2 of this chapter. According to the anode fuel provided PEM FCs can be divided into three types: pure hydrogen, reformate (involving a hydrogen reforming step allowing liquid hydrocarbons to be used as a fuel) and the direct methanol fuel cell (DMFC) with methanol as a fuel.

1.1 Environmental aspects

Fuel cells are a super efficient, environmentally friendly source of energy. At the moment, the high emission to the atmosphere of greenhouse gases by combustion engines used in cars needs to be prevented, otherwise climate change could be irreversible. Emissions of pollutant gases are virtually zero during the operation of all fuel cell types. Unfortunately, while fuel cell cars are powered by hydrogen obtained using gasoline, the use of reformer technology to produce H_2 will have little or no benefit in reduced greenhouse gases emissions. On the other hand, methanol fuel cells may produce much less carbon dioxide and emissions could even drop by 40 % when cars use hydrogen extracted from natural gas. Current research shows that fuel cells could use hydrogen produced by an electrolysis

process that is powered by electricity derived from renewable biomass [2], wind, solar [3], and water sources. If these solutions were implemented over a long period of time, the environmental benefits would be even greater. In that case, the only outputs of fuel cells would be electricity, heat, and water vapour without CO_2, SO_x, or NO_x emissions.

1.2 Applications

In theory, fuel cells can be used with all the devices that consume electricity. Applications of fuel cells could be classified as being stationary or portable. High temperature fuel cells such as molten carbonate (650 °C) and solid oxide (1000 °C) are used mainly in stationary applications. Conversely, low temperature alkaline (80 °C) and PEMFC (80 °C) are used mostly for remote or portable applications.

High temperature fuel cells can be applied in regions which are placed far away from a power supply source, such as rural areas. These types of fuel cells are built as stationary power units. Additionally, high temperature fuel cells are used as an emergency source of energy for buildings which demand constant electricity supply such as hospitals, military sites etc. Any type of fuel cell can be used as auxiliary power. For example, when wind turbines do not operate due to periodic lack of wind, fuel cells could generate electricity instead. Similarly, fuel cells can be applied with solar panels at times when clouds obscure the sun.

Recently much more attention has been put into the development and applications of low temperature fuel cells, especially the PEMFC. An advantage of the PEM fuel cell system is its light weight and compactness. Importantly, the parts of the fuel cell do not move during operation, which helps to increase efficiency. Moreover, it operates at low temperatures, below 110 °C, and can cover a large power range. For this reason, PEM fuel cells have the highest energy density of all fuel cell types. Due to the nature of the reaction, they have less than one second start up time, so PEMFCs have been favoured for electric and hybrid vehicles (cars, boats, buses, submarines), portable power, spacecraft, remote weather stations, and backup power applications. They could also be used as domestic appliance home fuel cells.

On the other hand, the DMFC, which is a modification of the PEMFC, displays low operating temperature and no requirement for a fuel reformer. These features make the DMFC an excellent candidate for very small to medium sized portable electronic equipment applications, such as cellular phones, notebook computers, portable charging docks and other consumer products, up to power plants.

2 Proton Exchange Membrane Fuel Cells (PEMFCs)

Amongst all types of fuel cells, PEMFCs are the most promising for the future. The advantage is that they operate at lower temperature. The PEMFC was first developed by General Electric in the United States in the 1960s for use by NASA in spacecraft [4]. This type of fuel cell is also known as the polymer electrolyte membrane fuel cell because it consists of a proton conducting membrane, such as a perfluorinated polymers with sulfonate fixed ionic groups (Nafion®) as the electrolyte, which has good proton conducting properties. The membrane is sandwiched between two Pt based impregnated porous electrodes. At the back of both anode and cathode electrodes, gas diffusion layers (GDL) are coated with a hydrophobic polymer such as Teflon. This compound forms a waterproof coating which provides gas diffusion channels to the catalyst layer. Within the cell, hydrogen oxidized at the anode provides protons and releases electrons which pass through the external circuit to reach the cathode. The protons together with water molecules diffuse through the membrane to the cathode. The oxygen reacts with protons while picking up electrons and finally forms water.

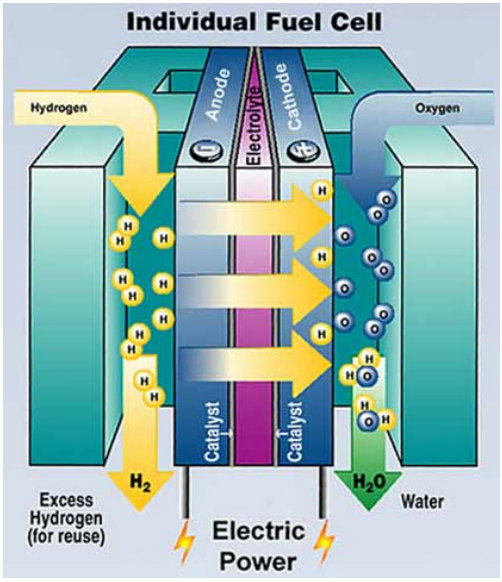

Figure 1 Schematic of PEM fuel cell [5]

As can be seen from Figure 1, the electrodes are porous; hence, they are permeable to gas. All three phases are required for the reaction to occur: the liquid phase (ion conductor – acid), the solid phase (electron conductor – Nafion®), and the gas phase (electrode pores).

2.1 PEM Fuel Cell reactions

The reactions occurring in a PEMFC are described in this section. The hydrogen oxidation reaction takes place at the anode electrode and is presented in Equation 1:

$$H_2 \rightarrow 2H^+ + 2e^- \qquad E° = 0\,V \; vs.\; SHE \qquad \textbf{Equation 1}$$

Note that the fuel cell operates using pure H_2. Sometimes the hydrogen is contaminated with CO. Only a few ppm of carbon monoxide may be tolerated by the Pt catalysis at its operating temperature of 80 °C. Removal of the unconverted CO to ppm levels is necessary to generate the pure hydrogen required as a fuel by the cell. The influence of CO poisoning at the anode could significantly decrease performance. The possible solutions of this problem will be discussed in section 3.5 of this chapter.

The oxygen reduction reaction (ORR) is an electrochemical reaction that takes place at the cathode. The performance of a wide variety of electrocatalysts towards the ORR has been studied extensively [6]. However, the detailed mechanism of this process is still unclear. One of the problems with the reduction of oxygen is that there are multiple reaction pathways, as depicted in Figure 2

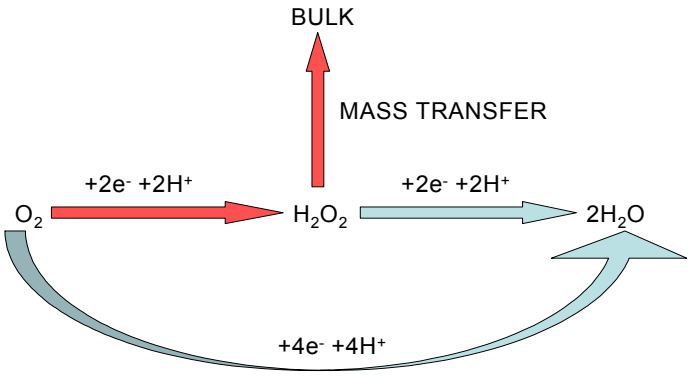

Figure 2 The different reaction pathways for the ORR in acidic solution.

For the direct four electron pathway, oxygen and protons are converted to water in a single step (Equation 2).

$$O_2 + 4H^+ + 4e^- \rightarrow 2H_2O \qquad E° = 1.23\,V \; vs.\; SHE \qquad \textbf{Equation 2}$$

The standard potentials $E°$ are reported with respect to the standard hydrogen electrode (SHE) at 25 ^{o}C. Formation of water is found without any other intermediates, which can appear in this reaction. [7]

In the second route, the reduction of oxygen proceeds in two sequential steps. Hydrogen peroxide is created in the first step (Equation 3) and is a distinctive intermediate of this reaction.

$$O_2 + 2H^+ + 2e^- \rightarrow H_2O_2 \qquad E° = 0.67\,V \; vs.\; SHE \qquad \textbf{Equation 3}$$

The hydrogen peroxide can subsequently be converted into water in a second $2e^-$ transfer reaction (Equation 4):

$$H_2O_2 + 2H^+ + 2e^- \rightarrow 2H_2O \qquad E° = 1.77\,V \; vs.\; SHE \qquad \textbf{Equation 4}$$

Peroxide can also decompose to produce water and oxygen via a non-Faradaic disproportionation reaction (Equation 5):

$$2H_2O_2 \rightarrow 2H_2O + O_2 \qquad \textbf{Equation 5}$$

The total cell summary reaction is (Equation 6):

$$2H_2 + O_2 \rightarrow 2H_2O \qquad E° = 1.23\,V \; vs.\; SHE \qquad \textbf{Equation 6}$$

2.2 Types of fuel for PEM FC

2.2.1 Pure Hydrogen

This type of fuel cell runs on pure hydrogen which derives straight from water hydrolysis. The main obstacle for an application of this type is hydrogen storage. At the moment four types of hydrogen storage are in general use [8]. First there is high pressure storage, which demands large and heavy vessels and is impractical in small cars. The second type of storage stores liquefied hydrogen and the disadvantage is that it demands large amounts of energy to turn gaseous hydrogen into the liquid phase. The third type is physical hydride storage, which stores hydride in alloys or inter-metallic compounds. The fourth type is chemical metal hydride storage. Unfortunately, the best physical and chemical hydride storage cannot compete with compressed hydrogen storage. As is generally known, hydrogen is highly explosive in the presence of oxygen if a source of ignition is present. For this reason, this is a huge disadvantage in applications of pure hydrogen.

2.2.2 Reformate

In this type of fuel, liquid hydrocarbons are used instead of pure hydrogen as the main source of energy. In contrast to hydrogen, this option employs reforming steps to produce reformate, which is mainly hydrogen, but also contains quite large amounts of CO and CO_2

and sulphur compounds. If a hydrocarbon fuel such as natural gas is used as a fuel, reforming of the fuel proceeds by the reaction (Equation 7):

$$CH_4 + H_2O \rightarrow 3H_2 + CO$$ **Equation 7**

(in the case of natural gas), followed by shifting of the reformate by the reaction (Equation 8):

$$CO + H_2O \rightarrow H_2 + CO_2$$ **Equation 8**

This process helps to avoid dangerous hydrogen storage and produces fuel on demand. The disadvantage of this fuel is that carbon monoxide can poison the anode, thus lowering performance. Moreover, any sulphur compounds present in a hydrocarbon fuel could be dangerous for fuel cell performance and have to be removed prior to use in the reformer fuel.

2.2.3 Methanol

PEM fuel cells which use methanol instead of hydrogen are called direct methanol fuel cells (DMFC). This type of fuel cell was developed in the early 1990s [9]. Improvements in catalysts and other recent developments have increased power tremendously over time and efficiency may eventually reach 40 % [10]. These cells have been tested in a temperature range from about 50 °C – 100 °C [10]. DMFCs are similar to the PEMFCs in that the electrolyte is a polymer and the charge carrier is the hydrogen proton. However, at the anode the methanol (CH_3OH) is oxidized in the presence of water, generating CO_2, hydrogen ions and the electrons (Equation 9).

$$CH_3OH + H_2O \rightarrow 6H^+ + 6e^- + CO_2$$ **Equation 9**

Similarly, as in hydrogen fuel cells, the ions migrate through the membrane towards the cathode and the electrons travel throughout the external circuit generating electricity.

3 PEM FC Structure

PEM fuel cells consist of a stacked arrangement of bipolar plates, between which membrane electrode assemblies (MEAs) are sandwiched. The main role of the bipolar plate is to supply gas and conduct electricity. Fuel cell stacks are incorporated into fuel cell systems which broadly consist of one or several stacks, fuel and air (oxygen) humidifiers, fuel reformers, recycling route, afterburner, control system, power electronics including DC-AC inverter, and many other components.

3.1 The Fuel Cell Stack

The schematic stack is shown in Figure 3. It consists of two end plates and numerous bipolar plates with gas flow channels machined on both sides. Between the bipolar plates and two endplates, the membrane electrode assemblies (MEAs) are sandwiched. A MEA consists of a polymer electrolyte membrane which is covered with reaction layers on both faces, namely the electrodes. The first reaction layer is designed as a Pt-based anode electrocatalyst for the oxidation of hydrogen. The second reaction layer is designed for the reduction of oxygen as a cathode, similarly using Pt based electrocatalysts. Next to the electrodes are positioned gas diffusion layers. They are made of carbon fibre paper or carbon fibre cloth. These carbon materials facilitate good access by the reaction gases to the electrodes and efficient current conduction after the potential is applied to the electrodes.

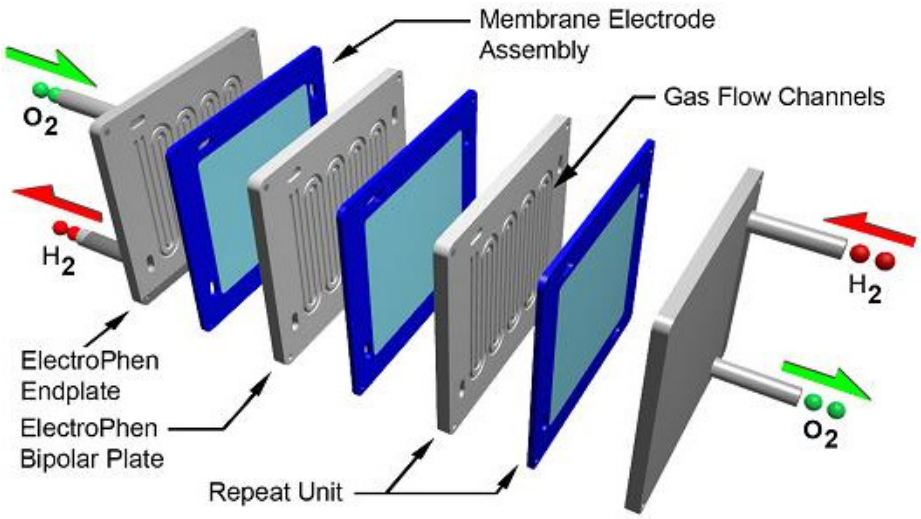

Figure 3 Schematic of PEMFC with serpentine flow fields. [11]

3.2 The Bipolar Plate

Traditionally, graphite was used as the material to produce the plates in PEM FC stacks, generally referred to as bipolar (anode/cathode) plates or separator plates. Graphite's advantages are simplicity of machining by automated process, light weight, and good electrical conduction [12]. These days, graphite has been replaced by compounds that contain a high percentage of carbon or graphite, and a polymer resin. Metal plates may be possible for application as well. However, materials used and manufacturing techniques vary a lot between producers.

The major functions of bipolar plates in the fuel cell are to support the MEA and make electrical connections in the stack. The other main roles are associated with flow field channel design. The functions are thermal management, water management, and supply of humidified reactant gases. Performance improvement in PEMFCs is based on minimization of all transport resistances, which largely depend on the design of gas flow fields. A typical problem in PEMFCs is water accumulation in the flow field. This problem needs to be solved by the appropriate geometry of the channels. A variety of designs of flow fields have been proposed by many authors [12-14]. Four main types of designs are distinguished: pin type, straight or parallel design, serpentine and interdigitated.

3.3 The membrane

The polymer electrolyte membrane consists of polymer materials which conduct protons. For short these materials are also called ionomers. Normally, a polytetrafluoro-ethylene (PTFE)/fluorovinylether hydrophobic core chain copolymer with attached hydrophilic side chain with acid functions, in particular sulfonic acid groups (SO_3H), is preferably used as ionomer. Such a material is sold by DuPont with the trade name of Nafion® (Figure 4). However, other materials, in particular fluorine-free ionomer materials such as polybenzimidazoles or sulfonated polyether ketones or aryl ketones, can also be used [15, 16].

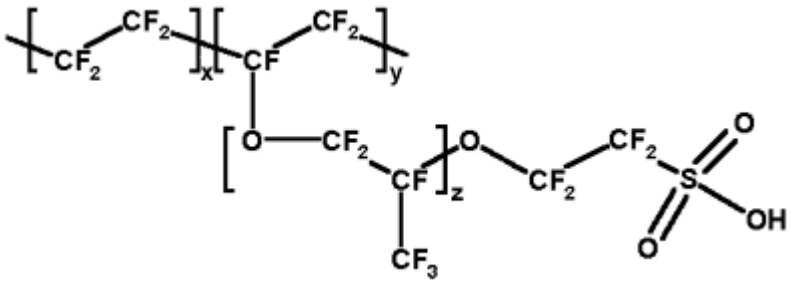

Figure 4 Schematic of Nafion® polymer [17]

The main roles of the membrane are the transport of protons from the anode to the cathode with minimum IR drop, the separation of the hydrogen and oxygen gases from mixing, and to be a support for both anode and cathode catalysts layers. Moreover, the membrane has the function of being an electronically insulating material so that no charge is lost. Furthermore, Nafion polymer is inert for both reducing and oxidizing conditions. The proton conductivity results from hydrophilic sulfonic groups bonded with the polymer chain. The sulfonic

groups create tunnels and protons can 'jump' between fixed ionic groups under the influence of a voltage gradient. Importantly, the polymer has to be sufficiently hydrated to conduct protons.

The initial Nafion membranes were N-115 and N-117 with film thickness of 127 μm and 177 μm respectively. Unfortunately, with time when the electrode platinum loadings were reduced and current density was increased, the resistance of thick membranes caused a decrease in performance and water management problems. Thus, new thinner, extrusion cast membranes, N-105 (a lower equivalent weight (EW), 127 μm), N-1135 and N-1035 (standard and low EW versions with 90 μm thick), N-112 (50 μm) were made. Further development led to the development of even thinner solution cast membranes ranging from 13 to 50 μm [18]. Membrane development focuses on performance, reliability and finally cost. Improvements to membrane mechanical stability, chemical stability and performance at operating temperature up to 110 °C are essential requirements of future development. Polymers with aromatic structures could be the solution because of their greater stability in fuel cell conditions.

3.4 Gas diffusion electrode

Gas diffusion electrodes (Figure 5) are electrodes which play the role of interface as they combine three states: solid, liquid and gaseous. The solid state is the Pt based electrocatalyst supporting electrochemical anode or cathode reactions; the gaseous phase is hydrogen or oxygen gases. The third is the liquid phase; water and electrolyte are needed for the reaction to occur. Usually the catalyst is fixed to porous carbon paper or cloth, so that the liquid and the gas can interact. Moreover, the gas diffusion electrode has to offer an optimal electrical conductivity, in order to enable the transport of electrons without significant resistance to the external circuit.

Pt based catalysts are often used. They have been applied in a form of highly dispersed particles on the surface of a carbon support. The main types of commercially available carbon supports are: Vulcan XC-72R, Tonka, Ketjen Black, Shawinigan Black. Due to high conductivity and stability in fuel cell operational conditions, carbon is a good choice for Pt support. Moreover, it helps to disperse Pt particles uniformly and attain low loading. The average crystallite (particle) size of the platinum group metals supported on carbon is between 1 and 15 nm diameter. The particle size depends on the method of catalyst preparation and the surface area of the carbon support.

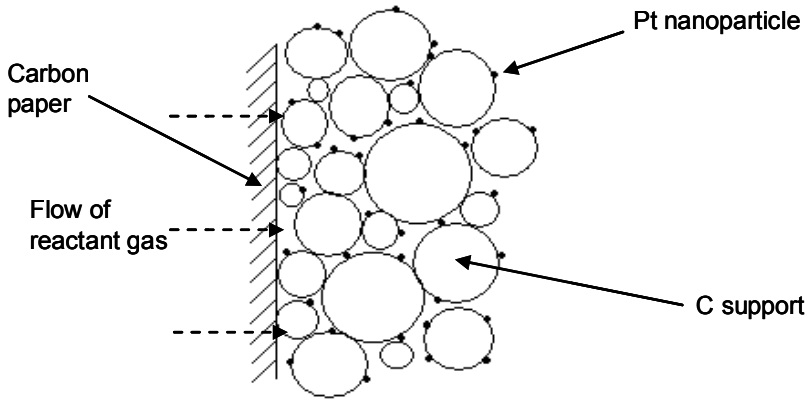

Figure 5 Cross-section through a typical gas diffusion electrode [19].

3.5 Anode catalysts

Anode catalysts are responsible for the hydrogen oxidation reaction (Equation 1) in PEMFCs. Fortunately, the kinetics of this process is very effective and the overpotential needed for the reaction to occur is equal to only 20 mV. The differences in the current densities obtained at this potential mainly depends on the type of catalyst used. The main issue associated with the anode reaction is catalyst poisoning by carbon monoxide, so to face problems connected with this process, some enhancements in the catalyst's structure have been made over last couple of decades [20, 21].

Pt based carbon-supported catalyst is easily poisoned by carbon monoxide even at concentrations of less than 100 ppm [22]. For this reason, the hydrogen fuel should be highly purified by three or more steps. The addition of Ru improves the CO-tolerance of Pt/C [23, 24]; however, a problem with Ru is based on its limited resources. The electrooxidation of adsorbed CO monolayer on catalyst surface occurs at 0.25 V less positive than Pt alone. The reaction occurs in a two step sequence:

$$Ru + H_2O \rightarrow Ru\cdots OH + H^+ + e^- \qquad \textbf{Equation 10}$$

$$Ru\cdots OH + Pt\cdots CO \rightarrow Ru + Pt + CO_2 + H^+ + e^- \qquad \textbf{Equation 11}$$

Some reports have revealed that the addition of Mo [23, 25, 26] or tungstic oxide to Pt/C is also effective for improving CO tolerance; however, the problem of durability still remains. Moreover, Pt alloyed with Co [27], Sn, W [28], and Ge [29] were studied in this process as well. A lot of effort should be dedicated towards developing a CO-tolerant Pt based anode catalyst. A new generation of CO-tolerant catalyst is needed to achieve better efficiency of the anode reaction.

3.6 Problems with ORR – cathode catalysts

Platinum and platinum based bimetallic catalysts are the most commonly used for the ORR at the cathode in the PEMFC. This choice is based on the observation that the kinetics of the ORR are better at Pt based catalysts than at non-Pt catalysts [30]. Unfortunately, the world market price of platinum is consistently very high, as supply is limited. Thus, a balance must be struck between cost and performance. However, even with Pt based catalysts, the slow kinetics of the ORR are a limiting factor in the performance of PEMFCs.

The discovery of improved catalysts for cathode ORR remains a huge challenge for scientists because reduction of oxygen is a far more complicated process than oxidation of hydrogen (see section 2.1). The di-oxygen bond is quite strong and much more energy is required to break it compared to the di-hydrogen bond. The kinetics of the ORR is very sluggish and demands a high overpotential to be applied, of approximately 400 mV (Equation 2). This reaction remains the most important inefficiency in fuel cell technology. To counter this limitation, higher loadings of Pt are used at the cathode than at the anode.

3.7 Improvement of ORR – Possible solutions

In general, three major approaches are under way to address the issues of slow ORR activity. The first point is to reduce Pt loading by the application of carbon support in the PEMFC catalyst layers while maintaining high performance. The second issue is to add non-noble transition elements as a second metal to the Pt catalysts that cost much less and still display the necessary performance level under PEMFC conditions. Finally, the third factor which could be modified is the particle size of platinum catalysts. The rest of the fuel cell components depend mainly on the design and materials used in the production process.

3.7.1 Dispersion of catalyst

The application of high surface area carbon supports is the first approach to achieve high and even dispersion of the platinum particles. In the last two decades, much work has been devoted towards reducing Pt usage in PEMFCs. In this period, the Pt loading in a PEMFC catalyst layer was reduced from 2.0 mg cm $^{-2}$ to 0.4 mg cm^{-2} without any performance loss [30]. However, such a state-of-the-art low temperature PEMFC still cannot reach the requirements for applications in the car industry. At the moment, the target is to increase the catalyst activity by at least four times, which was discussed by Gasteiger et al. [30]. Further research is in progress to reduce the Pt loading to even 0.1 mg cm^{-2}. However, one needs to

bear in mind that this is a huge challenge to get the same durability and performance as for catalysts with 0.4 mg cm^{-2} loading.

3.7.2 Particle size

Several approaches have been taken to enhance the activity of Pt catalysts towards the ORR. Kinoshita [31, 32], focused on the effects of particle size and showed it to be one of the major factors that limit the efficiency of this reaction (Equation 2). In his work, the effects of particle size on the electrocatalyst's activity were illustrated (Figure 6). The trends showed that the activity is changing when particle size changes. Analysis of the data suggested that mass activity (mA mg_{Pt}^{-1}) reaches a maximum for particle diameters between 3 and 5 nm. It is important to mention that the mass activity provides practical information for industry because the cost of the electrodes depends strictly on the mass of Pt used in production.

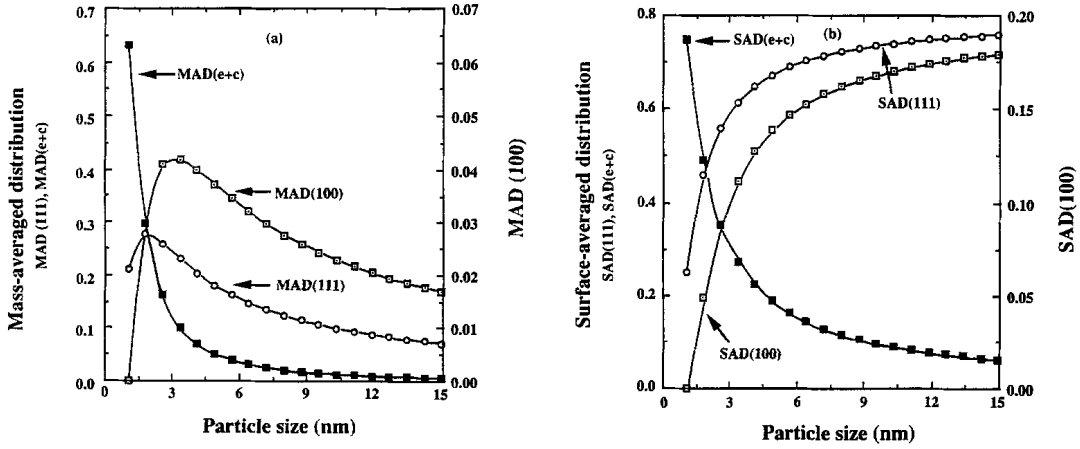

Figure 6 Mass averaged distribution (MAD) and surface averaged distribution (SAD) of atoms on the (111) and (100) crystal faces and on the edge and corner sites of cubo-octahedral (a) MAD (b) SAD. [31]

Kinoshita also showed that the specific activity (mA cm_{Pt}^{-2}) increases as the Pt particle size increases (Figure 6); however, other authors have suggested that specific activity is constant, independent of the Pt particle size [33]. Specific activity reports the results which were obtained as a function of surface area, in other words, as a function of particle size.

From these observations it can be concluded that the ORR is more efficient on ideal ordered crystallographic surfaces and that oxygen reduction on highly dispersed Pt electrocatalysts in acid electrolytes is a demanding or structure-sensitive reaction. Demanding reactions exhibit a specific rate that depends on particle size, and specific sites with special geometric arrangements that are involved as so-called active sites. The larger the particle, the more

active sites appear on the surface of the particle, which enhance efficiency of the reaction for specific activity. Unfortunately, in respect to mass activity, the larger the particle, the more platinum is placed in the bulk of the particle and remains inactive.

3.7.3 Alloy composition

Extensive studies have been made in order to enhance catalyst structure and thus improve catalytic activity. An approach has been to mix the Pt with a second metal to form bimetallic particles. The secondary element can serve as either an inert diluent or as a promoter of the ORR. The latter has been the most common strategy with the secondary metal chosen to decrease the Pt-Pt bond distance, or to increase the potential at which an oxide layer is formed at the surface of the catalyst. The most commonly chosen elements to enhance the efficiency of the ORR are transition elements (metals) such as Mn, Fe [34-39], Cr [40, 41], Co [42-44], Ni [34-36, 45-48], and elements from platinum group metals, Ir [49, 50], and Ru [51]. They could modify the structure and decrease the overpotential. It is commonly thought that changing the catalysts' parameters will resolve this problem. Investigations showed that there are principally three interrelated factors controlling the electrocatalysis of the ORR. The first is due to electronic differences of the vacancies of the Pt d-orbitals. Second is the dependence on the Pt-Pt bond distance, and finally the adsorption characteristics of the oxygenated species from the electrolyte solution Pt-O(H). The interplay of the electronic and structural parameters of Pt and Pt alloy electrocatalysts determines the final electrocatalytic activity of ORR catalysts.

4 PEMFC Challenges

Durability and cost are the major obstacles to commercialization of fuel cells. Similarly, weight, size, and thermal and water management are also difficulties which should be addressed. Fuel cells are far too expensive for most consumers. Manufacturers need to reduce the price of the electrolyte membrane and the catalyst, which is made out of expensive platinum. The durability of fuel cell systems for transportation applications will require about a 5,000-hour lifespan or the equivalent of 150,000 miles. For stationary applications, more than 40,000 hours of reliable operation in a temperature range -35°C to 40°C will be required for market acceptance [52]. Operation at very low temperatures is also problematic because fuel cell systems contain water, which can freeze in cold weather. The size and weight of current fuel cell systems must be further reduced to fit into automobiles [53]. Another problem is to store enough hydrogen on board vehicles. Without sufficient hydrogen fuel, the car cannot travel as far as a traditional fossil fuel vehicle.

Moreover, hydrogen is very dangerous to store. For this reason, safety and risk precautions must be handled. Probably the most difficult element in the whole process of hydrogen delivery to the consumers is building the new facilities and infrastructure that will be required. Unfortunately, this will need significant time and money.

The cost of fuel cells could therefore be drastically reduced by using smaller amounts of carbon-supported Pt in fuel cell electrodes as described in section 3.7.1. Any other catalyst without Pt gave poor results. Pt alloys with transition metals have been used for the ORR (see section 3.7.3) and displayed good results. However, many tests have shown that leaching of the transition metal was a problem for some Pt alloys [46, 54]. The activities of alloy catalysts are good, but at present there is an issue with their durability [55].

Another limiting factor is the effect of H_2O_2 on the stability of polymer electrolyte membranes and this is a critical criterion for the choice of suitable catalysts [56]. The two-electron process produces hydrogen peroxide, which is an unwanted side product in fuel cells, as it reduces power efficiency (see section 2.1). Hydrogen peroxide is corrosive and degrades the PEM (proton exchange membrane) [57]. This is crucial not only for ORR, but also for the anode reaction. At an electrolyte membrane operating temperature above 70 °C, it is difficult to maintain good water management and high water content of the polymer, especially under operation in atmospheric pressure.

5 Project aims

A problem faced by those working in the area of discovering new fuel cell catalyst formulations is the need to screen large numbers of candidate formulations, as the discovery process is still largely empirical. The aim of the work presented in this thesis was to develop and compare several high throughput screening methods. These were applied to the study of oxygen reduction catalysts for PEMFCs. The three methods explored were (i) a rotating disc electrode technique that uses a thin film of the catalyst ink; (ii) a 64 channel pin array electrode cell that also used thin films of catalyst ink, but had higher throughput than the single electrode RDE method; and (iii) a 25 channel membrane electrode assembly fuel cell. Each method was evaluated individually (Chapters 3 through 5) using standard sets of catalysts with known properties, with the aim of providing a recommendation regarding the best screening method (Chapter 6).

6 References

[1] W. R. Grove, Phil. Mag. 14:127 (1839).

[2] P. Westermann, B. Jørgensen, L. Lange, B. K. Ahring, and C. H. Christensen, International Journal of Hydrogen Energy 32:4135 (2007).

[3] J. I. Levene, M. K. Mann, R. M. Margolis, and A. Milbrandt, SOLAR ENERGY 81:773 (2007).

[4] W. E. Rice and D. Bell, in Proceedings of the 7th Intersociety Energy conversion Engineering conference San Diego San Diego, 1972, p. 390.

[5] www.p2sustainabilitylibrary.mil.

[6] B. Sljukic, Banks C. E.,Compton R. G., Journal of the Iranian Chemical Society 2:1 (2005).

[7] K. Swider-Lyons, Bouwman, P. J., Teliska, M. E., Baker W. S., Naval Research Laboratory, Washington, DC, 2004, p. 379.

[8] U. Bossel, B. Eliasson, and T. G., The Future of the Hydrogen Economy: Bright or Bleak?, 2003.

[9] S. Srinivasan, Fuel cells: from fundamentals to applications Springer, 2006.

[10] L. Guzzella and A. Sciarretta, Vehicle Propulsion Systems, Springer, 2007.

[11] www.futureenergies.com.

[12] A. D. James Larminie, Fuel Cell Systems Explained, John Wiley & Sons, 2003.

[13] H. Li, Y. Tang, Z. Wang, Z. Shi, S. Wu, D. Song, J. Zhang, K. Fatih, J. Zhang, H. Wang, Z. Liu, R. Abouatallah, and A. Mazza, Journal of Power Sources 178:103 (2008).

[14] L. Xianguo, Principles Of Fuel Cells, Taylor, 2005

[15] B. Liu, D.-S. Kim, J. Murphy, G. P. Robertson, M. D. Guiver, S. Mikhailenko, S. Kaliaguine, Y.-M. Sun, Y.-L. Liu, and J.-Y. Lai, Journal of Membrane Science 280:54 (2006).

[16] S. Zhong, C. Liu, Z. Dou, X. Li, C. Zhao, T. Fu, and H. Na, Journal of Membrane Science 285:404 (2006).

[17] www.wikipedia.org.

[18] S. Banerjee and D. E. Curtin, Journal of Fluorine Chemistry 125:1211 (2004).

[19] L. P. L. Carrette, K. A. Friedrich, and U. Stimming, ChemPhysChem 1(4):162 (2000).

[20] E. I. Santiago, V. A. Paganin, M. do Carmo, E. R. Gonzalez, and E. A. Ticianelli, Journal of Electroanalytical Chemistry 575:53 (2005).

[21] S. C. Ball and D. Thompsett, in Solid State Ionics - 2002. Symposium (P. Knauth, J. M. Tarascon, E. Traversa, and H. L. Tuller, eds.), Mater. Res. Soc, Boston, MA,, 2003, p. 353.

[22] Y. Yamada, A. Ueda, H. Shioyama, and T. Kobayashi, Applied Surface Science 223:220 (2004).

[23] S. Ball, A. Hodgkinson, G. Hoogers, S. Maniguet, D. Thompsett, and B. Wong, Electrochemical and Solid State Letters 5:A31 (2002).

[24] M. Watanabe and S. Motoo, Journal of Electroanalytical Chemistry 60:275 (1975).

[25] B. N. Grgur, N. M. Markovic, and P. N. Ross, Journal of Physical Chemistry B 102:2494 (1998).

[26] S. Mukerjee, R. C. Urian, S. J. Lee, E. A. Ticianelli, and J. McBreen, Journal of the Electrochemical Society 151:A1094 (2004).

[27] H. Uchida, K. Izumi, K. Aoki, and M. Watanabe, Phys Chem Chem Phys 11:1771 (2009).

[28] S. Ye, M. Hall, H. Cao, and P. He, ECS Transactions 3:657 (2006).

[29] E. M. Crabb and M. K. Ravikumar, Electrochimica Acta 46:1033 (2001).

[30] H. A. Gasteiger, S. S. Kocha, B. Sompalli, and F. T. Wagner, Applied Catalysis B-Environmental 56:9 (2005).

[31] K. Kinoshita, Journal of the Electrochemical Society 137:845 (1990).

[32] N. Giordano, E. Passalacqua, L. Pino, A. S. Arico, V. Antonucci, M. Vivaldi, and K. Kinoshita, Electrochimica Acta 36:1979 (1991).

[33] M. Watanabe, H. Sei, and P. Stonehart, Journal of the Electrochemical Society 135:C157 (1988).

[34] S. Mukerjee, S. Srinivasan, M. P. Soriaga, and J. McBreen, Journal of the Electrochemical Society 142:1409 (1995).

[35] S. Mukerjee and J. McBreen, Journal of the Electrochemical Society 143:2285 (1996).

[36] S. Mukerjee, McBreen, J., Supramaniam S., Investigation on the electrocatalysis for oxygen reduction reaction by Pt and binary Pt alloys: an XRD, XAS and electrochemical study, 1996.

[37] W. Z. Li, W. J. Zhou, H. Q. Li, Z. H. Zhou, B. Zhou, G. Q. Sun, and Q. Xin, Electrochimica Acta 49:1045 (2004).

[38] C. Medard, M. Lefevre, J. P. Dodelet, F. Jaouen, and G. Lindbergh, Electrochimica Acta 51:3202 (2006).

[39] T. Toda, H. Igarashi, and M. Watanabe, Journal of Electroanalytical Chemistry 460:258 (1999).

[40] M. T. Paffett, J. G. Beery, and S. Gottesfeld, Journal of the Electrochemical Society 135:1431 (1988).

[41] P. P. Wells, Y. D. Qian, C. R. King, R. J. K. Wiltshire, E. M. Crabb, L. E. Smart, D. Thompsett, and A. E. Russell, Faraday Discussions 138:273 (2008).

[42] B. C. Beard and P. N. Ross, Journal of the Electrochemical Society 137:3368 (1990).

[43] U. A. Paulus, A. Wokaun, G. G. Scherer, T. J. Schmidt, V. Stamenkovic, V. Radmilovic, N. M. Markovic, and P. N. Ross, Journal of Physical Chemistry B 106:4181 (2002).

[44] E. Antolini, J. R. C. Salgado, M. J. Giz, and E. R. Gonzalez, International Journal of Hydrogen Energy 30:1213 (2005).

[45] S. Mukerjee, S. Srinivasan, M. P. Soriaga, and J. McBreen, Journal of Physical Chemistry 99:4577 (1995).

[46] M. Teliska, V. S. Murthi, S. Mukerjee, and D. E. Ramaker, Journal of the Electrochemical Society 152:A2159 (2005).

[47] L. G. R. A. Santos, C. H. F. Oliveira, I. R. Moraes, and E. A. Ticianelli, Journal of Electroanalytical Chemistry 596:141 (2006).

[48] V. R. Stamenkovic, B. Fowler, B. S. Mun, G. F. Wang, P. N. Ross, C. A. Lucas, and N. M. Markovic, Science 315:493 (2007).

[49] P. Holt-Hindle, Q. F. Yi, G. S. Wu, K. Koczkur, and A. C. Chen, Journal of the Electrochemical Society 155:K5 (2008).

[50] T. Ioroi and K. Yasuda, Journal of the Electrochemical Society 152:A1917 (2005).

[51] T. J. Schmidt, U. A. Paulus, H. A. Gasteiger, N. Alonso-Vante, and R. J. Behm, Journal of the Electrochemical Society 147:2620 (2000).

[52] www1.eere.energy.gov.

[53] www.fueleconomy.gov.

[54] F. H. B. Lima, J. F. R. de Castro, L. G. R. A. Santos, and E. A. Ticianelli, Journal of Power Sources 190:293 (2009).

[55] T. R. Ralph, Hogarth, M. P., Platinum Metals Rev. 46:117 (2002).

[56] U. A. Paulus, T. J. Schmidt, H. A. Gasteiger, and R. J. Behm, Journal of Electroanalytical Chemistry 495:134 (2001).

[57] V. M. Vishnyakov, Vacuum 80:1053 (2006).

Contents

Chapter Two: Experimental Methods - Theory

The basic experimental methods and techniques used in this project will be briefly introduced in this chapter and the theory associated with the measurements will be described.

1 Chemicals and Materials

The catalysts, chemicals and substrates used in these studies are listed in Table 1 along with their suppliers.

Table 1 List of catalysts, chemicals, materials and their suppliers used in this project.

Chemicals / Materials	**Supplier**
20 wt % Pt supported on carbon (XC-72R)	Johnson Matthey
40 wt % Pt supported on carbon	Johnson Matthey
40 wt % Platinum-Cobalt on carbon	Johnson Matthey
Vulcan XC-72R carbon black	Cabot Corporation
Nafion®117 membrane	DuPont Corp.
Nafion® solution 5 wt % in alcohol	Aldrich
TGHP-090 carbon paper	Johnson Matthey
Concentrated sulphuric acid (98%)	Fisher
Chloroform (Lab reagent grade)	Fisher
Propan-2-ol (Lab reagent grade)	Fisher

1.1 Johnson Matthey catalysts

The catalysts and the electrodes used in the experiments carried out during the period of this project were produced and supplied by JMTC (Sonning Common). The catalyst details for the RDE [1-4] and 64 channel array [5] experiments are listed in Chapter 3 (Tables 1, 3 and 4). Similarly, details of the electrodes made out of JM catalysts used in the array fuel cell [6-9] measurements are described in Chapter 5 (Tables 1, 3 and 4).

2 Reference electrodes

2.1 MMS electrode calibration to RHE scale

A mercury mercurous sulphate (MMS), Hg/Hg_2SO_4, was applied as a reference electrode (RE) in both the RDE and 64 channel array measurements. Every time, prior to commencing the experiments, the MMS reference electrode was calibrated against a reversible hydrogen electrode (RHE). The calibration took place in the same electrolyte as in the subsequent experiment was used. In the case of the RDE and 64 channel array, the electrolytes were 1 mol dm^{-3} and 0.5 mol dm^{-3} sulphuric acid, respectively. The potential difference between the MMS and dynamic hydrogen electrode/Pt gauze was measured using Autolab potentiostat (PGSTAT30).

2.2 DHE

A dynamic hydrogen electrode (DHE) was used as a reference electrode (RE) in the array fuel cell experiments. The 103 cm^2 anode (~ 0.4 mg_{Pt} cm^{-2} loading) was used as common counter/reference electrode. Pure hydrogen was supplied to the anode side and the potential difference between hydrogen oxidation reaction at the anode and oxygen reduction reaction at the array cathode was determined.

3 Electrochemical Methods – voltammetric techniques

The main common characteristic of voltammetric methods is that they involve the application of potential (E) to the electrode and at the same time the registration of the resulting current (i) flowing through the electrochemical cell is performed. Sometimes the current is monitored over a period of time (t) instead of applied potential. Thus, all voltammetric techniques can be presented on graphs and described as a function of E, i, and t. The advantages of the various electrochemical methods include excellent sensitivity, the large number of electrolytes and solvents that can be used, the wide range of temperatures that can be applied, and that short analysis times are possible. Moreover, the merit is the ability to estimate the values of unknown kinetic and mechanistic parameters, as well as to develop theories.

The electrochemical cell consists of a working electrode, a reference electrode, and usually a counter (auxiliary) electrode. In principle, an electrode provides the interface across which a charge can be transferred or its effects felt. The reaction takes place on the working electrode. Both the reduction and oxidation of a substance can occur at the surface of a working electrode. Each typical reaction occurs only at the appropriate range of applied potential. The results are the mass transport of new material to the electrode surface and the

generation of a current. Despite the fact that many electrochemical systems look totally different at first glance, the fundamental principles and applications derive from the same electrochemical theory [10].

In voltammetry, the effects of the potential applied to the electrode and the behaviour of the redox current are described by two well-known laws. The first law describes the concentrations of the redox species (Equation 1) at the electrode surface (c_O^σ and c_R^σ) and is described by Nernst equation [10] (Equation 2). The second law relates the electrical current at an electrode to the potential applied and is characterised by the Butler–Volmer equation [10](Equation 3). When diffusion plays a controlling part in the reaction then the current resulting from the redox process is related to the diffusive flux to the concentration field at the electrode–solution interface, and this is described by Fick's law [10] (Equation 4).

The simplified equation for a reversible electrochemical reaction is as follows:

$$O + ne^- \Leftrightarrow R$$ **Equation 1**

The application of a potential E force to the concentrations ratios of O and R at the surface of the electrode (that is, c_O^σ and c_R^σ respectively) can be described with the Nernst equation:

$$E_e = E_e^O + \frac{RT}{nF}\ln\frac{c_O^\sigma}{c_R^\sigma}$$ **Equation 2**

Where: R is gas constant (8.314 J mol^{-1} K^{-1}), T - the temperature (K), n - the number of electrons transferred, F - Faraday's constant (96485 C mol^{-1}), and E_e^O - the standard reduction potential for the redox couple.

If the potential is made more negative the ratio of concentrations c_O^σ and c_R^σ at the surface of the electrode becomes larger (that is, O is reduced) and, conversely, if the potential is made more positive the ratio c_O^σ and c_R^σ becomes smaller (that is, R is oxidized).

For some techniques, it is useful to use the relationship known as the Butler–Volmer equation:

$$I = I_O\left[\exp\left(\frac{\alpha_A nF}{RT}\eta\right) - \exp\left(-\frac{\alpha_C nF}{RT}\eta\right)\right]$$ **Equation 3**

where I - electrode current density (A m^{-2}), I_O - exchange current density (A m^{-2}), η - overpotential, $E - E_e$ (V), α - known as transfer coefficient, which is dimensionless (subscripts $_A$ and $_C$ indicate anodic and cathodic processes, respectively).

The interaction between these processes is responsible for the characteristic features of the voltammograms observed for various techniques. More details regarding the Butler–Volmer equation are described in section 3.3.1.

The third law which could be applied to electrochemical systems is Fick's law. This law postulates that the current flow also depends directly on the flux of species to the electrode surface. When O or R is produced at the surface in electrochemical reaction, the increased concentration of species gives the force for its diffusion toward the bulk of the electrolyte. Conversely, when O or R is reduced or oxidised, the decreased concentration helps the diffusion of new species from the bulk solution to the surface of the electrode.

$$Flux = -D_O \frac{\partial c_O}{\partial x} \qquad \textbf{Equation 4}$$

where D_O - the diffusion coefficient of O and x - the distance from the electrode surface. An analogous equation can be written for the reduced species, R. The flux of O or R at the electrode surface controls the rate of reaction, and thus the current flow in the cell. The current is a quantitative measure of how fast a species is being reduced or oxidized at the electrode surface. In contrast to the diffusion layer, the concentration gradients in the bulk solution are generally small and ionic migration carries most of the current.

3.1 Cyclic voltammetry on smooth Pt

Cyclic voltammetry (CV) has become an important and widely used electroanalytical technique. It is used for the study of redox processes. This technique is based on varying the applied potential at a working electrode at chosen scan rate in both forward (positive going) and reverse (negative going) directions while monitoring the current. The direction of scan could be either towards positive or negative potentials. At a chosen potential value the scan can be reversed and then run in the opposite direction. Depending on the experiment, one full scan cycle, or a series of scans/cycles can be run.

A typical cyclic voltammogram acquired for a platinum disc electrode is shown in Figure 1. Three specific regions [11] can be distinguished in the cyclic voltammogram at particular potentials. The regions are named accordingly (a) hydride region, (b) double layer region (c) oxide region.

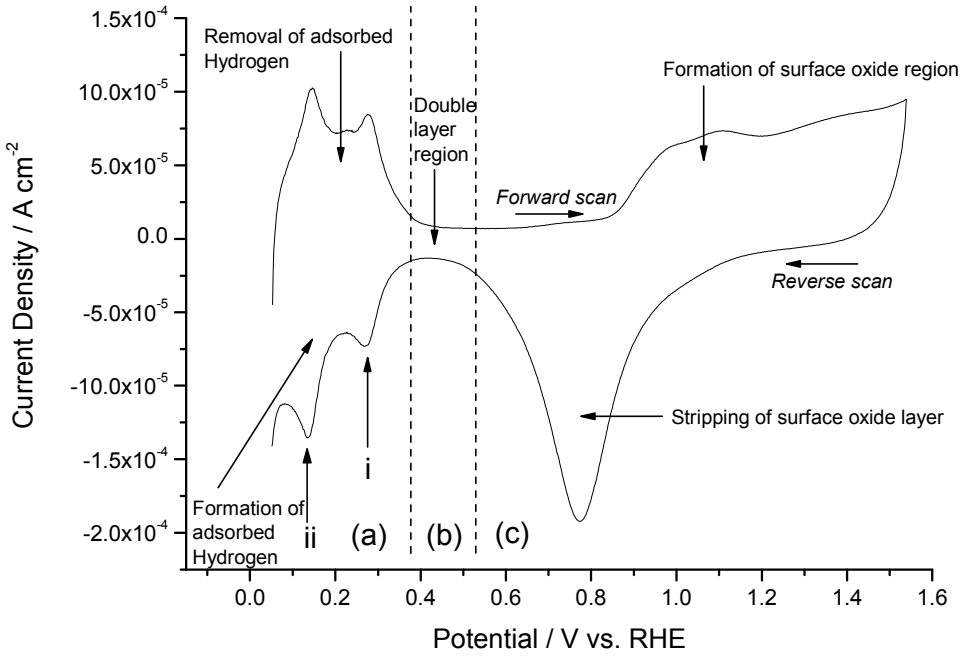

Figure 1 CV of a Pt disc electrode in 1 mol dm^{-3} H_2SO_4 acquired at 100 mV s^{-1} scan rate [11].

Region (a) – Hydride region is responsible for the formation and removal of hydrogen from the surface of the Pt electrode. The peaks in the reverse scan in this region are associated with (i) strongly adsorbed and (ii) weakly adsorbed hydrogen species (Equation 5). Weakly adsorbed means that lower overpotential is required to remove adsorbed hydrogen; conversely, strongly adsorbed hydride species demands higher overpotential. The area of the cyclic voltammogram underneath the adsorption peaks can be used in calculation of the Pt real surface area (see section 3.2). The two peaks in the hydride region collected in positive going scan and positioned at similar potentials as the peaks below correspond to desorption (removal) of adsorbed hydrogen.

$$Pt + H^+ + e^- \rightarrow Pt\cdots H_{ads} \qquad \textbf{Equation 5}$$

Region (b) – Double layer region. In this region, the segregation of positive and negative charges between two phases, the electrode and electrolyte, occur. The double layer is charged at the time when the potential is swept and all the charges from the electrolyte are migrating to the electrode surface. Ideally, after the double layer has been formed, no electron transfer reactions occur at the electrode and the solution is composed only of electrolyte. The current observed in the double layer region of a cyclic voltammogram is proportional to the scan rate. Most experiments in this thesis were performed at 10 mV s^{-1} and 20 mV s^{-1} scan rates. The reason is that, at high scan rates, the double layer current is no

longer negligible in comparison to the Faradaic current (current generated in the reduction and oxidation processes).

Region (c) – Oxide region. The oxide layer is formed (Equation 6 and Equation 7) on the surface of the electrode when the potential is swept from negative to positive potential (forward scan). The onset of the current associated with oxide layer formation is positioned approximately at 0.85 V vs. RHE. The oxide species do not adsorb in a form of monolayer, and much of the oxide species migrate into the bulk of the metal by a place exchange mechanism. On the reverse scan, the oxide species are stripped (reduced) from the surface of the platinum electrode. The area under the oxide peak varies a lot. This depends on how far the potential excursion is toward positive potentials, which corresponds to the time in the oxide region. The longer the time spent, the larger the peak.

$$Pt + H_2O \rightarrow Pt\cdots OH_{ads} + H^+ + e^- \qquad \textbf{Equation 6}$$

$$Pt\cdots OH_{ads} \rightarrow PtO + H^+ + e^- \qquad \textbf{Equation 7}$$

3.2 CO stripping voltammetry

A CO stripping experiment [11, 12] is carried out in order to determine the Pt real surface area of the Pt based electrodes supported on carbon. Normally the solution is saturated with CO and the potential is kept at 0.1 V vs. RHE for 30 minutes. To remove dissolved CO in the electrolyte, the solution is subsequently purged for another 30 minutes by nitrogen. Generally, the scans are run between 0.0 V and 1.2 V vs. RHE. The adsorbed CO forms a monolayer on the platinum electrode surface. When CO is oxidised to CO_2 a noticeable current response occurs in the cyclic voltammogram as shown in Figure 2. The CO stripping CV is shown as a dashed red line. Moreover, the previously discussed desorption peaks of the hydride region do not exist in the first scan. The reason for this is that the platinum active sites were fully covered with CO instead of hydrogen. However, the second scan (solid black line) possesses fully developed hydride region features in the first cycle. Hydrogen desorption peaks appeared because initially CO was stripped from the surface and hydrogen species was adsorbed on the available crystal sites in the second cycle.

$$Pt\cdots CO + H_2O \rightarrow Pt + CO_2 + 2H^+ + 2e^- \qquad \textbf{Equation 8}$$

The charge associated with CO stripping peak presented as a black striped field in Figure 2 can be used to calculate Pt real surface area.

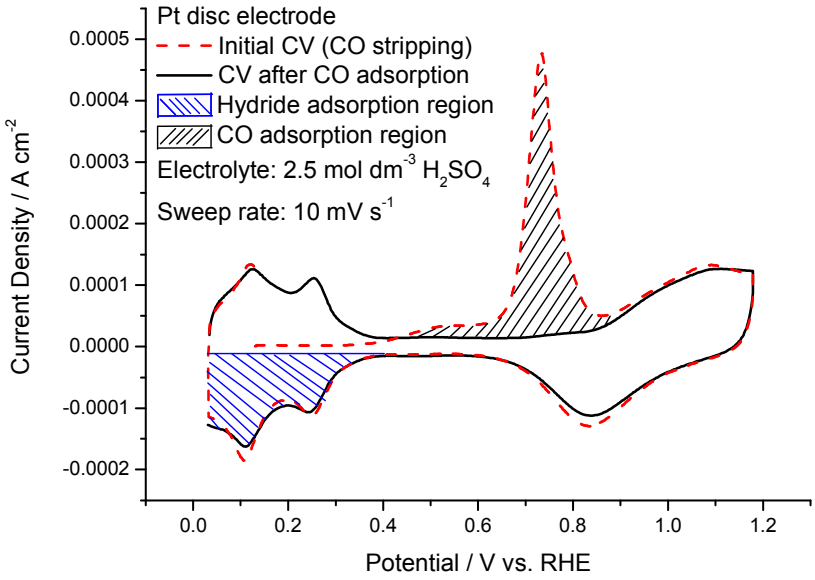

Figure 2 Cyclic voltammograms of a Pt disc electrode before and after CO adsorption [11].

The calculation of Pt real surface area using CO stripping peak charge was determined using Equation 9.

$$\mathrm{Pt}_{\mathrm{area}}\left(cm^2_{Pt}\right) = \frac{\text{Measured CO stripping peak charge}\,(\mu\mathrm{C})}{420\,(\mu\mathrm{C\ cm^{-2}}_{\mathrm{Pt}})} \qquad \textbf{Equation 9}$$

Similarly, the charge associated with hydrogen adsorption region presented as a blue striped area in Figure 2 could be used instead of the CO stripping peak charge to calculate area. The only difference is that the theoretical value of the charge associated with hydrogen monolayer evaluated for hydride adsorption region is half that (210 µC cm^{-2} Pt) of those used for the CO stripping method (420 µC cm^{-2} Pt).

The calculation of Pt real surface area using hydrogen adsorption region charge was determined using Equation 10.

$$\mathrm{Pt}_{\mathrm{area}}\left(cm^2_{Pt}\right) = \frac{\text{Measured H stripping peak charge}\,(\mu\mathrm{C})}{210\,(\mu\mathrm{C\ cm^{-2}}_{\mathrm{Pt}})} \qquad \textbf{Equation 10}$$

In comparison of the two methods of Pt real surface area calculation, it should be mentioned that for some cyclic voltammograms collected using different techniques the hydrogen region is not very pronounced. Thus, is very difficult to accurately estimate the area and to promote the hydride method as the main source of information. Therefore, in some cases the CO stripping method gave more accurate results.

Other important electrochemical parameters which help to compare different methods are the effective platinum surface area (EPSA) [13] and the electrochemical area (ECA) [13]. EPSA is calculated using Pt real surface area divided by the geometric area of the electrode (Equation 11). The information given by this parameter is used to compare Pt real surface area between electrodes of different types and sizes.

$$EPSA(cm^2_{Pt}cm^{-2}) = \frac{Pt_{area}(cm^2_{Pt})}{geometric\ electrode\ area\ (cm^2)} \qquad \textbf{Equation 11}$$

The ECA is determined by dividing the EPSA of the electrode by the Pt loading of the electrode (Equation 12). In this case the values obtained are especially useful in industry. ECA helps to compare results collected using different equipment and methods starting from the RDE, half cell systems and up to real fuel cells.

$$ECA(m^2_{Pt}g^{-1}_{Pt}) = \frac{EPSA(m^2_{Pt}cm^{-2})}{Pt\ loading\ on\ the\ electrode\ (g_{Pt}cm^{-2})} \qquad \textbf{Equation 12}$$

When the raw currents are normalized by the Pt "real" surface area of the electrode, the activities of Pt based electrocatalyst are quoted as specific activity (A cm_{Pt}^{-2}) [14]. Note that specific activities measured by RDE are always quoted as the kinetic current density (I_K) [15]. A second term used by scientists is mass activity (A g_{Pt}^{-1}) [14]. In this case, the raw currents obtained during experiments can be normalized by the mass of Pt of the electrode (Pt loading). The mass activity is very important information for industry as it correlates with the quality and performance of Pt used, which is linked to the cost of the electrode. Moreover, the third way of defining the current is to divide it by the geometric area of the electrode. The term is quoted as current density (A cm^{-2}) [16].

3.3 ORR Polarisation Curve technique

The polarisation curve technique enables the measurement of the ORR catalytic activity of Pt based electrocatalysts. In the experiment, the potential was applied to the electrode and held for some time (typically 60 seconds) at the same constant value until the steady state was reached. Then potential was then stepped to a different potential value (typically 25 mV step) and the potential was held again and the steady state current recorded. The polarisation curve was plotted using only the average value derived from each steady state step. Average value is extracted for each potential step from the very last data points collected when the current value stabilises, which means it achieves a steady state. A schematic polarisation curve for ORR is presented in Figure 3. The inefficiency losses associated with different

types of polarisation are presented on this graph. Note that in the graph presented below, only the theoretical aspects of overpotential losses are presented.

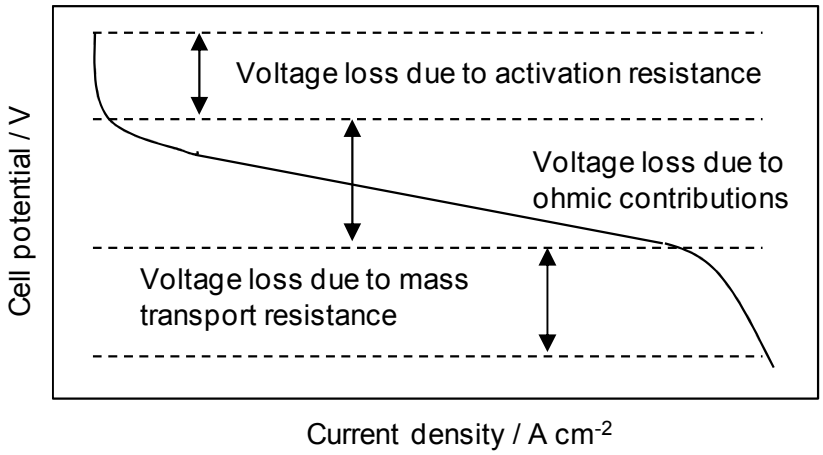

Figure 3 Polarisation curve identifying the difference inefficiencies of a fuel cell. [17]

In this case, polarisation means the difference between the thermodynamic cell voltage and measured cell voltage. The operating fuel cell voltage is always lower than the thermodynamic voltage (1.23 V). In an ideal case without any polarisation losses, the curve should possess the shape of a straight line and be positioned at open circuit voltage value. Unfortunately, the measured cell voltage is that of thermodynamic cell voltage minus the sum of the three polarisation losses. Due to the nature of voltage losses, the polarisation curve is divided into three distinct regions, namely, activation, ohmic and concentration polarisation losses [18]. This could be expressed in terms of overpotential of the electrode as follows (Equation 13 and Equation 14):

$$\eta = E - E_e \qquad \textbf{Equation 13}$$

where

$$\eta = \eta_O\ (activation) + \eta_{iR}\ (ohmic) + \eta_{concentration}\,(mass\ transport) \qquad \textbf{Equation 14}$$

All three regions of inefficiencies can be related to both anodic and cathodic irreversible processes. The theoretical relationship is shown in Figure 4 where anodic oxidation reaction is a red dashed line and cathodic reduction reaction is a blue dashed line. For both anodic and cathodic processes the current is associated with overpotential. The polarisation curve is divided into electron transfer, mixed and mass transfer control current regions. These regions are exactly related to activation, ohmic and concentration overpotentials, respectively. It can be seen from Figure 4a that polarisation curves with positive (oxidation) and negative (reduction) currents can be transformed into a logarithm scale as shown in

Figure 4b. The theoretical discussion regarding activation region is described in the next section (3.3.1).

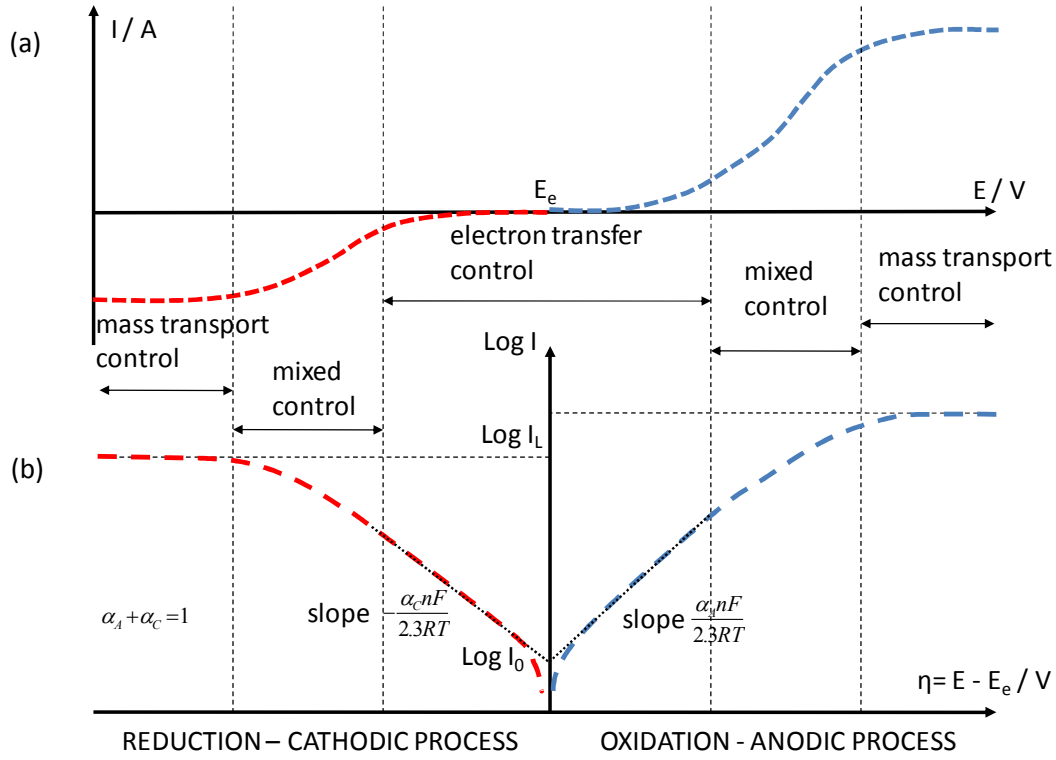

Figure 4 (a) Polarisation curves of redox reactions and their conversion into logarithm scale (b) Tafel plots.

3.3.1 Activation polarisation – Tafel plot

The first region of voltage losses is associated with activation polarisation. This polarisation is caused by the sluggish kinetics of the reaction which takes place on the surface of the electrode. Generally, it can be presented graphically as Tafel plots (Figure 4b) which show the plot of overpotential versus log current density. The currents associated with this polarisation are caused by the most significant voltage losses amongst all the inefficiencies of fuel cells. To increase the performance of the electrode and hence reduce the losses, better catalysts with lower activation resistance should be applied. The activation overpotential can be expressed using the Tafel equation (Equation 15):

$$\eta_O\ (activation) = \frac{RT}{\alpha nF} \ln \frac{I}{I_o} \qquad \textbf{Equation 15}$$

Where α is transfer coefficient, n - number of electrons per reacting ion or molecule, I_o - exchange current density (A m^{-2}), and I - current density (A m^{-2}).

The Butler-Volmer Equation 3 is a general representation of the polarisation of an electrode reduction and oxidation (redox) reaction. This equation plays a role that is fundamental in electrode kinetics. The limiting forms of Butler-Volmer equation exist in oxidation and reduction processes (Equation 3). As overpotentials, either positive or negative, become larger than about 0.05 V, the second or the first term of the equation becomes negligible, respectively. Hence, simple exponential relationships between current and overpotential are obtained, and the overpotential can be considered as logarithmically dependent on the current density.

At high positive overpotentials, Equation 3 becomes Equation 16 and only the anodic current density remains under consideration.

$$\log I = \log I_O + \frac{\alpha_A nF}{2.3RT}\eta \qquad \textbf{Equation 16}$$

At high negative overpotentials the first term of the Equation 3 may be ignored and conversely only the cathodic current density is described as (Equation 17):

$$\log(-I) = \log I_O - \frac{\alpha_C nF}{2.3RT}\eta \qquad \textbf{Equation 17}$$

Both anodic and cathodic kinetic reactions can be expressed graphically as shown in Figure 4. It can be seen from Figure 4b that only the electron transfer control region is in linear relationship after the current density is converted into logarithm scale. The log (I) vs. η plot is curved in the mixed control region and is independent of overpotential (η) in the mass transport region current.

3.3.2 Ohmic polarisation

The second type of inefficiency is connected with ohmic polarization [19-21] and can be described as shown in Equation 18.

$$\eta_{iR} = IR_T \qquad \textbf{Equation 18}$$

This polarization consists of $R_T = r_i + r_e + r_c$, where r_i - ionic resistance, r_e - electronic resistance, r_c - contact resistance.

The origins of the resistance include all parts of the cell, including the electrodes and the electrolyte and current collectors, etc. To calculate the resistance, a current interrupt method can be applied. The method involves switching off the current and measuring the potential as a function of time. After the current is switched off, the potential difference across the ohmic resistance is zero and the charged double layer is discharged. The curve corresponding to the

discharge can be extrapolated to the start, t = 0 seconds, from which the iR drop can be calculated [17]. Each cell has specific ohmic resistance. For this reason, better design of the system could decrease resistance and this would result in a shallower slope in the polarisation curve.

3.3.3 Mass transport polarisation

The third region is associated with mass transport or concentration polarisation and is caused by the concentration change of the reactant species at the surface of the electrode. In comparison to the ohmic resistance curve, where the potential drop is much shallower, a sharp potential drop is observed in this case. This is attributed to depletion of the reactant at the electrode surface because the mass transport fails to feed the reaction with sufficient reactant. This part of the polarisation curve can be described with Equation 19:

$$\eta_{concentration}(mass\ transport) = \frac{RT}{nF}\ln\left(1-\frac{I}{I_L}\right) \qquad \textbf{Equation 19}$$

4 Methods and Techniques – Physical Characterisation of Catalyst

4.1 XRD

X- ray diffraction (XRD) is a common technique used in the characterisation of catalysts. It provides information on both the structure and the composition of the crystalline materials. The theoretical aspects, principles of operation and example profiles will be explained here.

4.1.1 Theoretical Aspects of XRD

The wavelength of X-rays lies between one and one hundred angstroms (Å). This range encompasses useful molecular distances e.g. unit cell dimensions, crystallite size and bond lengths, etc.

The general principle of XRD experiments involves the firing of a beam of X-rays at the sample, which are then scattered by the electrons around the nucleus. When the radiation beam interacts with the sample, diffracted beams are produced. Only a few beams are formed by a single crystal, but in larger amorphous samples, many beams are produced. When the beams are added together and produce lines, they form continuous spots on the film on the image plate [22]. The pattern of spots (called reflections) can be used to determine the structure of the catalyst.

An incident beam of X-rays interacts with the crystal planes within an individual catalyst particle at an angle of θ (theta) as shown in Figure 5.

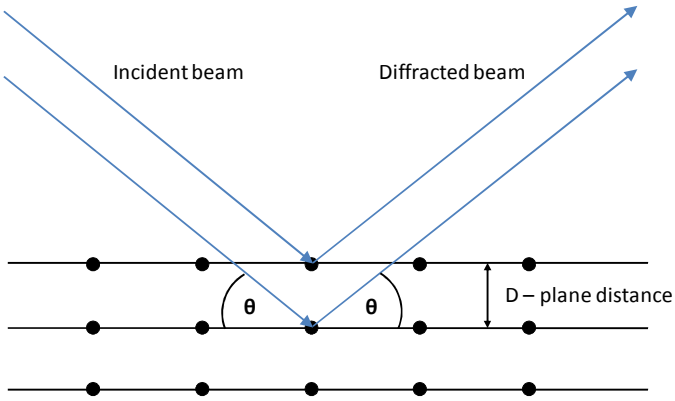

Figure 5 A schematic of the X-ray beam causes diffraction of a portion of energy giving a diffracted beam.

Interference between reflections from different planes takes place, with constructive interference taking place when the parameters of the Bragg equation [23](Equation 20) are fulfilled:

$$n\lambda = 2d\sin\theta$$ **Equation 20**

where: n - an integer, λ - the wavelength of incident X-ray beam, d - distance between the planes (spacing of the atoms) and θ - angle of incidence (theta). The d-separation is determined by the crystal structure and the unit cell dimensions of the crystal in the equation. Extensive catalogues of values for θ diffraction peak exist in the literature and are available for different well-ordered compounds. Those diffraction patterns can be used as fingerprints for the identification of various crystalline phases within the material.

After the diffraction pattern has been collected, it needs to be indexed. The intermolecular spacing for cubic structures d is given by Equation 21

$$d_{hkl} = \frac{a}{\sqrt{h^2 + k^2 + l^2}}$$ **Equation 21**

The Bragg equation can be used in determination of lattice parameter, a , when fcc peak positions and θ_{hkl} have been obtained. The crystallographic parameters h k l are indexes responsible for planes in a crystal structure.

$$\sin^2\theta_{hkl} = \frac{\lambda^2}{4a^2}(h^2 + k^2 + l^2)$$ **Equation 22**

The particle size of a Pt crystal can be measured by measuring the entire width of the peak at an intensity of half its maximum value after a background scan is subtracted. Small crystalline materials with small particle size cause broadening of the X-ray diffraction line profiles. The average crystalline size may be estimated using a Debye-Scherrer equation (Equation 23)

$$\beta_{0.5} = \frac{k\lambda}{L\cos\theta_o}$$ **Equation 23**

where $\beta_{0.5}$ - the width of the diffraction peak at half height, measured in radians, L - the effective crystal diameter (particle size), θ_o - the position of peak maximum and k - constant dependent on the crystalline shape and in the way which $\beta_{0.5}$ and L are defined, and is usually assigned the value 0.9. However, this technique is limited for particle sizes of more than 2 nm, as extensive line broadening occurs for smaller particles.

4.1.2 XRD profiles

All of the XRD data relating to this project were obtained by technicians at the Johnson Matthey Technology Centre and were supplied by Brian Theobald. The example XRD profiles obtained for a set of catalysts described in Chapter 4 section 2.5 are shown below in Figure 6.

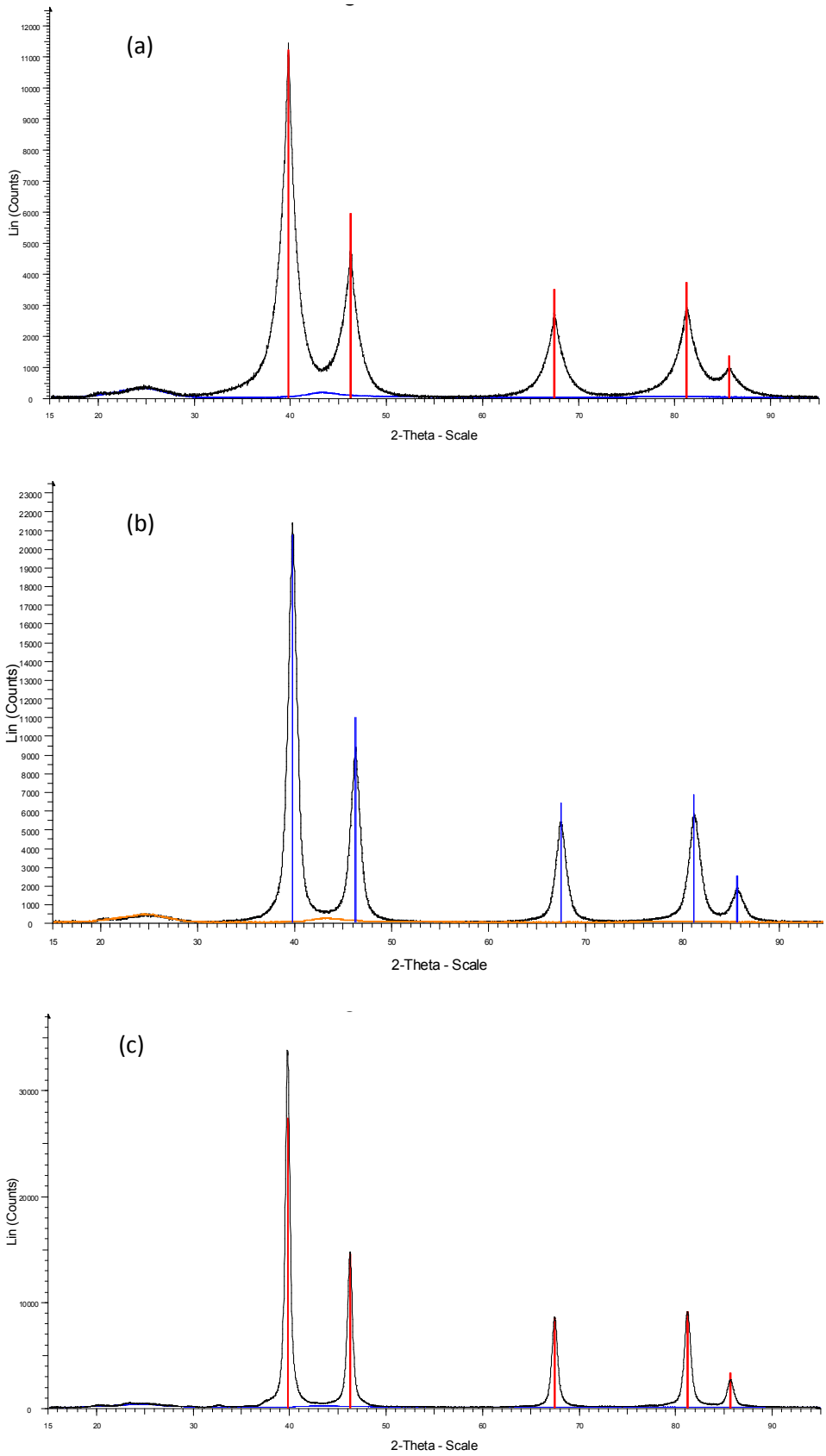

Figure 6 XRD spectrum of a samples containing 40 wt % Pt/C (a) 05/75 with particle size of 4.7 nm (b) 04/131 with particle size of 7.7 nm and (c) 05/79 with particle size of 15.6 nm.

Comparing each XRD profile obtained for catalysts containing 40 wt. % Pt/C with different crystalline size the following conclusion could be reached: the smaller the particle, the wider the peaks. Also important is that all the peaks have the same position on the 2-theta scale. This means that those catalysts possess the same Pt crystallite structure, independent of the particle size.

Bruker AXS D-500 with 40 position sample changer was used as the diffractometer. X-ray diffraction data was determined using the following instrument parameters. The data were obtained using Ni filtered Cu Kα radiation at scan range from 10 to 90°2θ with 0.02° step size. Scan rate was set to 0.25°2θ per minute in a continuous scan. Rotation rate of the sample was set to 30 rpm. Tube voltage and current were 40 kV and 30 mA, respectively. Bruker AXS Diffrac Plus and Eva V9 were used as analysis software. Crystallite size results which were quoted at JMTC have always employed the Scherrer constant of $k = 0.9$.

4.2 TEM

The transmission electron microscopy (TEM) technique [24] in this study of activity of Pt based catalysts supported on carbon was used to provide information regarding the size of the particles.

A transmission electron microscope works on the same principles as a light microscope, but uses an electron beam rather than light to obtain an image of the sample under study. As in a light microscope, an enlarged image of the specimen is observed by focusing through a series of lenses. Transmission electron microscopy (TEM) is a technique in which a beam of electrons is transmitted through a very thin layer of specimen. TEM provides structural information of the materials studied in a user friendly format as an image with very high magnification. Such a high magnification can be acquired because the resolution of TEM is not limited by the wavelength of light, as in optical microscopy. TEM can be used to distinguish the size and distribution of the small platinum particle or platinum-based alloy particles dispersed on a carbon support. An example TEM image of 40 wt. % Pt/C (04/111) catalyst is shown in Figure 7.

(a)

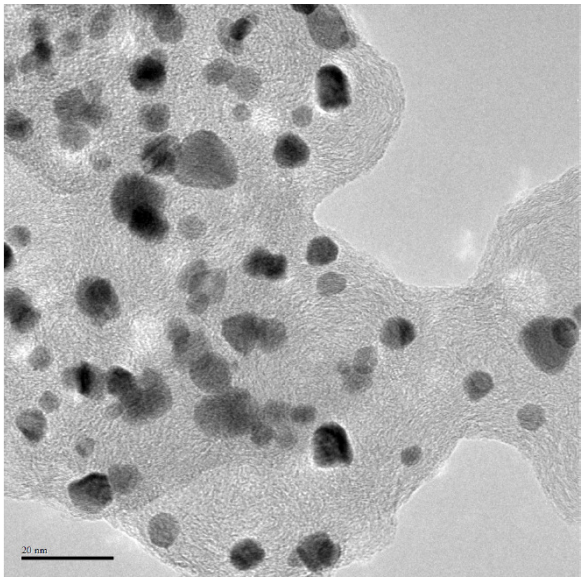

(b)

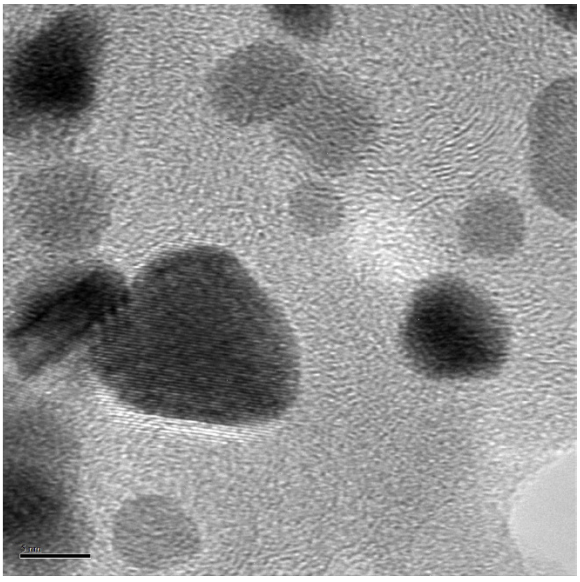

Figure 7 TEM images of 40 wt. % PtCo/C (04/111) catalyst. (a) the scale bar on each micrograph is 20 nm (b) the scale bar on each micrograph is 5 nm.

All the particle size results obtained using TEM imaging were obtained at Johnson Matthey Technology Centre (Sonning Common).

The preparations of the samples were carried out using the dry route. The samples were examined using the Tecnai F20 Transmission Electron Microscope. The instrumental conditions were set at 200 kV voltage with C_2 aperture 30 & 50 m. The apparatus possesses three modes: bright field (BF), high resolution electron microscopy (HREM) and high angle annular dark field (HAADF) method. All the results obtained for particle size analysis (PSA) have been carried out on bright field images.

5 References

1. H. A. Gasteiger, S. S. Kocha, B. Sompalli, and F. T. Wagner, Applied Catalysis B-Environmental 56:9 (2005).
2. F. Gloaguen, P. Convert, S. Gamburzev, O. A. Velev, and S. Srinivasan, in 1997 Joint International Meeting of the International Society of Electrochemistry and the Electrochemical Society, Pergamon-Elsevier Science Ltd, Paris, France, 1997, p. 3767.
3. U. A. Paulus, T. J. Schmidt, H. A. Gasteiger, and R. J. Behm, Journal of Electroanalytical Chemistry 495:134 (2001).
4. V. Stamenkovic, T. J. Schmidt, P. N. Ross, and N. M. Markovic, Journal of Physical Chemistry B 106:11970 (2002).
5. S. Guerin, B. E. Hayden, C. E. Lee, C. Mormiche, J. R. Owen, A. E. Russell, B. Theobald, and D. Thompsett, Journal of Combinatorial Chemistry 6:149 (2004).
6. E. S. Smotkin, J. H. Jiang, A. Nayar, and R. X. Liu, Applied Surface Science 252:2573 (2006).
7. R. Liu and E. S. Smotkin, Journal of Electroanalytical Chemistry 535:49 (2002).
8. R. R. Diaz-Morales, R. X. Liu, E. Fachini, G. Y. Chen, C. U. Segre, A. Martinez, C. Cabrera, and E. S. Smotkin, Journal of the Electrochemical Society 151:A1314 (2004).
9. E. S. Smotkin and R. R. Diaz-Morales, Annual Review of Materials Research 33:557 (2003).
10. D. Pletcher, Instrumental Methods in Electrochemistry, Horwood Publishing, Southampton, 2001.
11. P. P. Wells, Thesis for the degree of Doctor of Philosophy (2007).
12. T. R. Ralph, G. A. Hards, J. E. Keating, S. A. Campbell, D. P. Wilkinson, M. Davis, J. StPierre, and M. C. Johnson, Journal of the Electrochemical Society 144:3845 (1997).
13. D. P. Wilkinson and S.-P. J., in Handbook of Fuel Cells - Fundamentals, Technology and Applications, Vol. 3 (W. Vielstich, Gasteiger, H. A., Lamm, A., ed.), John Wiley & Sons, 2003.
14. D. Thompsett, in Handbook of Fuel Cells - Fundamentals, Technology and Applications, Vol. 3 Fuel Cell Technology and Applications (W. Vielstich, Gasteiger, H. A., Lamm, A., ed.), John Wiley & Sons, 2003, p. 467 (Chapter 37).

15. T. J. Schmidt and H. A. Gasteiger, in Handbook of Fuel Cells - Fundamentals, Technology and Applications, Vol. 2 Electrocatalysis (W. Vielstich, Gasteiger, H. A., Lamm, A., ed.), John Wiley & Sons, 2003, p. 316 (Chapter 22).
16. P. W. Atkins, Physical Chemistry, Oxford University Press, Oxford, 1994.
17. R. J. K. Wiltshire, in School of Chemistry, University of Southampton, Southampton, 2005, p. 226.
18. J. Zhang, PEM Fuel Cell Electrocatalysts and Catalyst Layers: Fundamentals and Applications, Springer-Verlag New York, LLC, 2008.
19. H. A. Gasteiger, W. Gu, R. Makharia, M. F. Mathias, and B. Sompalli, in Handbook of Fuel Cells - Fundamentals, Technology and Applications, Vol. 3 Fuel Cell Technology and Applications (W. Vielstich, Gasteiger, H. A., Lamm, A., ed.), John Wiley & Sons, 2003, p. 593 (Chapter 46).
20. K. C. Neyerlin, H. A. Gasteiger, C. K. Mittelsteadt, J. Jorne, and W. B. Gu, Journal of the Electrochemical Society 152:A1073 (2005).
21. K. C. Neyerlin, W. B. Gu, J. Jorne, and H. A. Gasteiger, Journal of the Electrochemical Society 153:A1955 (2006).
22. A. Rose, in School of Chemistry, Vol. PhD, Southampton, Southampton, 2004, p. 171.
23. W. L. Bragg, Proceedings of the Cambridge Philosophical Society 17:43 (1913).
24. D. B. Williams and C. B. Carter, Transmission electron microscopy: a textbook for materials science, 1996.
25. S. Brunauer, P. H. Emmett, and E. Teller, Journal of the American Chemical Society 60:309 (1938).

Contents

Chapter Three: Rotating Disc Electrode (RDE) 38

Chapter Three: Rotating Disc Electrode (RDE)

1 Introduction

The Rotating Disc Electrode (RDE) [1-13] is currently the most popular method for kinetic and mechanistic studies of Pt catalysts. In this chapter, the principles of the RDE system and the analysis of results for several sets of Pt based cathode catalysts will be presented. The RDE is one of the few systems in electrochemistry in which convective diffusion is controlled. Convection is defined as the transport of species due to external mechanical forces. In the RDE experiment, convection can arise from the movement (rotation) of the electrode [6]. Under conditions of convection control, current densities are 3 to 100 times greater than steady state diffusion limited value. Furthermore, convective diffusion assures a reproducible mass transfer regime at a particular rotation rate.

Platinum supported on high surface area carbons is a commonly used electrocatalyst in low temperature PEMFC for the cathodic reduction of oxygen as well as the anodic oxidation of hydrogen. The development of new catalysts with improved activity requires methods of determination of catalytic activity. Especially in the last two decades, the RDE method has been applied to study the properties of Pt based catalyst using a thin film technique, as described by Markovic *et al.* [11] and Gloaguen *et al.* [9]. Further modification and improvement of this method focused on the preparation of electrodes with low noble metal loadings was described by Schmidt *et al.* [3, 13]. A range of publications that describe much more developed studies on Pt carbon supported catalysts alloyed with second transition metal was issued by Paulus *et al.* [2, 14, 15]. Moreover, a study of PtCo/C and PtNi/C was carried out by Stamenkovic *et al.* [16]. In recent years Gasteiger *et al.* [1] published a paper which provides benchmark oxygen reduction activities for state-of-the-art platinum electrocatalysts using two different methods, the RDE and fuel cell testing of MEAs.

1.1 Principles of operation and experimental factors

In this section the important principles of the RDE system are discussed and the kinetics [11, 12, 17] of the electrode reactions and the mass transfer control region are explained. Most of the experiments performed using the RDE system consider the shape of the current vs. potential (IE) curve at a single rotation rate and the current density at one or a series of potentials as a function of the range of rotation rates. The IE curve for each type of catalyst is analysed in order to elucidate the difference with other catalysts in its limiting current plateau region as well as the kinetic and mass transfer region. In this case, the ability to control mass transfer using the RDE system is particularly important. In electrochemistry,

mass transport can be classed as (i) diffusion, due to a gradient in concentration following Fick's laws (see Chapter 2 section 3); (ii) migration, provoked by a potential gradient in solution; or (iii) convection, defined as a flow of species provoked by a mechanical force. If the mass transport regime of an experiment is known exactly, interpretation of reaction kinetics is possible. The second aspect of RDE experiment analysis is the comparison of polarisation (IE) curves collected at different rotation rates.

The RDE consists of a disc-shaped electrode embedded in a PTFE (or other insulating) sheath. The entire assembly is rotated, resulting in a laminar flow of solution to the electrode. As shown in Figure 1 a, b and c, when the flux of solution almost reaches the surface of the electrode, it is thrown outwards.

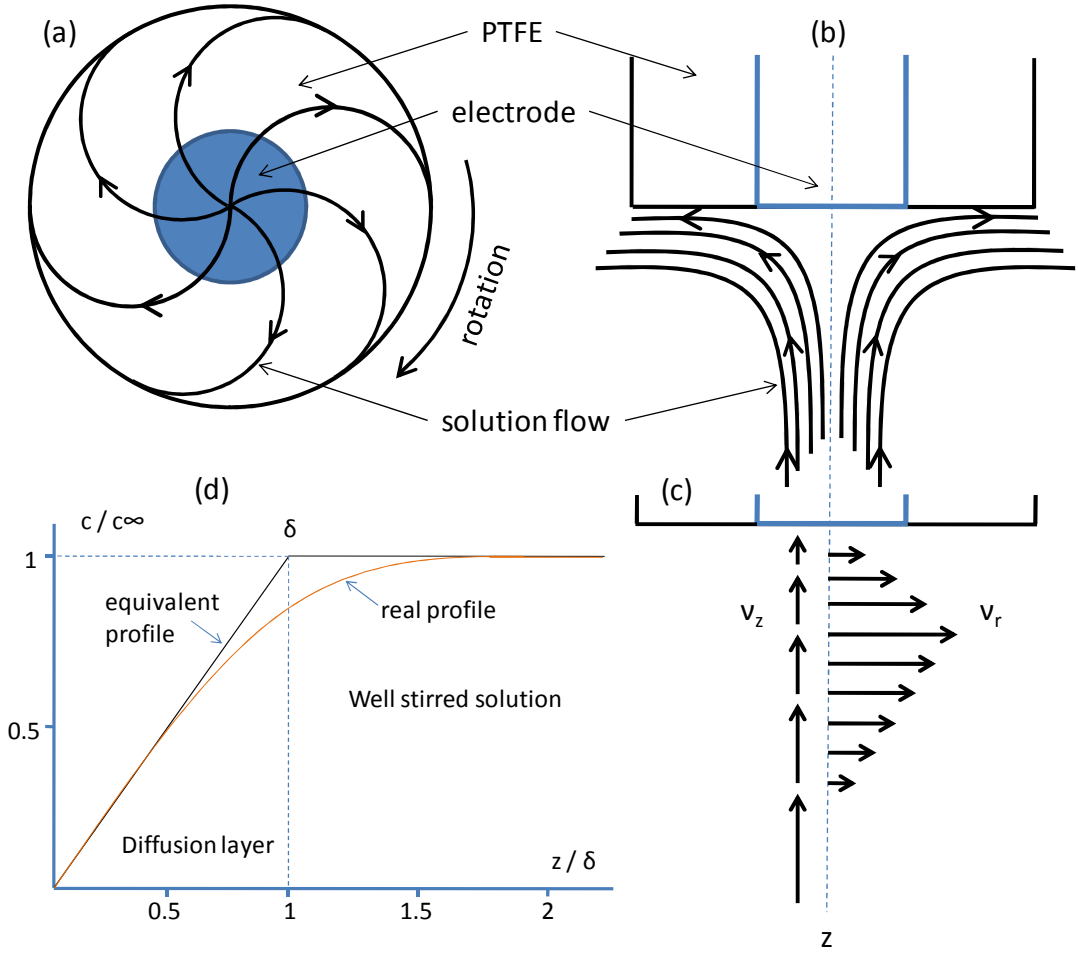

Figure 1 Flow patterns created when electrode rotates in the electrolyte solution: (a) view from below; (b) view from the side; (c) vector representation of fluid velocities near disc; (d) concentration profile and Nernst diffusion layer.

The rotation of the electrode helps to keep the concentrations of all species at their bulk value throughout with the exception of the electrode surface. The thickness of the boundary layer at the surface of the electrode 'δ' depends on the rotation speed (Figure 1 d). The movement of the species within the boundary layer occurs only by diffusion. The thickness of the layer decreases when the rotation rate increases. This is expressed mathematically by the Levich equation [6]. If the data collected shows agreement with the Levich equation then conditions of mass transport control have been obtained.

The Levich equation (Equation 1) is described as follows:

$$I_L = 0.62nFD^{2/3}\upsilon^{-1/6}c^{\infty}\omega^{1/2} \qquad \textbf{Equation 1}$$

Where: I_L - the limiting current density (A cm^{-2}), 0.62 - a constant which depends on the units of the other variables in the equation, n - the number of electrons involved in the process, F - the Faraday's constant (C mol^{-1}) , D - the diffusion coefficient (cm^2 s^{-1}), υ - kinematic viscosity (cm^2 s^{-1}), c^{∞} - the concentration of electroactive species in the bulk solution (mol cm^{-3}) and ω - the angular rotation rate of the disc (s^{-1}). Thus a plot of I_L vs. $\omega^{1/2}$ should yield a straight line that passes through the origin.

Figure 2 shows typical cyclic voltammogram obtained in ORR whilst the disc of the electrode rotates. It is easily spotted that both, forward and reverse scans currents do not overlap on the graph. Although the currents are similar, especially at higher potentials in kinetic region. The loops created during the ORR reaction are dependent on many factors related to specific reactions occurred at particular potentials and will be described below.

The IE (polarisation) curve obtained using an RDE may be divided into three distinct regions as indicated in the diagram, Figure 2. At low current densities, the current is entirely defined by the kinetics of electron transfer. The intermediate region is characterised by mixed control and at high current densities the current is limited by mass transfer I_L.

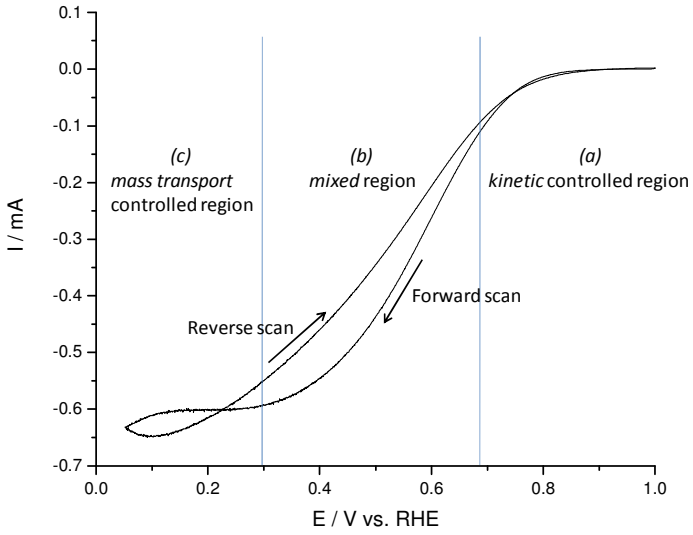

Figure 2 Polarisation curves of 20 wt. % Pt/C in 1 mol dm^{-3} H_2SO_4 acquired at a scan rate of 2 mV s^{-1} and 2500 RPM rotation rate. The oxygen was continuously flowing above the surface of the electrolyte.

Region (a) is the kinetic controlled region. The current is low and according to different scientists [18] normally reaches only one fifth or one sixth of the total current of the curve. This region is also deformed by construction of a Tafel plot as described in Chapter 2, where the pure kinetic region corresponds to the linear region of the Tafel plot. Mass transport in the bulk solution has no influence on this kinetic current. For this reason, the current in this region should remain identical as the mass transport in the solution alters, i.e. as the rotation rate increases. The difference between the current obtained for forward scan and that of the reverse scan is attributed to oxide layer formation, which occurred at high potentials. Usually, the negative-going (forward) scan possesses slightly lower currents in comparison to positive-going scan. When scanning towards lower potentials, the oxide layer is present, whilst on the reverse scan towards higher potentials the oxide layer has been removed; hence the smaller currents on the forward scan and the larger currents in the reverse.

Region (b) is the mixed control region. There is a mixed control of current by the mass transport and the electron transfer of kinetic reaction. Mass transport plays a major role in maintaining the concentration of the species constant throughout the cell up to the diffusion layer. The situation between forward and reverse scan change when mass transfer starts play a role in mixed control region influencing currents. A Similar situation for the reduction of the oxide species occurred in the mixed control region. This time on the voltammogram both forward and reverse scan create a loop. The hysteresis between negative-going (forward) and positive-going (reverse) scans occurred. The hysteresis is due to reactions, which took place simultaneously in the forward scan, reduction of the oxygen and reduction of the oxide at the

surface of the electrode. In the reverse scan, the surface is free of oxide and only the reduction of oxygen occurred.

Region (c) is the mass transport controlled region. The measured current will be susceptible to any change in rotation rate. As the rotation rate increases the mass transfer limiting current increases. As seen in Figure 2 the current in the voltommogram created another loop in mass transport controlled region when reaching the limiting current. The speculation is that this hysteresis is related to hydrogen adsorption, which normally occurs at these potentials, as observed in the standard Pt cyclic voltammograms in the absence of oxygen.

At any potential in the mixed control region, the current measured can be expressed via the kinetic equation (Equation 2):

Equation 2

$$-I = nF\,\vec{k}\,c_O^{\sigma}$$

Where: $\vec{k}$ - the rate constant for the electron transfer reaction and c_O^{σ} is the concentration of the electroactive species at the electrode surface.

Similarly, it can be expressed by the Nernst diffusion layer model equation (Equation 3):

Equation 3

$$-I = nF\,k_m\left(c_O^{\infty} - c_O^{\sigma}\right)$$

Where: k_m - the mass transport coefficient, and c_O^{∞} is the concentration of electroactive species in the bulk solution.

Hence, when eliminating *I*, the equation translates into Equation 4:

Equation 4

$$c_O^{\sigma} = \frac{k_m c_O^{\infty}}{\vec{k} + k_m}$$

Now substituting Equation 4 into Equation 2 gives Equation 5:

Equation 5

$$-\frac{1}{I} = \frac{1}{nF\,\vec{k}\,c_O^{\infty}} + \frac{1}{nFk_m c_O^{\infty}}$$

which can be simplified to Equation 6:

$$\frac{1}{I} = \frac{1}{I_k} + \frac{1}{I_L}$$ **Equation 6**

Where: I_L -the diffusion limited current density and I_k - the true kinetic current density [19]. Hence, the kinetic current can separated out from any mass transport effects. Thus, the kinetic current may be obtained as a function of the potential, as follows (Equation 7):

$$I_k = \frac{I\, I_L}{I_L - I}$$ **Equation 7**

In comparing the activities of the catalysts, the specific activity is commonly used. This is obtained by correcting the kinetic current by dividing by the Pt real surface area to obtain the current per cm^2 of Pt.

The Pt real surface area was determined electrochemically by integrating either the CO stripping peak or the hydride adsorption region peak (see Chapter 2 section 3.2) from the cyclic voltammogram.

2 Experimental Details

2.1 System components

The RDE system consists of a PINE AFMSRX Modulated Speed Rotator (MSR) and exchangeable disc system (E4 Series Change Disk RDE Tips), glass cell and Pine instrument rotation rate control unit. An MMS electrode and a Pt gauze were used as the reference electrode (RE) and counter electrode (CE) respectively. The electrodes were connected into a high power AUTOLAB PGSTAT30 potentiostat. The GPES AUTOLAB software was used to apply and control the potential and record the current. The rotating shaft with the electrode tip was mounted into the RDE cell as described below.

2.2 Cell design

The RDE measurements were carried out in a specially designed three electrode glass cell. The cell had a water jacket to maintain a constant elevated temperature (298 K), water being pumped from a thermostatically controlled water bath (Grant). The cell used for the measurements is shown schematically in Figure 3. The Pt mesh counter electrode (Goodfellow Pt mesh, 99.9 %) was placed below the working electrode, perpendicular to the rotating shaft and parallel to the glassy carbon electrode surface. The vitreous carbon working electrode (5 mm diameter) was surrounded by PTFE insulating material as shown in Figure 1a and b. A PTFE shield was mounted around the rotating rod to ensure that no dust could fall from the top of the Pine RDE into the electrochemical cell. Gases such as

nitrogen and oxygen can either be bled over the surface of the solution during measurements or be introduced by inserting the gas tube into the electrolyte and being purged (CO, O_2, N_2) through it. The experimental reference electrode was again a commercial MMS electrode placed in the reference compartment with a Luggin capillary connection to the cell. All potentials presented in this thesis are reported against the reversible hydrogen electrode (RHE) in 1 mol dm^3 H_2SO_4 as described in Chapter 2 section 2.1.

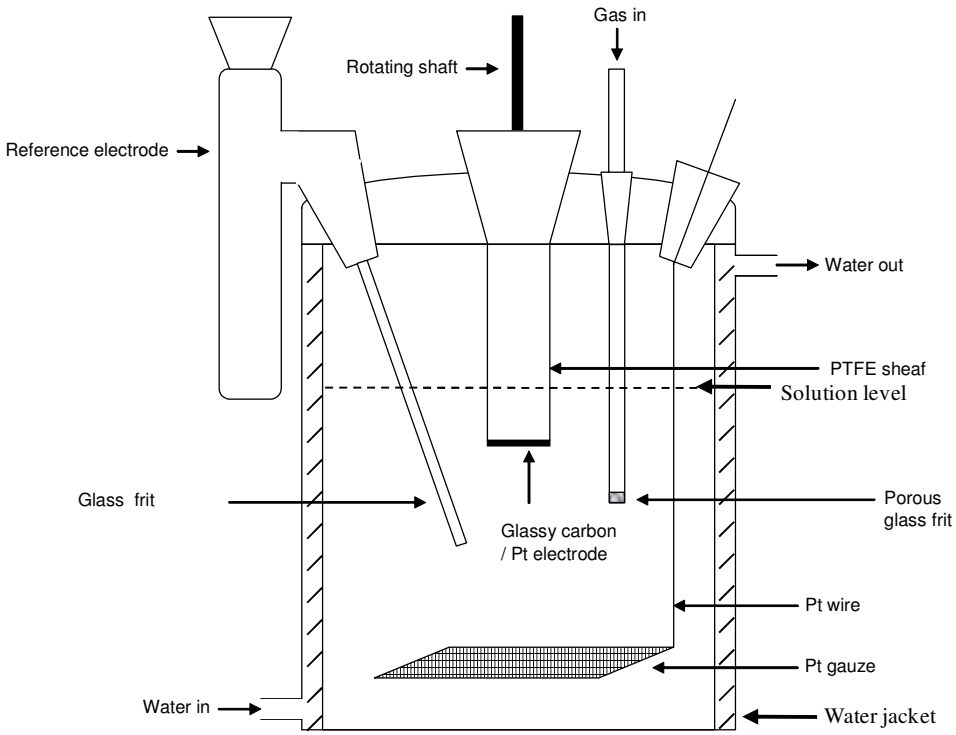

Figure 3 Electrochemical cell for RDE measurements [19].

2.3 Electrode cleaning

Prior to applying the catalyst suspension the glassy carbon electrode was cleaned. Iso-propanol (IPA) was used first in order to remove of old catalyst residue. Then, the vitreous carbon electrode was polished manually using alumina powder (Buehler, grain sizes of 1, 0.3, 0.05 μm). The alumina powders were wetted separately with purified water (16-18 MΩ cm). The polishing was performed using the largest particle alumina first, and the finest powder was applied at the end. In between polishing with alumina powders, the electrode tip was rinsed several times with water. At the end, the electrode tip was immersed in purified water and sonicated briefly in an ultrasonic bath to remove any residual particulates affixed to the disc. The electrode was dried by air or by use of a heat gun.

2.4 Ink and electrode preparation method

This procedure of ink preparation was used in all the experiments performed and reported in this chapter. 10 mg catalyst and 10 mL chloroform were mixed using an ultrasonic bath for

30 minutes to form a suspension of well-dispersed catalyst. A 5 μL aliquot of this solution was deposited onto the surface of a glassy carbon rotating disc electrode with 5 mm diameter [area - 0.196 cm^2] and allowed to dry. 5 μL of a mixed solution containing 5 wt % Nafion® [12] in low atomic weight alcohol (50 μL) and 99.5 % iso-propanol (4950 μL) were deposited onto the catalyst layer and allowed to dry in air at room temperature for 30 min. Low atomic weight alcohol solution allow to disperse Nafion polymer more uniformly.

2.5 RDE Experimental procedure

Before the experiment commenced, the electrochemical connections were checked as any degradation in the quality of the connection will create noise. Many problems occurred during measurements and these were often traced to the cell connections.

2.5.1 Cyclic voltammetry – CO stripping

The electrode was inserted into an electrochemical cell filled with 1 mol dm^{-3} H_2SO_4. Prior to commencing the experiment the electrolyte was purged with nitrogen for 20 minutes. Conditioning scans were run from 0.05 V to 1.2 V vs. RHE at 10 mV s^{-1} scan rate. The scans were continued until a constant overlay of voltammetric data was observed.

The CO stripping experiment [13, 20, 21] was performed in order to calculate the Pt real surface area using the CO peak charge as described in Chapter 2 section 3.2. Before the experiment's start, CO was purged for 15 minutes through the electrolyte, while the potential was held at 0.05 V. At this potential, CO creates an adsorbed layer on the Pt catalyst. To remove dissolved CO from the electrolyte, the electrolyte was subsequently purged with nitrogen for another 30 minutes and the potential was held continuously at 0.05 V. After the pretreatment, the voltammograms were run starting from 0.05 V and scanning to 1.2 V vs. RHE. Normally three voltammograms were acquired.

2.5.2 Oxygen Reduction Reaction (ORR)

ORR activity was determined following CO stripping measurements as follows. The electrolyte was purged with O_2 for 10-20 minutes, whilst the electrode was rotating at 1000 rpm. The position of the gas inlet tube was then raised to just above the surface of the solution and polarization curves were obtained at a range of rotation rates. The potential was scanned from 0.05 V and 1 V vs. RHE at 10 mV s^{-1}. Typical rotation rates were 900, 1600, 2500 and 3600 rpm.

3 Reproducibility and Qualitative agreement

This section overviews the reproducibility of the data obtained using the RDE and the qualitative agreement of a set of 40 wt % PtCo/C catalysts [4, 8, 14-16, 22] with different particle sizes [3, 10, 23] and 20 wt. % Pt/C catalyst named as 'standard' for comparison (Table 1) with the known trends in activity of such catalysts. Each experiment with one of the catalysts tested was run up to four times. The best two runs out of four, where good reproducibility was achieved, were chosen to present in this section. For ease of later comparison, the catalysts sets were chosen to match those used in the 64 channel array experiments described in Chapter 4.

Table 1 Details of the PtCo/C and 20 wt. % Pt/C catalysts investigated (set 1).

No.	Catalyst code	Composition	XRD - Crystal Size / nm	XRD - Lattice Parameter / Å
(a)	-----	20 wt% Pt/C (XC72R)	-----	-----
(b)	05/76	40 wt% Pt (Pt:Co 3:1) / C	3.6	3.85
(c)	04/118	40 wt% Pt (Pt:Co 3:1) / C	3.7	3.85
(d)	04/111	40 wt% Pt (Pt:Co 3:1) / C	5.9	3.85
(e)	04/132	40 wt% Pt (Pt:Co 3:1) / C	12.6	3.85

3.1 Cyclic voltammetry

CO stripping voltammograms were obtained for each catalyst and the results are shown in Figure 4, showing results of two duplicate experiments for each sample. As can be seen from the data presented in Figure 4, obtaining the reproducible voltammograms for the catalysts on the RDE was difficult. The CVs shown have been normalised to take into account variations in the amount of catalyst deposited; currents densities were defined with units of $\mu A\ cm^{-2}_{Pt}$, which are obtained by using the CO stripping peak areas. Even when variations in the loading are accounted for, the voltammograms' differences were found in the position of the CO and oxide peaks, the resolution of any hydrogen feature, and the magnitude of the capacitance in the double layer region.

The positions of the CO and oxide stripping peaks are often used as markers of electrocatalytic activity [4]. These positions are summarised in Table 2 for both replicates of each experiment. It can be seen in Table 2 when the Pt real surface area displays discrepancy for the experiments carried out for (e) 04/132 sample, the variation in parameters' positions is enormous. As seen in Table 2, the oxide peak potential was relatively constant for all the

catalysts studied. In contrast, the onset potential shifted towards lower potentials as the particle size increased. The trend of CO peak maximum potential remains undefined.

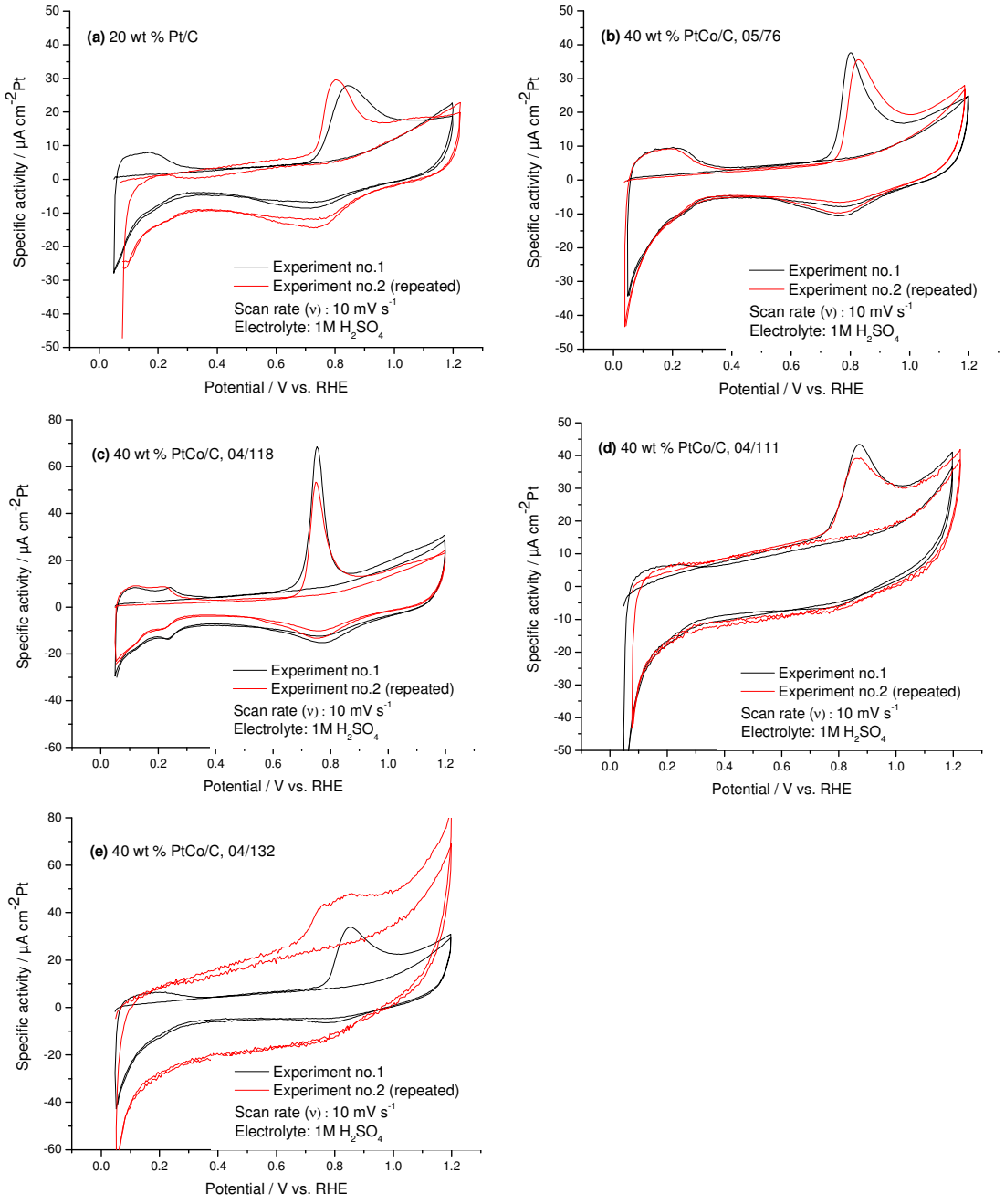

Figure 4 CO stripping voltammograms along with second scan of catalysts described in details in Table 1. Comparison of replicate experiments of (a) 20 wt% Pt/C (b) 05/76 (c) 04/118 (d) 04/111 (e) 04/132.

Table 2 Comparison of electrochemical parameters extracted from cyclic voltammograms shown in Figure 4

	Catalyst type, catalyst code	CO peak onset position / mV		CO peak (maximum current) position / mV		Oxide peak (maximum current) position / mV		Pt real surface area / cm^2	
		Exp. 1	Exp. 2	Exp. 1	Exp. 2	Exp. 1	Exp. 2	Exp. 1	Exp. 2
(a)	20 wt% Pt / C	684	684	845	803	715	728	0.898	0.462
(b)	40 wt% PtCo (3:1)/C, 05/76	689	719	800	827	770	764	0.567	0.432
(c)	40 wt% PtCo (3:1)/C, 04/118	620	636	751	749	773	757	0.725	1.02
(d)	40 wt% PtCo (3:1)/C, 04/111	683	683	870	875	770	770	0.163	0.152
(e)	40 wt% PtCo (3:1)/C, 04/132	682	591	852	812	778	753	0.298	0.114

In summary, the designed level of reproducibility was achieved only for catalyst (a) 20 wt. % PtCo/C, (b) 05/79, (c) 04/118 and (d) 04/111. The discrepancy that occurred with (e) 04/132 catalyst was attributed to unequal Pt loading [7-10, 20, 24] associated with the lower Pt particle size present in this catalyst.

3.2 Oxygen Reduction Reaction (ORR)

To check the reproducibility of the ORR measurements, voltammograms were obtained as a function of rotation speed using a scan rate of 2 mV s^{-1}. An illustration of typical RDE oxygen reduction testing is shown in Figure 5. The rotation speed of the working electrode was 900, 1600, 2500 and 3600 revolutions per minute (RPM) for sequential scanning. Hence the mass control limiting currents should be proportionally higher as the rotation speed was increased. Importantly, the kinetic currents [11, 12, 17] remained the same for all four scans acquired during ORR. Excellent agreement was obtained in the kinetic region (0.8 V to 1.0 V) for the two replicates, with slight deviations observed in the mixed control and mass transport controlled regions. [6] The latter may have been affected by effect variations in the oxygen saturation of the electrolyte between measurements. Unfortunately, the exact variation in oxygen saturation in the electrolyte was not measured during this project.

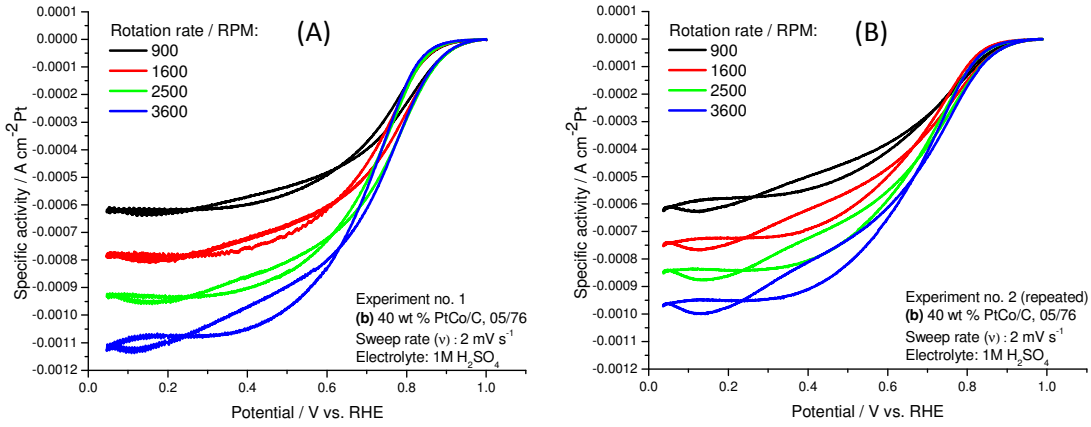

Figure 5 ORR replicate experiments carried out for 40 wt. % PtCo/C (05/76) catalyst. Cyclic voltammograms run from 1.0 V to 0.05 V vs. RHE in 1 mol dm^{-3} H_2SO_4, with scan rate of 2 mV s^{-1}. (A) Experiment 1 (B) Experiment 2 (repeated)

The performance of the RDE was confirmed by plotting the limiting current vs. the square root of the rotation speed in a Levich plot as shown in Figure 6 (A) and (B). The linear plots confirm proper mass transport control at high overpotentials. Unfortunately, the intercepts do not exactly pass through the origin, indicating a level of error in the measurement.

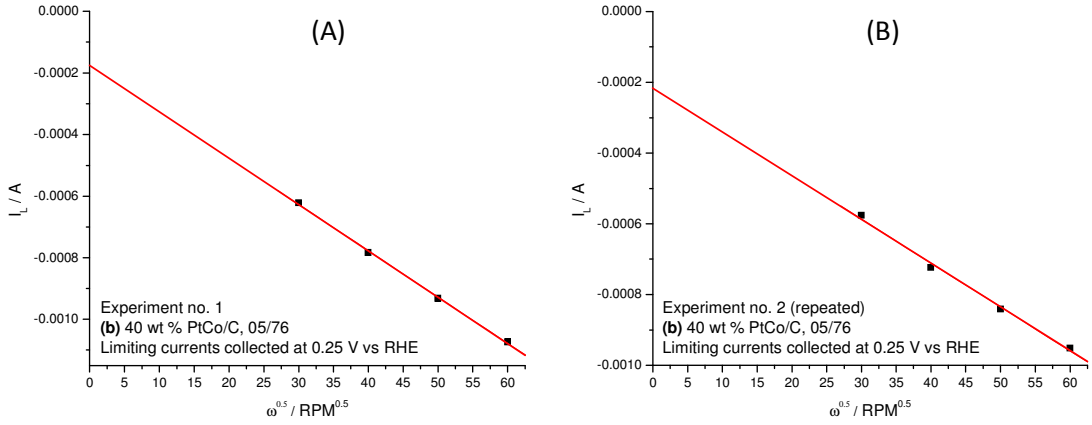

Figure 6 Levich plots obtained by analysis of the cyclic voltammograms shown above in Figure 5. The limiting currents collected at 0.25 V (forward scan) at each rotation rate were plotted against rotation rate $\omega^{0.5}$ (A) Experiment 1 (B) Experiment 2 (repeated). Linear regression lines (red colour) are included, with the straight line indicating good mass transfer control.

Figure 7 is a demonstration of two separate ORR experiments carried out using the same 40 wt. % PtCo/C (04/111) catalyst. In both cases, the testing procedure was identical. As can be seen, the magnitudes of currents normalized by Pt real surface area were dissimilar.

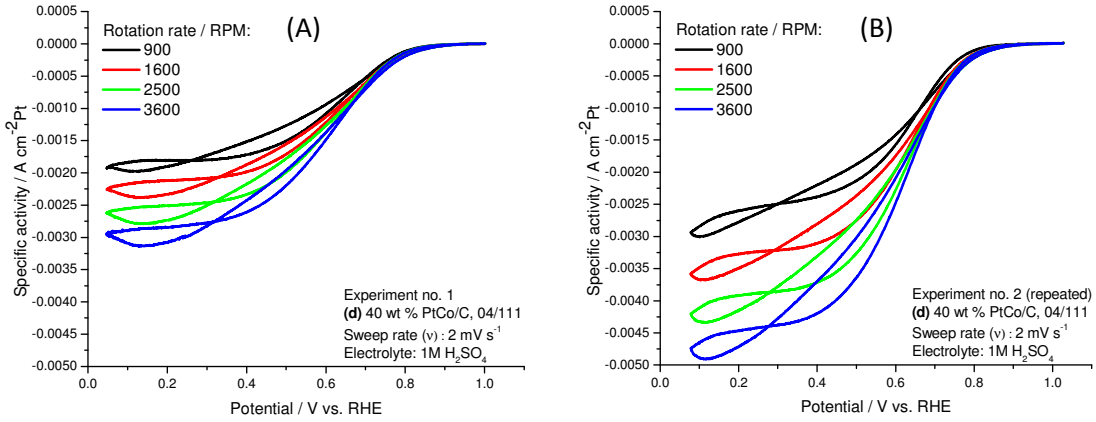

Figure 7 ORR replicate experiments carried out for 40 wt. % PtCo/C (04/111) catalyst. (A) Experiment 1 (B) Experiment 2 (repeated)

The current density values used to plot Levich plots shown in Figure 8 were extracted again from cyclic voltammogram limiting currents displayed above. The current points at each of the graphs almost formed a straight line. In an ideal situation, the data points should perfectly overlap with the linear regression red line. Analysing Figure 8 (A) and Figure 8 (B), the black squares are slightly off trend, especially in graph (B). The difference in positions observed for Levich plots of 04/111 catalyst was, therefore, on the frontier of the confidence limits of measurements, approximately 15 %.

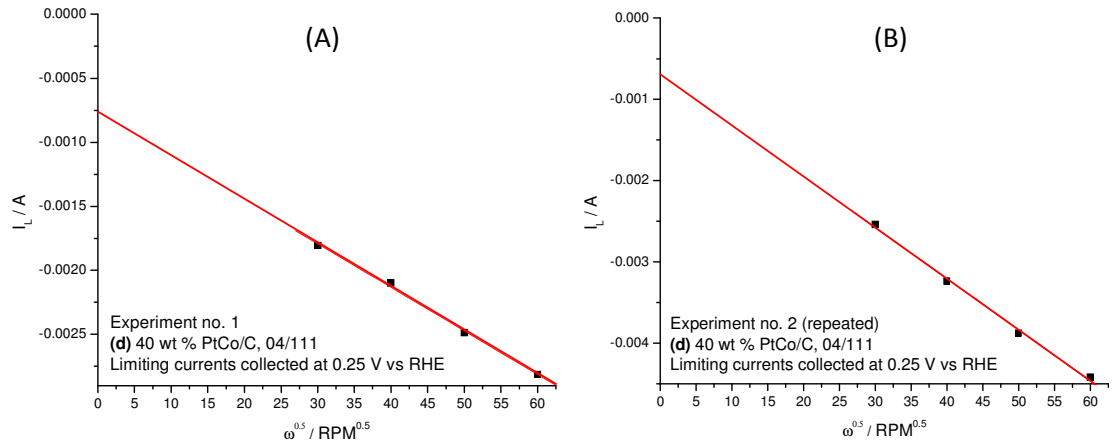

Figure 8 Levich plots of the cyclic voltammograms shown in Figure 7. The limiting currents at each rotation rate were plotted against rotation rate $\omega^{0.5}$. (A) Experiment 1 (B) Experiment 2 (repeated).

4 Results and Discussion

The RDE results reported in these studies have been separated into three subsections. Here, it should be noted that the results were purposely grouped to facilitate later comparison with the sets of results obtained using the 64 channel array. The experiments presented were

carried out using 20 wt. % Pt/C catalyst, named as 'standard', and a group of 40 wt. % PtCo/C catalysts. The PtCo/C catalysts were selected to probe the effects of different structure, particle size, composition and pre-treatment (acid leaching) on the ORR activity of these materials.

4.1 Particle Size effect on PtCo/C

The first set of catalysts described measures the influence of particle size on their ORR activities. The set of samples tested was described in detail in Table 1. The catalysts were purposely arranged from catalyst (b) with the smallest particle size to (e) with the largest.

Polarisation curves were obtained for each of the catalysts in the set in duplicate and the results are shown in Figure 9. If the ORR was strictly mass transport controlled in the limit of high current density, corresponding to the plateau between 0.05 and 0.2 V, then according to Equation 1, all the polarisation curves should have the same limiting current. It is readily apparent from the data shown in Figure 9 that this is not the case, even through linear Levich plots were obtained for each catalyst-covered electrode. The origins of the observed differences may be attributed to (i) a variation in the mechanisms of the ORR ($2e^-$ vs. $4e^-$ reduction); (ii) variations in oxygen saturation of the electrolyte; or (iii) effects of the film of catalyst either not covering the entire disc or extending beyond the edges of the disc. The latter is the most likely and accounts for the variation observed in the duplicate measurements.

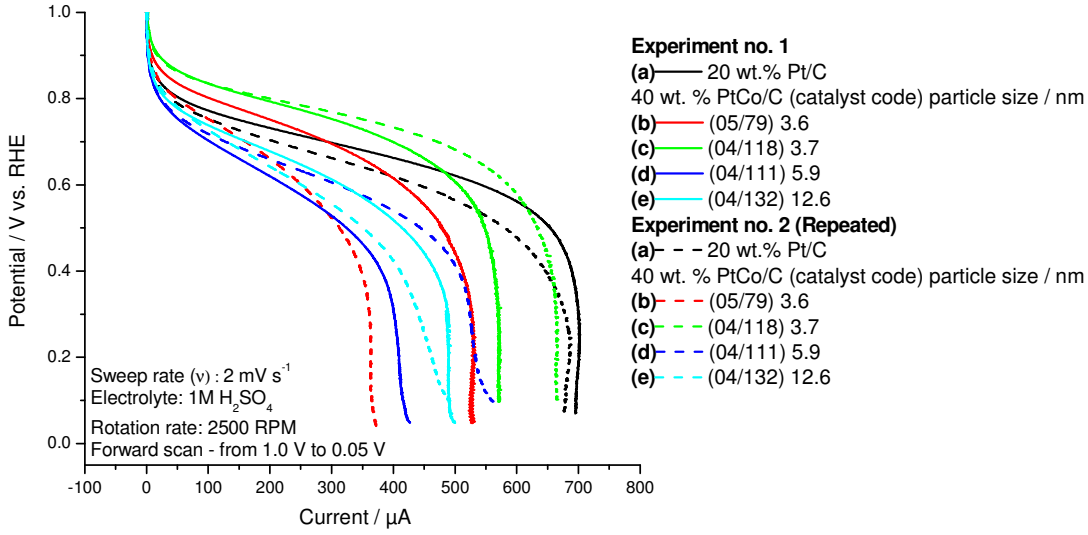

Figure 9 Polarisation curves (raw currents) collected for catalysts described in Table 1. MMS was used as reference electrode and the potential scale was corrected to RHE electrode. Replicate experiments were run using the same catalysts and were carried out in 1 mol dm^{-3} H_2SO_4.

Comparison of the ORR activities of the catalysts is restricted to the region in which the rate is kinetically controlled. Therefore, the data were corrected to determine the kinetic current densities as defined in Equation 7. The corrected polarisation curves corresponding to the data in Figure 9 are shown in Figure 10.

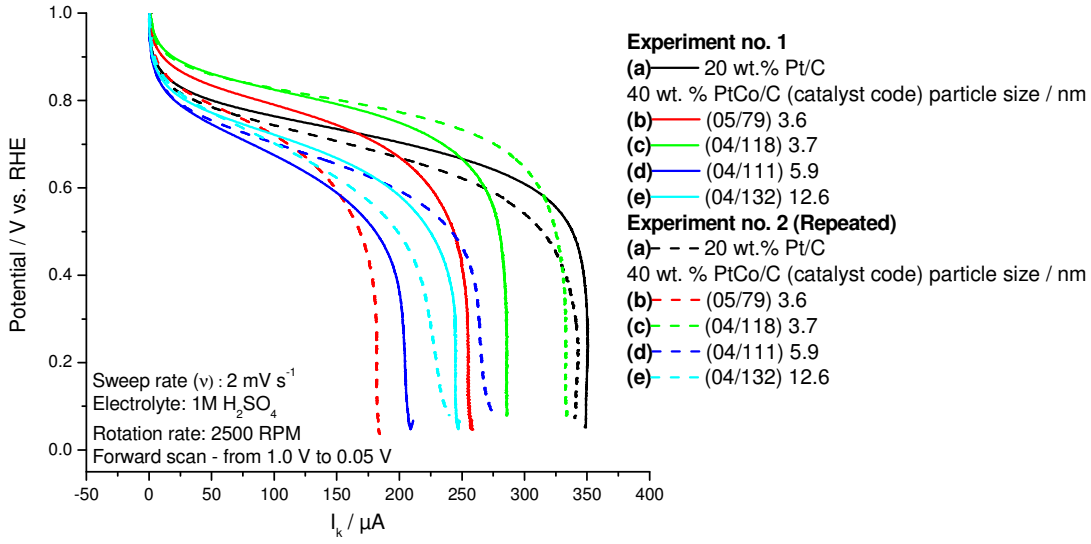

Figure 10 Polarisation curves collected for catalysts described in Table 1. The currents were corrected by mass transfer limiting current value extracted at 0.2 V potential and using Equation 7.

Finally, the data were corrected to obtain the specific activities [6] by dividing the kinetic current by the Pt real surface area, and transformed into logarithm scale. The results are presented as a Tafel plot in Figure 11. Tafel regions represent only the purely kinetically controlled current. As can be seen, fairly reasonable agreement was obtained between the pair of duplicate measurements.

The ORR activity of Pt catalysts is known to depend on particle size, with greater specific activities (A cm^{-2}) generally found for larger particles [4, 25]. The data generally agree with this trend with the 12.6 nm PtCo/C having the greatest activity. The 3.6 nm (05/79), 3.7 nm (04/118) and 5.9 nm (04/111) catalysts all have very similar activities in agreement with previously reported studies [26-28].

The results also reflect the enhanced activity of PtCo/C catalysts over Pt/C [25, 29]. For larger particles, Pt and Co elements are better alloyed; hence, the structure exhibits better surface and bulk ordering and enhanced activity.

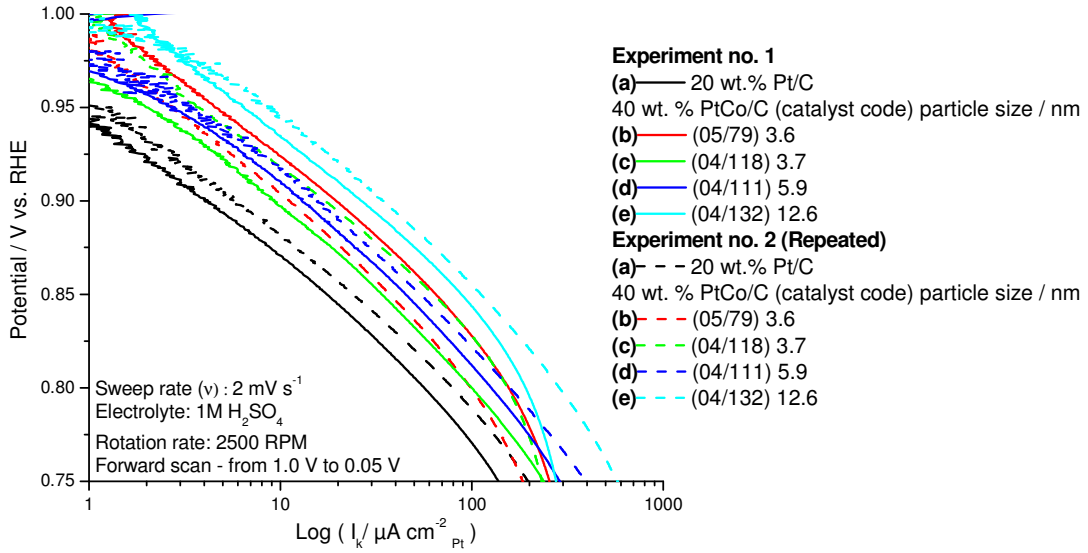

Figure 11 Tafel plots - comparison of a series of PtCo/C catalysts along with 20 wt. % Pt/C. All the 40 wt % PtCo/C catalysts were heat treated in hydrogen as indicated, for which the 20 wt. % Pt/C catalyst was used without further treatment. Data were extracted from Figure 10. In addition to initial kinetic current correction using Equation 7, the currents were normalized per unit of Pt active surface area determined using the CO stripping peak area.

4.2 Acid leached samples

The effects of acid leaching, which may remove any excess unalloyed Co as well as Co from the surface of the particles was assessed by examination of a set of catalysts as described in Table 3, where catalysts 05/19 and 05/66 represent treated variations of 04/111. All the catalysts provided were previously acid leached at Johnson Matthey Technology Centre. The polarisation curves for this set are shown in Figure 12 and the corresponding Tafel plots (corrected to yield the specific activity) are shown in Figure 13. The PtCo catalysts all exhibited very similar oxygen reduction activities, with very little effect of the acid leaching being apparent.

Previously reported work by Teliska *et al.* [30] presents the influence of $HClO_4$ leaching on surface composition of the PtCo/C catalysts. The findings are that PtCo clusters were quite homogenous after leaching conditioning. This means that Co was not leached significantly from the surface of the alloyed PtCo particle. Moreover, the Pt:Co ratio, 3:1, which was similar to the catalyst tested in this study, gave a totally homogenous cluster. Similarly, Paulus *et al.* [15] and Stementkovic *et al.* [16] found that Co in a PtCo sample did not leach out from the surface of the alloy particle by using $HClO_4$. The authors suggest that the non-leaching character in PtCo clusters was attributable to an electronic stabilisation of the cobalt in the bimetallic particle. In addition, the catalytic enhancement for PtCo catalysts tested in ORR was greater in $HClO_4$ than in H_2SO_4.

Table 3 Catalysts used in experiments (description of pre-treatment in the preparation procedure). XRD results present no variation in particle size of each catalyst. (set 2)

No.	Catalyst code	Composition	Acid leached	XRD - Crystal Size / nm	XRD - Lattice Parameter / Å
(a)	-----	20 wt. % (Pt) / XC72R	-----	-----	-----
(b)	04/111	40 wt% Pt (Pt:Co 3:1) / C	no	5.9	3.85
(c)	05/19	40 wt% Pt (Pt:Co 3:1) / C	H_2SO_4	5.9	3.85
(d)	05/66	40 wt% Pt (Pt:Co 3:1) / C	$HClO_4$	5.9	3.85

The kinetic currents obtained and calculated from raw currents of set 2 catalysts (Table 3) are shown in Figure 12.

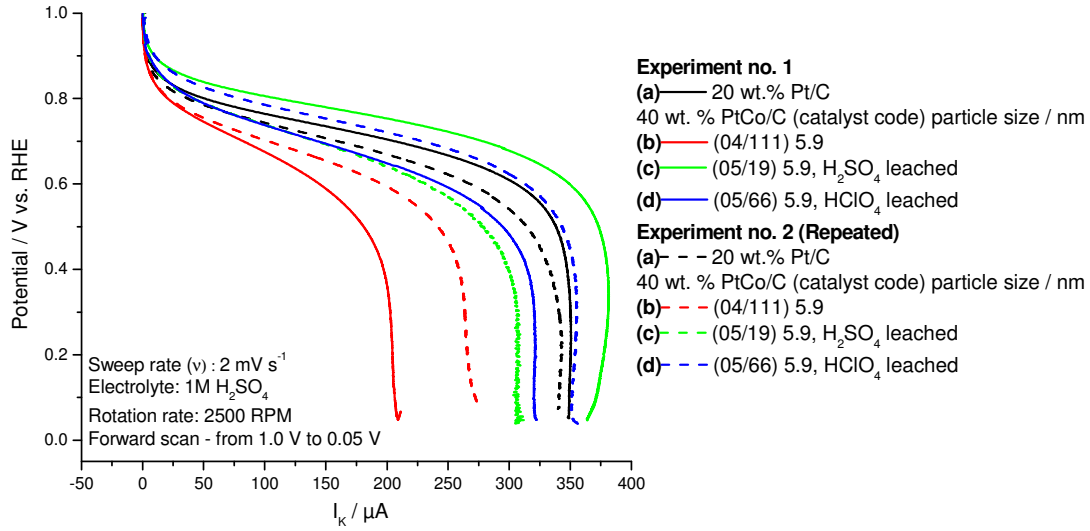

Figure 12 Polarisation curves collected for catalysts descried in Table 3 using the RDE method. Both replicate experiments (identical colour) were run using the same catalysts and testing procedure.

Similar results for both scans of the same catalyst were achieved after the kinetic currents were normalized with Pt real surface area, and were plotted as Tafel plots (Figure 13). The results obtained for 40 wt. % PtCo/C catalysts were very similar to each other. However, slightly better performance was displayed by catalyst (d) 05/66 leached with $HClO_4$. Undoubtedly, the worst performance among the catalysts measured was (a) 20 wt. % Pt/C electrode.

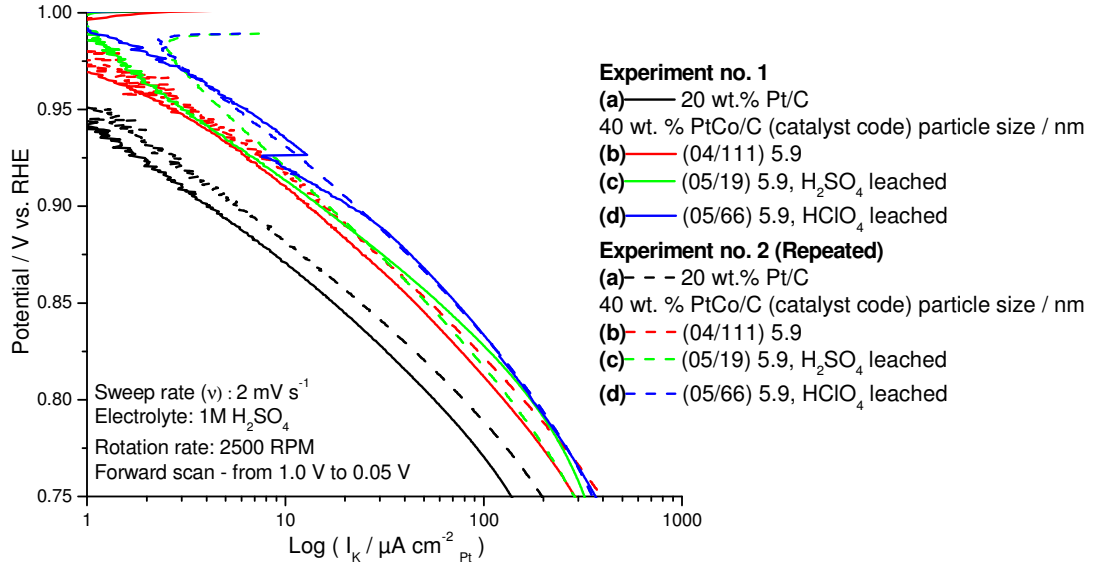

Figure 13 Tafel plots derived from the polarisation curves shown in Figure 12.

4.3 Binary catalyst composition effect

The effects of catalyst composition, Pt:Co ratio [4, 14-16, 31], were investigated using the set of catalysts described in Table 4. The polarisation curves and corresponding Tafel plots are shown in Figure 14 and Figure 15, respectively.

The best activity was found for the 87.5 wt % Pt, 12 wt % Co catalyst, corresponding to a Pt:Co atomic ratio of 2.2:1, with the 3:1 Pt:Co catalyst having similar activity for one of the replicates, but lower activity for the other.

Table 4 Catalysts used in experiments. Description of structure and composition parameters. (set 3)

No.	Catalyst code	Composition	XRD - Crystal Size / nm	XRD - Lattice Parameter / Å
(a)	-----	20 wt. % (Pt) / XC72R	-----	-----
(b)	04/111	40 wt% Pt (Pt:Co 3:1) / C	5.9	3.85
(c)	05/74	40 wt% Pt (Pt:Co 87.5 % Pt/12 % Co) / C	7.2	3.88
(d)	05/99	40 wt% Pt (Pt:Co 50 % Pt/50 % Co) / C	6.6	tetragonal

According to Paulus *et al.* [15] a small activity enhancement of 1.5 was achieved for 25 at % Co catalysts in comparison to pure Pt catalyst. An even more significant enhancement factor of 2-3 was reported for 50 at. % Co. Stemenkovic *et al.* [16] have studied Pt_3Co alloys in acid electrolytes. The same PtCo atomic ratios of 3:1 were tested having two different surface compositions: one with 75 % Pt alloy surface (sputtered) and

other 100 % Pt (annealed). The greater enhancement of ORR activity was observed for annealed catalysts with 'Pt-skin' over the catalyst where the surface was partially composed of Co. Antolini *et al.* [31] reported results collected for PtCo catalyst, with three Pt:Co composition ratios of 85:15, 80:20 and 75:25, and particle sizes of 8.5 nm, 6.7 nm and 4.6 nm respectively. The ORR activity at 0.9 V for those catalysts increased as Co content increased.

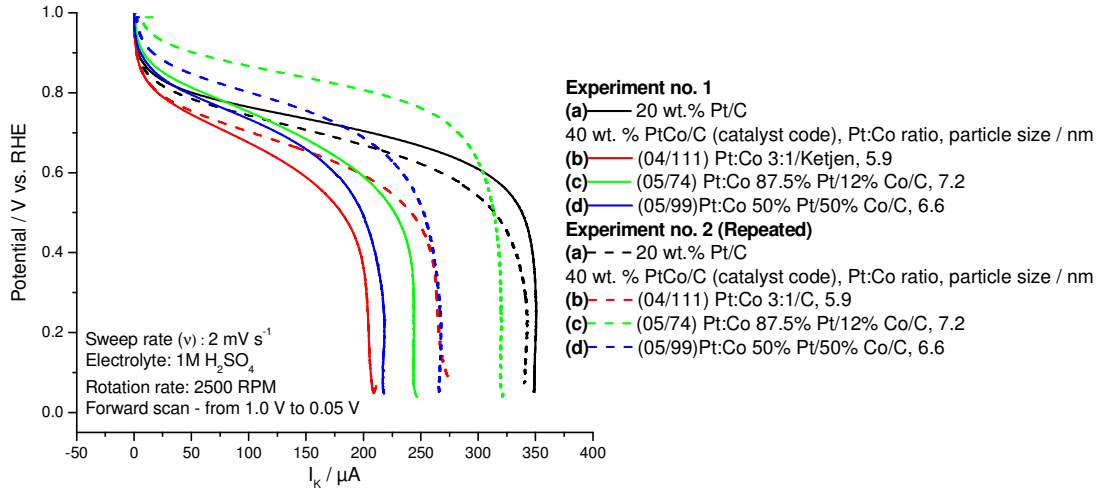

Figure 14 ORR polarisation curves collected for catalysts described in Table 4 using the RDE method. Both replicate experiments (identical colour) were run using the same catalysts and procedures.

Figure 15 illustrates the kinetic region plotted as Tafel plots. The best catalyst sample investigated in this experiment was (c) the 40 wt. % Pt (Pt:Co 87.5% Pt/12 % Co)/C and the worst 20 wt. % Pt/C catalyst. The activity increased in order (a) << (b) 5.9 nm (Pt:Co, 3:1) < (d) 6.6 nm (Pt:Co, 1:3.3) < (c) 7.2 nm (Pt:Co, 2.2:1) as the particle size increased. The interplay of particle size effect as well as composition ratio plays an important role in determination of ORR activity. However, the easiest criterion of classification of catalytic activities is particle size.

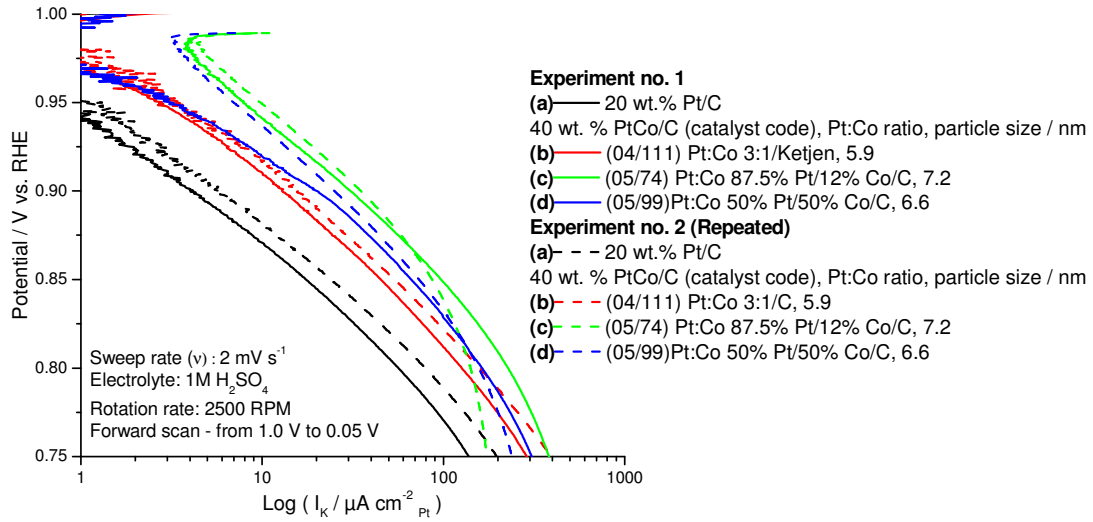

Figure 15 Tafel plots derived from the polarisation curves shown in Figure 14.

In conclusion, a clear trend of ORR specific activity was found for the experiments performed using the RDE method. The small difference in specific activities observed between two replicate measurements carried out for the same samples is therefore not significant.

5 Conclusions and Future Directions – Recommendations

The aims of the work reported in this chapter were to measure the ORR activities of a range of PtCo/C and Pt/C catalysts using the RDE method and to assess the RDE method as a rapid screening protocol. The results reported here reproduce the particle size and binary alloy composition effects on ORR activity reported in the literature. Thus, the technique appears to yield reliable results that enable ranking of catalysts.

While the RDE method yields useful data, it has several drawbacks as a rapid screening tool. First of all, the extended time required for measurement disqualifies this method as a rapid screening tool. It takes at least one month to collect the same amount of data as a high throughput method could achieve in one day. A second problem associated with this method is putting the drop of ink on the RDE disc. Many times when the drop is pipetted onto the surface of the electrode disc a non-uniformity of ink distribution occurs. The catalyst spreads out not only on the carbon disc but also on the PTFE isolating material that surrounds the disc. Moreover, variability in the mass of the catalyst ink drop between different experiments affects problems with mass activity estimation. Lack of knowledge of the real mass of the Pt catalyst deposited onto the disc means that the electrochemical area (ECA) cannot be calculated either. For this reason, the comparison of results with other available

methods such as fuel cell, mini cell measurements or half cell is impossible. The easiest and fastest way to enhance the quality of the data seems to be the improvement of the ink preparation method. Another important factor which causes difficulty is unequal electrolyte oxygen saturation in the separate experiments. Even a small variability of oxygen electrolyte saturation could affect the magnitude of currents tremendously.

The strengths and weaknesses of the method will be explained in Chapter 6, as well as comparison with 64 channel array and array fuel cell (25 channel) systems.

6 References

1. H. A. Gasteiger, S. S. Kocha, B. Sompalli, and F. T. Wagner, Applied Catalysis B-Environmental 56:9 (2005).
2. U. A. Paulus, T. J. Schmidt, H. A. Gasteiger, and R. J. Behm, Journal of Electroanalytical Chemistry 495:134 (2001).
3. T. J. Schmidt, H. A. Gasteiger, G. D. Stab, P. M. Urban, D. M. Kolb, and R. J. Behm, Journal of the Electrochemical Society 145:2354 (1998).
4. P. Hernandez-Fernandez, S. Rojas, P. Ocon, J. L. G. de la Fuente, P. Terreros, M. A. Pena, and J. L. Garcia-Fierro, Applied Catalysis B: Environmental 77:19 (2007).
5. R. Srivastava, P. Mani, N. Hahn, and P. Strasser, Angewandte Chemie-International Edition 46:8988 (2007).
6. D. Pletcher, Instrumental Methodes in Electrochemistry, Horwood Publishing, Southampton, 2001.
7. E. Higuchi, H. Uchida, and M. Watanabe, Journal of Electroanalytical Chemistry 583:69 (2005).
8. S. L. Gojkovic, S. K. Zecevic, and R. F. Savinell, Journal of the Electrochemical Society 145:3713 (1998).
9. F. Gloaguen, P. Convert, S. Gamburzev, O. A. Velev, and S. Srinivasan, in 1997 Joint International Meeting of the International-Society-of-Electrochemistry and the Electrochemical-Society, Pergamon-Elsevier Science Ltd, Paris, France, 1997, p. 3767.
10. J. Perez, E. R. Gonzalez, and E. A. Ticianelli, Electrochimica Acta 44:1329 (1998).
11. N. Markovic, H. Gasteiger, and P. N. Ross, Journal of the Electrochemical Society 144:1591 (1997).
12. O. Antoine, Y. Bultel, and R. Durand, Journal of Electroanalytical Chemistry 499:85 (2001).
13. T. J. Schmidt and H. A. Gasteiger, in Handbook of Fuel Cells - Fundamentals, Technology and Applications, Vol. 2 Electrocatalysis (W. Vielstich, Gasteiger, H. A., Lamm, A., ed.), John Wiley & Sons, 2003, p. 316 (Chapter 22).
14. U. A. Paulus, A. Wokaun, G. G. Scherer, T. J. Schmidt, V. Stamenkovic, N. M. Markovic, and P. N. Ross, Electrochimica Acta 47:3787 (2002).
15. U. A. Paulus, A. Wokaun, G. G. Scherer, T. J. Schmidt, V. Stamenkovic, V. Radmilovic, N. M. Markovic, and P. N. Ross, Journal of Physical Chemistry B 106:4181 (2002).

16. V. Stamenkovic, T. J. Schmidt, P. N. Ross, and N. M. Markovic, Journal of Physical Chemistry B 106:11970 (2002).
17. P. N. Ross Jr., in Handbook of Fuel Cells - Fundamentals, Technology and Applications, Vol. 2 Electrocatalysis (W. Vielstich, Gasteiger, H. A., Lamm, A., ed.), John Wiley & Sons, 2003, p. 465 (Chapter 31).
18. W. Vielstich, H. A. Gasteiger, and A. Lamm, Handbook of Fuel Cells. Fundamentals Technology and Applications, John Wiley & Sons Ltd., 2003.
19. P. P. Wells, Thesis for the degree of Doctor of Philosophy (2007).
20. T. R. Ralph, G. A. Hards, J. E. Keating, S. A. Campbell, D. P. Wilkinson, M. Davis, J. StPierre, and M. C. Johnson, Journal of the Electrochemical Society 144:3845 (1997).
21. T. Tada, in Handbook of Fuel Cells - Fundamentals, Technology and Applications, Vol. 3 Fuel Cell Technology and Applications (W. Vielstich, Gasteiger, H. A., Lamm, A., ed.), John Wiley & Sons, 2003, p. 481 (Chapter 38).
22. C. W. B. Bezerra, L. Zhang, H. Liu, K. Lee, A. L. B. Marques, E. P. Marques, H. Wang, and J. Zhang, Journal of Power Sources In Press, Accepted Manuscript.
23. K. Kinoshita, Journal of the Electrochemical Society 137:845 (1990).
24. H. A. Gasteiger, J. E. Panels, and S. G. Yan, Journal of Power Sources 127:162 (2004).
25. J. N. Soderberg, A. H. C. Sirk, S. A. Campbell, and V. I. Birss, Journal of the Electrochemical Society 152:A2017 (2005).
26. M. Watanabe, K. Tsurumi, T. Mizukami, T. Nakamura, and P. Stonehart, Journal of the Electrochemical Society 141:2659 (1994).
27. E. I. Santiago, L. C. Varanda, and H. M. Villullas, Journal of Physical Chemistry C 111:3146 (2007).
28. B. C. Beard and P. N. Ross, Journal of the Electrochemical Society 137:3368 (1990).
29. P. Yu, M. Pemberton, and P. Plasse, Journal of Power Sources 144:11 (2005).
30. M. Teliska, V. S. Murthi, S. Mukerjee, and D. E. Ramaker, Journal of the Electrochemical Society 152:A2159 (2005).
31. E. Antolini, J. R. C. Salgado, M. J. Giz, and E. R. Gonzalez, International Journal of Hydrogen Energy 30:1213 (2005).

Contents

Chapter Four: 64 channel wet array cell

1 Introduction

High throughput combinatorial testing methods have been in the spotlight of interest for the last couple of decades. Multichannel methods have elevated the science to a higher level of development. The main advantage of combinatorial or multichannel systems is the ability to measure a large number of samples in a relatively short time in comparison to single channel methods. In addition, great benefits are gained by investigating samples in the same environment. At the moment there is a need to produce, compare and choose the best catalyst out of a large number of formulations. The easiest way of finding the 'right' compound is to test samples using multichannel methods. Statistical analysis of the data should allow the estimation of the average performance values of the catalysts examined. In this manner, the catalysts displaying lower ORR activity can be quickly excluded from the 'good' candidates. Theoretically, the 64 channel array cell described in this chapter allows the testing of up to 63 different formulations simultaneously (one channel is blind). In practice, it is advisable to investigate up to only 8 catalysts at one time (8 channels per catalyst) to improve the statistical significance of the results.

The ideal wet cell system should meet the following criteria: high data reliability and reproducibility; easy to use and analyse the data; good sealing to avoid corrosion; hard to damage; and inexpensive. For this reason, further development of a previously published design was conducted and the results are described in this chapter.

1.1 History of high throughput methods

Over the last couple of decades, the development of high efficiency combinatorial methods [1] has been one of the important factors which have speeded up the discovery of new materials, catalysts, biological structures, capacitors, sensors, and many other compounds. Many institutes, companies and universities have been undertaking research in this area.

The first application of high throughput methods was made in screening biological compounds [2]. For this reason, fast screening became helpful in choosing the best biological compounds out of a wide range. Multi-channel systems were then developed for use in polymer synthesis [3], DNA recognition [4] and research on drugs [5] and materials science [6]. Large libraries of samples were tested simultaneously allowing the best performing compound to be chosen effectively. Since multichannel methods were applied, it was easier and faster to estimate the properties of the compound. High throughput methods

are still used in comparison to single channel methods but ideally in the future should be employed as a reliable source of information.

The first multi-element microelectrode arrays were reported by Glass *et al.* [7] in 1990 for electrochemical sensors. Their goal was to improve the quantitative information content from voltammetric measurements. High throughput methods were applied first by Reddington *et al.* [8] to study electrocatalysts using an optical screening method. Similar methods have subsequently been used in the development of oxygen reduction and water oxidation catalysts [9, 10] and the discovery of alloy electrocatalysts for amperometric glucose sensors [11].

A further step in the development of combinatorial methods for electrocatalyst screening was made by Fei *et al.* [12, 13], who described three different array geometries with differing numbers of channels (16 and 61) in the array.

High throughput electrochemical cells have been reported with various numbers of electrodes from 16 up to 244. For example, many 64 electrode operating systems have been reported [14-18]. Jiang *et al.* describe an electrochemical combinatorial system consisting of 144 separate probe chambers with working electrodes. The Smotkin group have been particularly active [19-23] and have reported a 25 channel DMFC cell with a serpentine array system which was used to screen anode catalyst in a real fuel cell environment.

In addition, multichannel combinatorial methods have been used to synthesise and screen heterogeneous ternary and quaternary electrocatalysts [15, 24-28]. An ideal combinatorial and high throughput workflow consists of synthesis and screening step of comparable synthesis. These techniques were classified as solution base, electrodeposition, and thin film, vacuum deposition methods. Vacuum deposition methods help to focus on the intrinsic activity of the materials, e.g. for ordered and disordered single-phase, metal alloys.

2 Experimental Details and Development

The 64 channel array screening technique described in detail below enables the testing of a large number of samples at the same time and in the same environment. This method allows trends in the characteristics and activities of a series of catalysts to be established more reliably than individual half cell measurements or the RDE method described in Chapter 3. Collection of replicate samples on the same array enables good statistics and allows estimation of the mean value of the catalytic performance of the samples.

This chapter is focused on developing a system for screening of the catalysts used at the cathode of PEMFCs (Proton Exchange Membrane Fuel Cells). Typically, Pt-based alloy

catalysts are used for oxygen reduction reaction (ORR) testing. Initially, the system components were the same as described by Guerin *et al.* [16]. Unfortunately, difficulties occurred with data quality and the results were not satisfactory. Many crucial issues arose concerning cell design, ink preparation, data acquisition and data processing methods. To overcome these problems, the array screening system has been redesigned to improve data quality. A comparison of old and new designs of the array cell is presented below in the next sections.

2.1 System components

Electrochemical characterization was performed on 64 vitreous carbon working electrodes arranged in an (8x8) array cell (Figure 1). The system is built from the following components: potentiostat, waveform generator, 64 channel array cell, and system of tubes, PCI-DAS6402/16 data acquisition card and the acquisition wizard software. 'The Analyzer' Visual Basic software developed by Guerin [16] along with popular available software packages such as Excel, Origin and Sigma Plot were used to analyse the data.

A three-electrode potentiostat was used with connection with a triangular Waveform Generator (PP RI HI-TEK INSTRUMENTS, ENGLAND) and a custom made 64 channel current follower 1 mA V^{-1} (max. 10 V) [16]. The waveform generator was programmed manually, setting the potential limits and scan rate. The 64 working electrodes in the cell were connected directly to the 64 channel current follower. The counter and reference electrode were attached to the potentiostat. The common counter electrode was a platinum gauze and the reference electrode was MMS, mercury-mercurous sulphate. The potentiostat communicated with the current follower through the waveform generator, whereas the current follower was connected to a PCI-DAS6402/16 data acquisition card, which was embedded into the PC (Pentium 4, 2.6 GHz, with XP professional operating system). The data acquisition card incorporated a high-speed PCI-bus compatible, 16-bit, 64-channel analogue input board with dual analogue output channels & 32 digital I/O bits. Operating with the large quantity of the data acquired during experiment requires large computer RAM memory (1024 MB) and a Pentium III processor (1.2 GHz). A gas delivery system was also constructed to connect the gas cylinders (CO, N_2, O_2) to the array cell to obtain efficient purging of the solution.

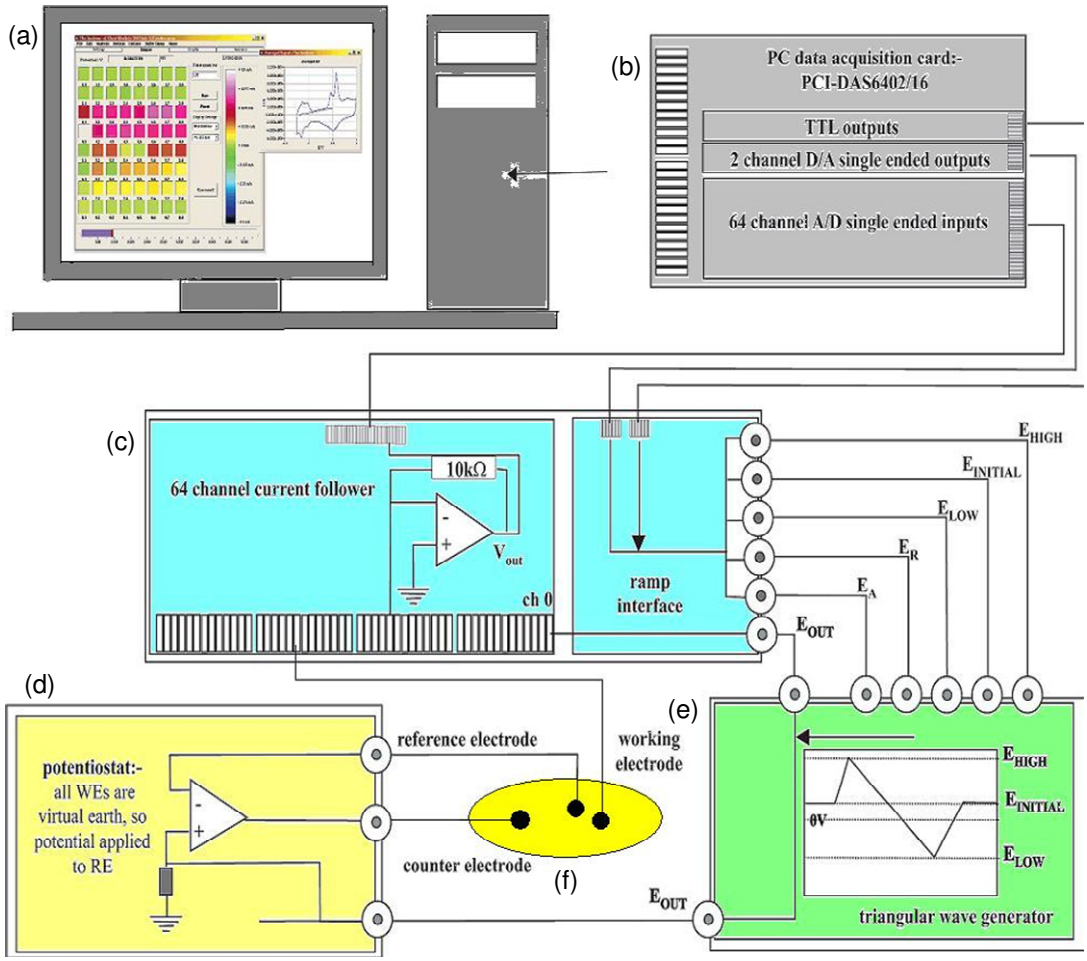

Figure 1 Schematic of the 64 channel array electrochemical control system developed for the combinatorial catalyst screening experiments. (a) The computer for data acquisition, (b) PCI-DAS6402/16 data acquisition card embedded into the PC (c) a 64-channel current follower, (d) a potentiostat, (e) a triangular sweep generator, and (f) an electrochemical array cell. [16].

2.2 Cell design

2.2.1 "Old" cell design

The old 64 channel array cell is shown in Figure 2. The whole cell was built mainly from Teflon parts (cell top, base array plate, bottom plate). The 3 mm diameter working electrodes were made from glassy carbon (SIGRADUR®G Rods) with 0.0705 cm^2 geometric areas. The spacing between the electrodes was 6 mm. The platinum gauze (counter electrode) was formed into a circle and placed around the array electrodes against the cell wall. The cell height was 20 mm and the top was covered with a glass lid having three holes in it. The reference electrode was inserted in the centrally located hole. Purging tubes were then positioned in the other two holes, which were aligned and situated at the same distance from the centre of the lid. The two glass tubes with frits provide gases to purge the solution.

The gases (oxygen, hydrogen and nitrogen) were used directly without additional humidification.

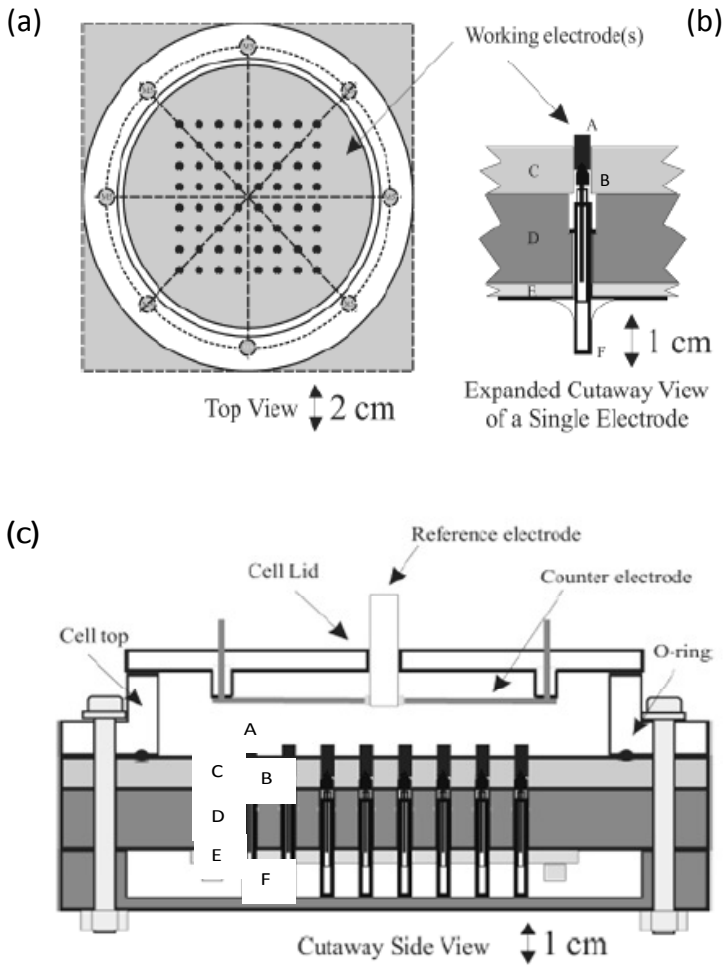

Figure 2 Schematic of 64 channel array cell. A - glassy carbon electrode, B - spring loaded electrical contact needle, C - PTFE array base plate, D - polypropylene contact holder, E - printed circuit board F - socket for electrical contact needle (a) electrode array from above (b) cutaway view of a single electrode (c) cross section of assembled cell. [16]

The weight of the cell is not significant, around one kilogram. The glassy carbon working electrodes were connected using spring loaded needles on the bottom side of the PTFE plate. This ensures good electrical contact. Spring needles were inserted into a socket crimp receptacle, which was soldered to the printed circuit board. The circuit board was connected by a 64 core ribbon cable to the current follower. The cell top was sealed against the base plate using a KARLEZ O-ring seal. The glassy carbon electrodes were sealed with glue to the PTFE base array plate.

2.2.2 "New" array cell design

Several experiments were carried out using the old design but they provided unsatisfactory results. Specific activities at a particular potential, e. g. 0.9 V vs. RHE, changed when two independent experiments with the same catalyst sets were run. The difference could be up to a factor of two using the same experimental parameters such as catalyst loadings, temperature and scanning procedures. The only merit was that the trends for a set of catalysts measured at the same time stayed approximately the same. With the aim of improving data quality and reproducibility, a redesign was completed. The new system was redesigned by me in such a way that it could be used to rank catalyst samples as well as to optimize loadings and the ink preparation.

For the new array cell, four important details were modified (Figure 3). Firstly, wider glassy carbon working electrodes (SIGRADUR®G Rods) were used, with 5 mm diameter compared to 3 mm in the previous cell; secondly, the cell top height was increased to 50 mm increasing the solution volume; thirdly, the counter electrode was placed above and parallel to the working electrode surface. Finally, the number of purging glass tubes with frits was increased to four.

As a result of electrode size modification the Pt catalyst mass in the catalyst suspension deposited on the top of the electrodes was greater, which improved data quality and reproducibility. The electrode diameter was increased from 3 mm to 5 mm (0.196 cm^2) and the spacing between electrodes changed from 6 mm to 4 mm. The decision to change the area of working electrodes was made for the following reasons. All the results could be compared with RDE, which has the same size (5 mm diameter) electrode, and applying the same loading and electrode geometric surface area on the array cell as for the RDE system helps with the comparison.

The second important change was the counter electrode position. Previously, the platinum gauze (counter electrode) ring was placed around the array, next to the cell top walls. This did not guarantee equal distances between each working electrode and the counter electrode. In the new system, the gauze was placed above and parallel to the working electrodes' surfaces. The platinum gauze is formed into a flat square and hung above the working electrodes from the cell lid.

In the old system, when the electrolyte was purged with gas, drops of 0.5 mol dm^{-3} sulphuric acid solution were splashed everywhere around the cell, despite the fact that the cell was covered with a glass lid. Hence, corrosion of the system connections occurred as well as damage to the insulation of the working electrode cables. This could damage the whole

system, opening unwanted electrical loops. A greater depth of solution was required to avoid spillage of acid electrolyte and to cover the counter electrode with the H_2SO_4 solution. The height of the cell top was increased; the walls now rise of 50 mm instead of 20 mm as previously. The volume of electrolyte can be greater, so it covers the reference electrode, purging tubes, frit tips and counter electrode more effectively.

The last modification made was the application of four purging tubes with frits instead of two to obtain a more uniform gas distribution. All the rest of the components have remained the same.

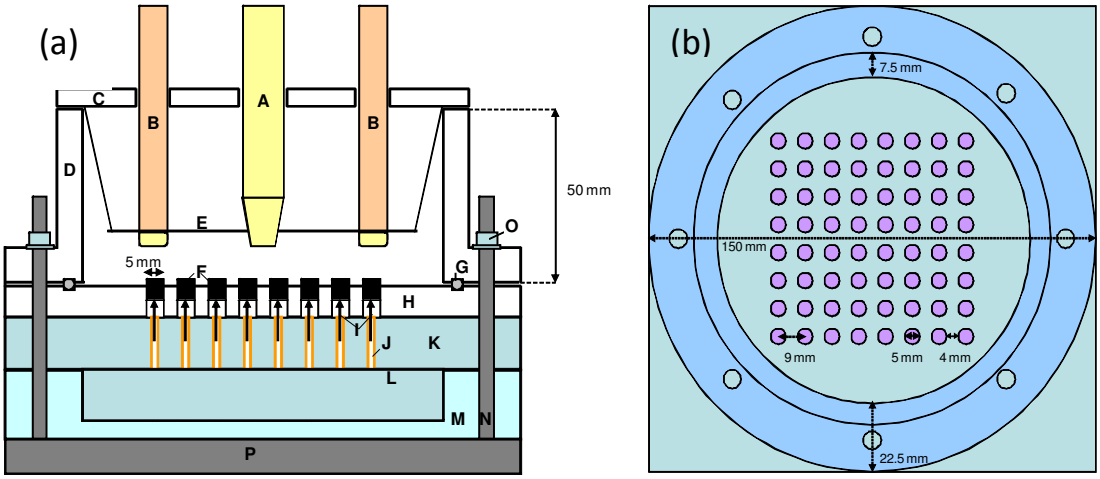

Figure 3 Schematic of the cell: (a) View from the side. A – reference electrode, B – gas purging tubes, C – cell lid, D – cell top, E – counter electrode, F – glassy carbon working electrodes, G – O-ring seal, H – glass filled PTFE array base plate, I – needle-point contacts, J – crimp receptacle for needle-point contacts, K – polypropylene contact holder, L – printed circuit board, M – polypropylene plate, N – long screw, O – nut, P – aluminium base. (b) View from the top (counter, reference electrodes and gas purging tubes removed).

In conclusion, the re-designed 64 channel array helps in the acquisition of more reliable data. The position of the counter electrode and the use of larger working electrodes improve the data quality and reproducibility.

2.3 Electrode cleaning

Before each experiment the PTFE plate with embedded vitreous carbon electrodes was cleaned with 98 % ethanol or iso-propanol using cotton wool. The plate was rinsed several times with high purity distilled water (16-18 MΩ cm). Afterwards the electrodes were polished with alumina powders with three particle sizes (0.3, 0.1 and 0.05 µm). The alumina was distributed uniformly on three separate pads and soaked with distilled water. The array plate was polished in a figure of eight for about 10 minutes using each type of alumina powder. This ensured that the surfaces of the electrodes were free from any impurities.

Subsequently, the array was rinsed several times with purified water. Particular attention was paid to this step, because the water can get underneath the plate causing corrosion and poor electrical contact with the pin needles. Finally, the plate was dried out using a heat gun.

2.4 Ink preparation methods

2.4.1 'Old' array

All the experiments carried out using the old array system were based on the ink preparation procedure as follows. 10 mg of electrocatalyst were mixed with 50 µl of 5 % Nafion® in alcohol (lower aliphatic alcohols and water) solution and 950 µl of water. The ink was mixed in an ultrasonic bath for around 90 min. The contents of the flasks with the ink were removed from the bath periodically and shaken to improve mixing.

Prior to application of the inks, the glassy carbon electrodes were cleaned as described in section 2.3. 4 µl aliquots of this ink were pipetted onto the 3 mm diameter (0.071 cm^2) electrodes and left for several hours to dry.

2.4.2 'New' array

Two ink preparation methods were used with the new array.

2.4.2.1 Water based ink

Water based inks were used for most of the experiments carried out using the new array. The inks were prepared by mixing 10 mg of electrocatalyst with 50 µL of 5 % Nafion® in low weight alcohol solution and either 950, 2950, 4950 or 6950 µL of water in an ultrasonic bath. 20 µL aliquots of the ink were pipetted onto identical 5 mm (0.196 cm^2 area) diameter electrodes.

2.4.2.2 Chloroform based ink

Chloroform based inks were used to facilitate comparison with the RDE experiments reported in Chapter 3. The inks were prepared by mixing 10 mg of electrocatalyst with 10 mL of chloroform sonicated in an ultrasonic bath for an hour. A 5 µL aliquot was deposited on the 5 mm diameter vitreous carbon electrodes (0.196 cm^2) and allowed to dry. Subsequently 50 µL of a 5 % Nafion® in alcohol solution was mixed with 4950 µL isopropanol and a 5 µL aliquot was pipetted on the dry catalyst layer previously deposited on the electrode.

2.5 Comparison of ORR experiments using the 'old' and 'new' 64 channel systems.

An investigation of a series of 40 wt. % Pt/C catalysts was performed and the details of the catalysts are given in Table 1. The 20 wt. % Pt/C reference catalyst [29] was also included. These measurements concentrate on the oxygen reduction reaction (ORR) through an examination of cathode catalysts. Comparison of the results from four experiments carried out using the two different 64 channel array cells described in section 2.2 was made to explore the reproducibility of this method. Each experiment was performed in duplicate for each type of cell.

Table 1 Catalysts used in experiments (description of pre-treatment and parameters)

No.	Catalyst code	Composition	XRD - Crystal Size / nm	XRD - Lattice Parameter / Å
(a)	-----	20 wt. % (Pt) / C	-----	-----
(b)	05/75	40 wt% Pt / C	4.7	3.93
(c)	04/131	40 wt% Pt / C	7.7	3.92
(d)	05/79	40 wt% Pt / C	15.6	3.93

All the MMS reference electrode calibration, inks and working electrode preparation procedures were identical as depicted in section 2.4. The MMS electrode was calibrated to RHE (reversible hydrogen electrode) scale before each experiment. Thus, all potentials are reported against the RHE scale; it also eases the comparison of this with other methods.

The measurements were run using the old cell with 3 mm diameter electrodes. Figure 4 (A) and Figure 5 (A) present the CV and ORR experiments, respectively. The loading of the Pt catalyst deposited on the glassy carbon electrode should be 40 µg, corresponding to 16 µg of platinum for 40 wt. % Pt/C, and 8 µg of platinum for 20 wt. % Pt/C catalyst. In other words, the platinum loadings per geometric electrode area were 0.225 mg cm^{-2} and 0.112 mg cm^{-2}, respectively. In practice, it is very difficult to know the real Pt loading in one drop pipetted onto the vitreous carbon electrode. The micro pipette used only 5 µL volume of the ink solution in this experiment; therefore the error could be significant. Such a small volume of solution could include various amounts of catalyst dispersed in it and could result in an error of two or three times the desired mass of platinum. As a result, it is not possible to accurately estimate mass activity (A mg_{Pt}^{-1}). For this reason, the only reliable value is the specific activity (A cm_{Pt}^{-2}). The raw currents obtained during the experiment were normalized by the Pt real surface area. Pt real surface areas were calculated from the CO stripping peak and hydride adsorption regions, as described in Chapter 2.

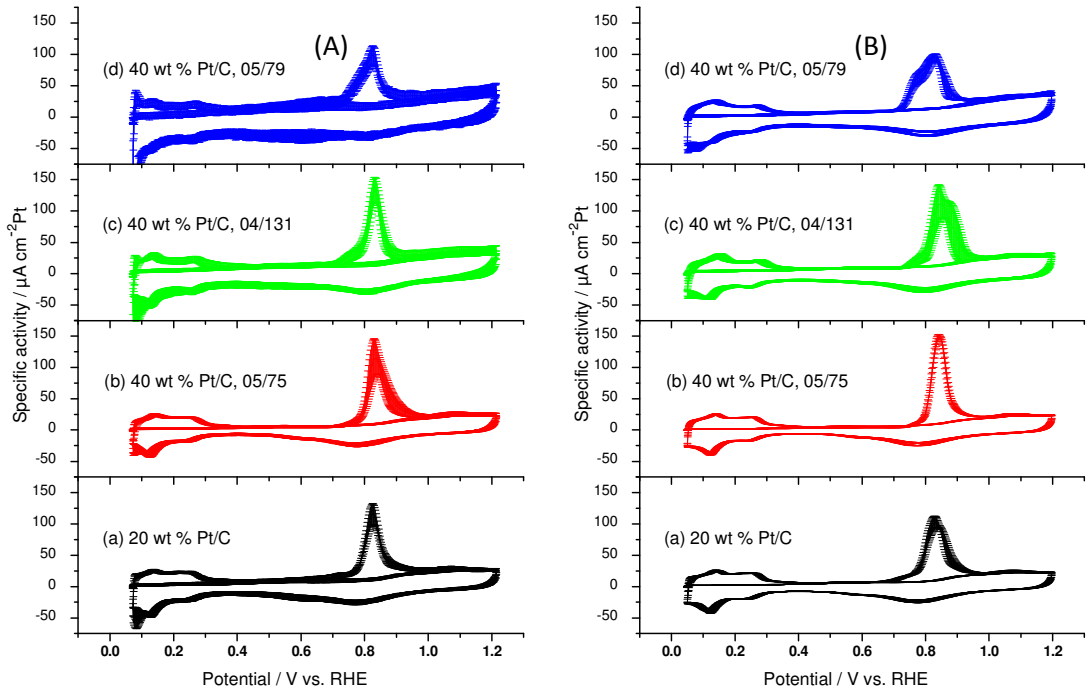

Figure 4 Comparison of cyclic voltammograms acquired for both experiments no. 1 depicted in this section using (A) old 64 channel array and (B) new array systems. Voltammograms show the average with associated standard deviations (as error bars).

Figure 4 shows the average cyclic voltammograms with their associated standard deviations shown as error bars. The experiments described as no. 1 were shown as a representative example for the difference between using 'old' and 'new' 64 channel cells. Comparing the CVs for the same set of catalysts, it can be seen that the standard deviation error bars are much broader for the 3 mm diameter vitreous carbon electrode cell, for which the results are thus less accurate. Ideally, after the CVs were normalized by Pt real surface area, the specific activity should be identical. In practice, some variation remains and is interpreted as the error associated with the measurement. The standard deviation error bars (colour area of the voltammograms) for data acquired using the new 5 mm diameter electrodes system were less significant compared with the old system. The largest difference occurred between results obtained for 40 wt. % Pt/C (05/79). The data acquired using the new cell presented uniformity compared to the old cell. In conclusion, the electrodes are larger, the more uniform and accurate the data was.

As seen in Figure 5A, the curves show similar trends in both experiments; however, the absolute values are not identical. Problems occurred for the catalyst with average particle diameter of 4.7 nm (b) 05/75 and the (a) 20 wt % Pt/C, where the curves from the same catalyst do not superimpose. Furthermore, the average Pt catalyst real surface areas varied significantly between two experiments (Figure 6A); this observation highlights that any

inaccuracies in the inks and electrode preparation were crucial factors which determine such a difference in the results. In addition, the geometrical area of the electrode also plays an important role. Smaller volumes of catalyst ink can be deposited onto the 3 mm diameter electrodes in comparison to the new cell with 5 mm diameter electrodes. Increasing the volume of the ink drop can stabilize the average mass of the catalysts, and this is reflected in the smaller differences between electrodes of the same type (Figure 6B) using the layer electrodes.

In the water ink preparation method (see section 2.4.2.1), the same mass of catalyst was diluted five times more in volume with water, and therefore 5 mL was used. This ensured a more equal catalyst distribution in the ink suspension. A larger volume of ink solution (20 µL) then corresponded to the desired mass of the catalyst (40 µg) deposited. The only difference was that the new electrode (5 mm diameter) had a much greater geometrical area (0.196 cm^2) which gave lower Pt loading of 0.0816 mg cm^{-2}.

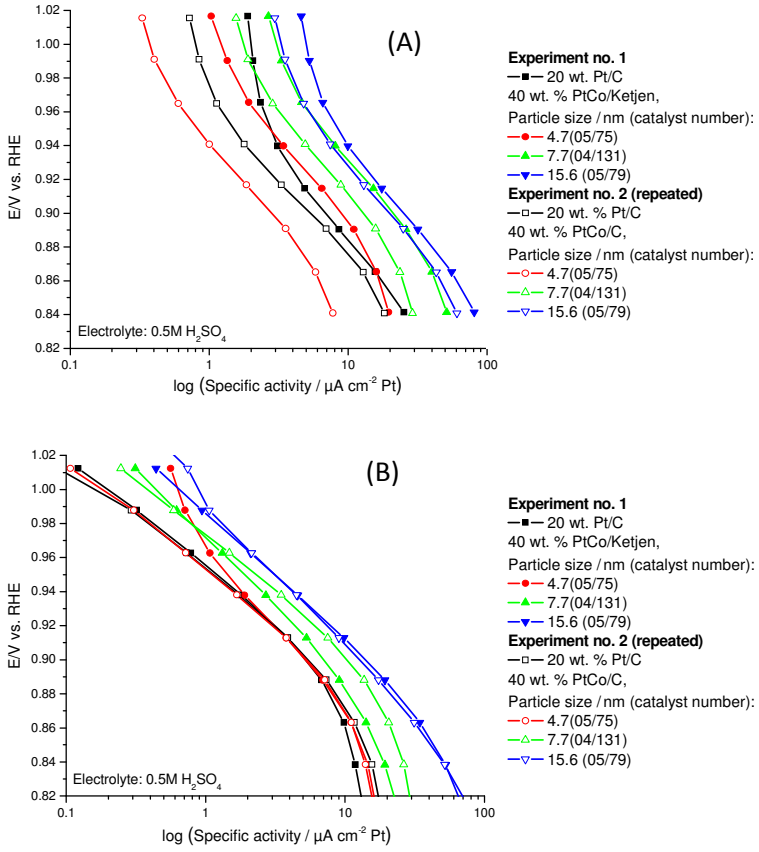

Figure 5 Tafel plots - Comparison of 40 wt % Pt/Ketjen catalysts series along with the 20 wt. % Pt/C reference catalyst. Two replicates were completed for each experiment. The experiment was carried out at room temperature in 0.5 mol dm^{-3} H_2SO_4 electrolyte. The measurements were run on (A) old array with 3 mm diameter electrodes, (B) new array with 5 mm diameter electrodes.

Figure 5B shows results from the experiments carried out using the new cell with larger electrodes. Following the enhancements made by redesigning the electrode size, counter electrode position and improving the ink preparation method, the quality of the data increased. The data points of three out of four catalysts perfectly overlap at potential 0.9 V vs. RHE between the two separate experiments. Similarly, the trends agreed with each other. The best performance was obtained for the sample with a particle diameter of 15.6 nm (d) 05/79. The second best specific activity presents a sample with a 7.7 nm particle (c) 04/131. The worst performance was obtained for both catalysts with a particle diameter 4.7 nm (b) 05/75 and (a) 20 wt. % Pt/C, as expected. In conclusion, as the particle diameter decreases the specific activity increases. Similar studies and results considering particle size effect on Pt/C catalysts were carried out by Kinoshita [30] and revealed the same relationship between particle size and ORR activity.

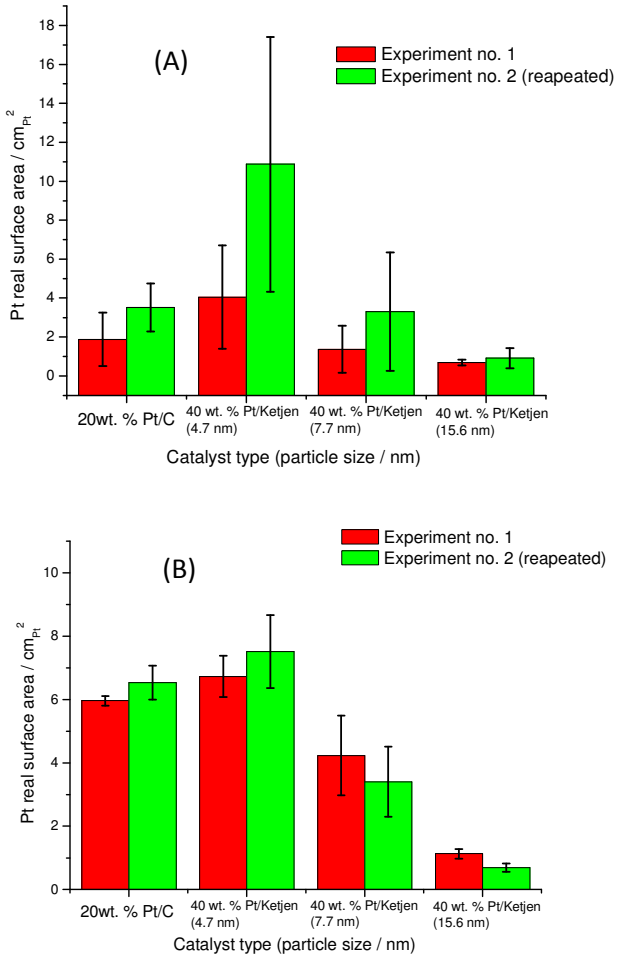

Figure 6 Pt real surface area as a function of particle size for both replicates using (A) the old array cell (3 mm diameter electrodes) and (B) the new array cell (5 mm diameter electrodes) to illustrate the greater reproducibility of the redesigned cell.

As can be seen by comparing Figure 5A and B, the new design yields much more reproducible results. Of particular importance is reproducibility in the kinetic region 1.00 – 0.88 V. The data are less reproducible in the mass transport controlled region, E < 0.88 V, and this is accounted for by variations in the O_2 saturation of the solution and electrode thickness. Thicker catalyst layers on the electrode pins result in poorer oxygen mass transport and utilisation of the full surface area of the catalyst.

2.6 Data analysis

High throughput methods have recently become a very useful tool in the analysis of a vast range of samples. Multichannel systems today are an area of chemistry, which is developing fast, but they still have not become a major area of interest. On the other hand, thirty years ago no one would have expected that the need for fast screening would lead to such a variety of systems. The types of apparatus being constructed are constantly improving in their simplicity, quality and reliability. For this reason, the equipment is becoming with time more user friendly. For instance, in the past the user had to attend the test at all times while the experiment was running. Now, particular attention during the experiment is not required. The process has in many cases been automated. Procedures have become simpler and even a non-fully-qualified user can carry out an experiment. Unfortunately, the experimental procedure issue is not the major inhibiting factor in the development of high throughput combinatorial methods. However, the data processing is one of the major aspects which prevents fast business growth in this area. Data analysis remains the most difficult step in the whole process of investigation of the properties of the compounds. It requires a lot of time and sufficient skills in operating software, as well as good scientific knowledge. Inexperienced users can become confused in the calculation process when operating with large quantities of data points. For this reason, there is a need to create software to help with data analysis. On the other hand, it is possible to use standard, commercially available software such as Excel, Origin and Sigma Plot. The researcher familiar with each of those software packages should have no problems with data processing. The following data analysis for a 64 channel array system is depicted below.

The process commences when the data are acquired by the ‘Acquisition Wizard’ Visual-Basic-based program [16]. This program has a range of features, which help to determine specific cyclic voltammogram characteristics, for example peak charge leading to Pt real surface area calculation. The program allows the experimenter to display the cyclic voltammogram, the current transient or the charge transient. Moreover, the user can display and observe the current response of 64 electrodes simultaneously using a false colour response window. The data from one experiment are saved in three files with extensions (*file*

*name*_Currents.dat, *file name*_Charges.dat and *file name*_infofile.txt). The first step in data processing was performed using 'The Analyzer', Visual-Basic-based software. A raw data file was loaded into the Analyzer. The procedure for opening a file was as follows. The file pathway to the experimental data was initially found, and then the extension was deleted and the file was opened using one large file option, e.g. when opening the file '051007-2Currents.dat', the 'Currents.dat' extension was deleted before opening the file. After the data file had been opened, the CVs for each of the 63 different electrodes were observed using a graph function window. In order to carry out an integration calculation for the peak charge, the positions of the CO stripping peaks were carefully monitored. Two integration potential limits (V) were then set, the first being the electrode potential at the onset of the CO stripping peak (approximately -0.1 V in most of the experiments) and the second being the potential at the end of the peak (around 0.3 V in most experiments). The different cycles were separated and integration was carried out. The integration peak charge results were saved. The next step was to calculate Pt real surface area using the obtained 64 peak charges with the previously combination of the equations described in chapter 2, section 3.2.

After the initial calculation of all 64 CO peak charges was completed, Excel was employed to carry out statistics calculations with the purpose of obtaining average values and associated standard deviations. The macros and templates were created for use in future data processing. The user can import the data and templates do most of the computation automatically. Secondly, Sigma Plot was used to plot highly complicated graphs with 64 small graphs ordered in 8x8 configurations. The graph templates once created may be used as many times as needed. In addition, Sigma Plot was used for the elimination of poor data and the normalisation of the currents to the Pt real surface area. Sigma Plot was similarly used in the analysis of the data for the ORR and the plotting of Tafel plots. Thirdly, Origin software was used in a similar way as Sigma Plot. Comparing both, Origin has better functions for plotting graphs, applying colours and other detailed functions. Each software package can be used separately from the others. It depends on the researcher's preferences as to which software is the most convenient to use. All the calculations made were similar and typical for conventional single electrode system analysis, with the difference that all the analysis was carried out for 64 channels at a time.

Many limitations of chemical measurements occurred during catalyst testing. In fact, there are many obstacles such as faulty connections, different catalyst distribution on the array, etc. Problems leading to inaccurate results include current offsets – positive or negative currents, insufficient electrode cleaning, electrode resistance (high iR drop), and poor connections (noise and corrosion) between the electrodes and the current followers. Common features of inaccurate CVs arising from faulty electrodes are shown in Figure 7.

Consequently, the data processing cannot be fully automatic. Poor data quality electrodes have to be eliminated manually from the calculations. The data channels showing such poor data were not used in the data analysis in order to minimise associated errors.

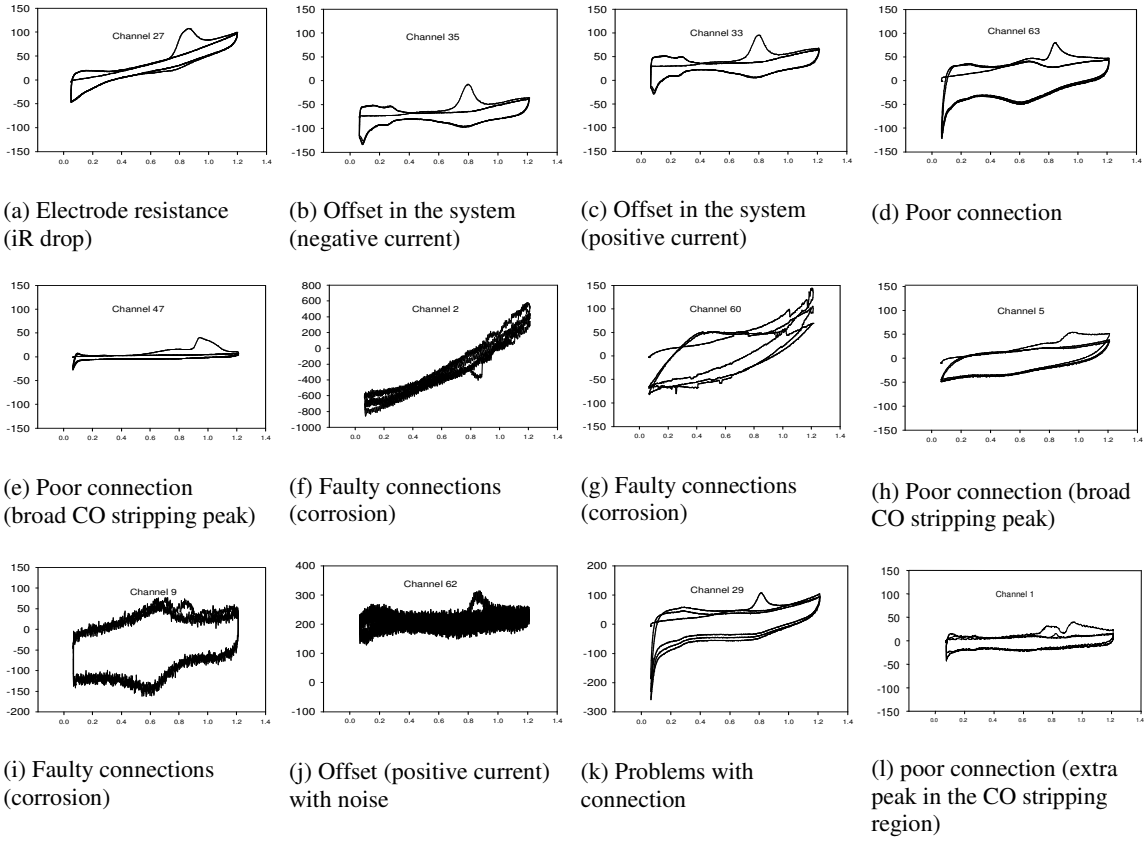

(a) Electrode resistance (iR drop)

(b) Offset in the system (negative current)

(c) Offset in the system (positive current)

(d) Poor connection

(e) Poor connection (broad CO stripping peak)

(f) Faulty connections (corrosion)

(g) Faulty connections (corrosion)

(h) Poor connection (broad CO stripping peak)

(i) Faulty connections (corrosion)

(j) Offset (positive current) with noise

(k) Problems with connection

(l) poor connection (extra peak in the CO stripping region)

Figure 7 Series of CO stripping voltammograms corresponding to poor, unreliable data which were eliminated from the data processing. The X scale in each panel shows potential from -0.2 to 1.4 V vs. RHE. The full Y scale in each panel presents the currents / µA.

2.7 Further development

The 64 channel array system needs further development. The most important challenge is to eliminate problems affected by acid corrosion in the system. The working electrodes are embedded into the PTFE base plate, which comprises the bottom of the reaction chamber. During the experiment the cell is filled with 0.5 mol dm^{-3} of sulphuric acid. As a result, the electrodes do not have a good seal and acid penetrates the gaps between the PTFE plate and the glassy carbon electrodes. The result of this is corrosion of the connections on the bottom side of the vitreous carbon rods. The printed circuit board position underneath the pin spring-loaded connections can also be affected by acid corrosion. In summary, the sealing of the working electrodes needs to be improved. If this does not work, a change in the whole design of the cell would need to be made. For instance, the working electrode could be positioned on the top side of the cell. Therefore, the acid could not infiltrate against force of gravitation. In brief, the connections would stay untouched by corrosive sulphuric acid.

Specialised new software needs to be developed. The time-consuming nature of data processing is a crucial factor, which limits the ability to screen samples and analyse large quantities of data. Decreasing the time significantly should speed up the process by a factor of four.

3 Reproducibility

In order to prove whether or not the data acquired during 64 channel array testing were reproducible, a range of experiments was carried out. Specifically, the same 20 wt. % Pt/C catalyst was tested on all of the electrodes. The ink preparation methods described below were the only difference in the testing procedure. The conditions of temperature, pressure and electrolyte were the same. Finally, the results for both CVs and ORR polarisation curves were expected to be identical for all the channels.

3.1 Cyclic voltammetry

Prior to commencing measurements, the electrodes were pre-treated for half an hour as follows. The potential was cycled between 0.06 V and 1.21 V vs. RHE, at 20 mV s^{-1} in 0.5 mol dm^{-3} H_2SO_4. The experiments were generally carried out between those limits to prevent any damage to, or deterioration of, these ORR catalysts. Any excursion of potential above and below the limits could damage the structure and change the properties. To remove dissolved oxygen, the acid solution was then purged with nitrogen for 30 minutes before the experiment. Three CV scans for carbon-supported platinum catalysts were run again between the same potential limits as shown above. All the potentials reported were corrected to the RHE scale. The data were acquired and saved with the Acquisition wizard (Visual Basic software).

The actual carbon monoxide (CO) stripping experiment performed after the CVs pre-scan looked satisfactory. This means that the connections were set properly, giving clear CVs. The electrolyte was purged with CO (g) for 30 minutes. Subsequently, any CO remaining in the bulk acid solution was removed by purging with N_2 for 30 minutes before the scanning commenced. At all times when gases were purged, the potential was kept at 0.06 V. This assured bonding of CO (g) to the Pt active crystal sites of the electrodes. Similarly to pre-CV scans, the potential was swept between 0.06 V and 1.21 V, starting from 0.06 V at a scan rate of 20 mV s^{-1} and CO stripping scans were then acquired. The data presented show only CO stripping CV along with subsequent CV.

All the CO stripping voltammetry scans for a 20 % wt. Pt/C are shown in Figure 8 (currents without normalisation) and Figure 10 (currents normalised by Pt real surface area). All the

electrodes were divided into groups with different loading of the same 20 wt. % Pt/C catalyst. In the experiment, four catalyst inks in total were used with two volumes of each ink deposited on the 64 channel array electrodes. In this case faulty electrodes, channels 8, 32, 33 and 48, were not involved in the data processing.

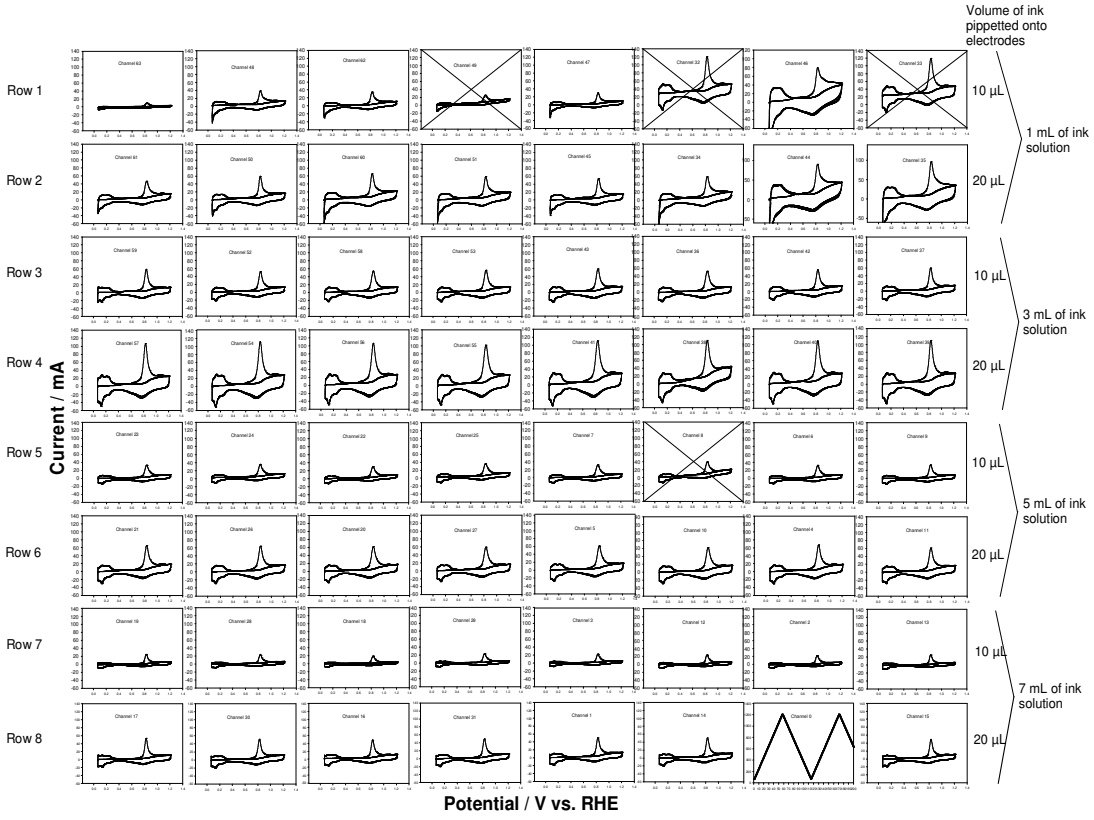

Figure 8 Reproducibility test for 20 wt. % Pt/C catalyst. 63 CO stripping voltammograms (raw data - currents) acquired at room temperature, (1st and 2nd scan) after H_2SO_4 electrolyte was purged with $CO_{(g)}$ for 15 min and $N_{2(g)}$ for 30 min. The potential was held at 0.05 V for 45 min at the time the gases were purged through the solution. The scan limits were 0.05 and 1.2 V and scan rate was 20 mV s^{-1}. Rows represent different volumes of water in the ink, which dilute 10 mg of the 20 wt. % Pt/C catalyst along with 50 µL of 5% Nafion in alcohol solution. Each type of ink was distributed in two different volumes onto electrodes (10 and 20 µL). Crosses (X) on the graphs correspond to faulty electrodes (resistance – iR drop and current offset) and are not included in the data processing. The scale of potential in each panel is -0.2 to 1.4 V vs. RHE. Full scale of current for each panel is -60 to 140 µA.

Firstly, Pt real surface areas were calculated using hydride region adsorption peak charges. The peak charges were corrected using double layer correction. Secondly, the active areas of the platinum catalysts were determined by the oxidation of an adsorbed monolayer of carbon monoxide. The Pt real surface area calculations using both methods were described in Chapter 2, section 3.2.

Figure 9 shows the comparison of Pt real surface area extracted from CVs after the CO stripping experiment. Figure 9 (a) shows Pt real surface determined from CO stripping peak

charge, and Figure 9 (b) represents Pt area calculated using hydride peak charge. In theory, CO peaks should have a charge twice those of hydride region peaks. The ink prepared using one method was distributed evenly in two rows in two different volumes, 10 and 20 µL. For this reason, row 1 should possess half the value of row 2. Unfortunately, those rows do not agree with this correlation, as indicated by the larger error bar. Eight electrodes were averaged for each volume. The explanation is in the huge error (standard deviation) bar. In other words, the ink preparation method and distribution on the array are not sufficient in this case. On the other hand, row 3 and row 4 do display such a relationship. The error bar is not significant. This means there is not much difference in Pt real surface area between CVs positioned in the same rows. Similarly, rows 5 and 6 and rows 7 and 8 also display such behaviour. This dependence establishes both methods as trustworthy.

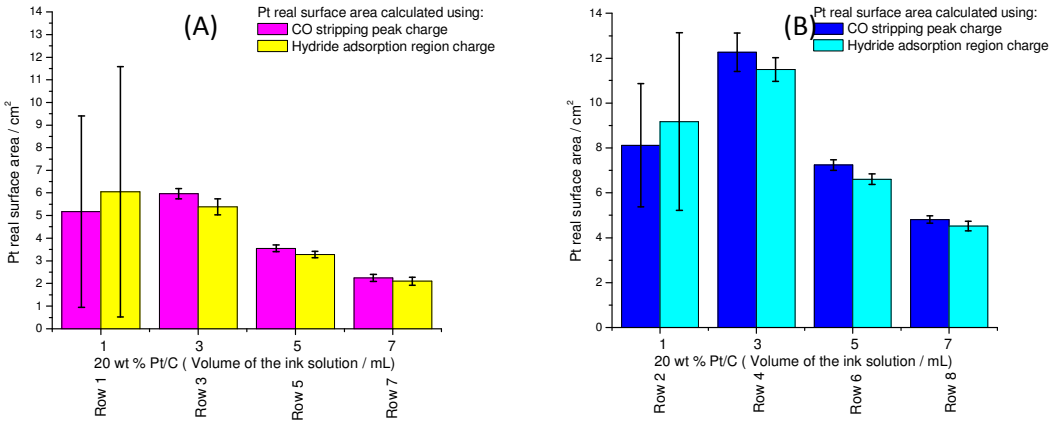

Figure 9 A study of the effect of solvent volumes on Pt real surface area using CO stripping and hydride region. Average results of Pt real surface area calculated using CO stripping peak charge and hydride adsorption region peaks charge methods. Standard deviations stand for the variations in between electrodes Pt real surface area. Accordingly, 1, 3, 5 and 7 mL of water (solvent) were used to disperse 10 mg of 20 wt. % Pt/C catalyst along with 50 µL of 5% Nafion in alcohol solution. Each catalyst ink (a) 10 µL and (b) 20 µL volume drop were pipetted onto glassy carbon 5 mm diameter (0.196 cm^2) electrodes.

Figure 10 shows the same CVs as presented in Figure 8. The only difference in this case was that CV currents were normalised by the Pt real surface areas and the graphs look similar, displaying almost identical specific activity and having the same scale. This confirms that the same catalyst provides the same values after data processing. In addition, all average maximum CO stripping peak potentials had value of 831 mV (± 2 mV). Finally, the peaks stayed approximately in the same position, which suggested that results were consistent and reproducible.

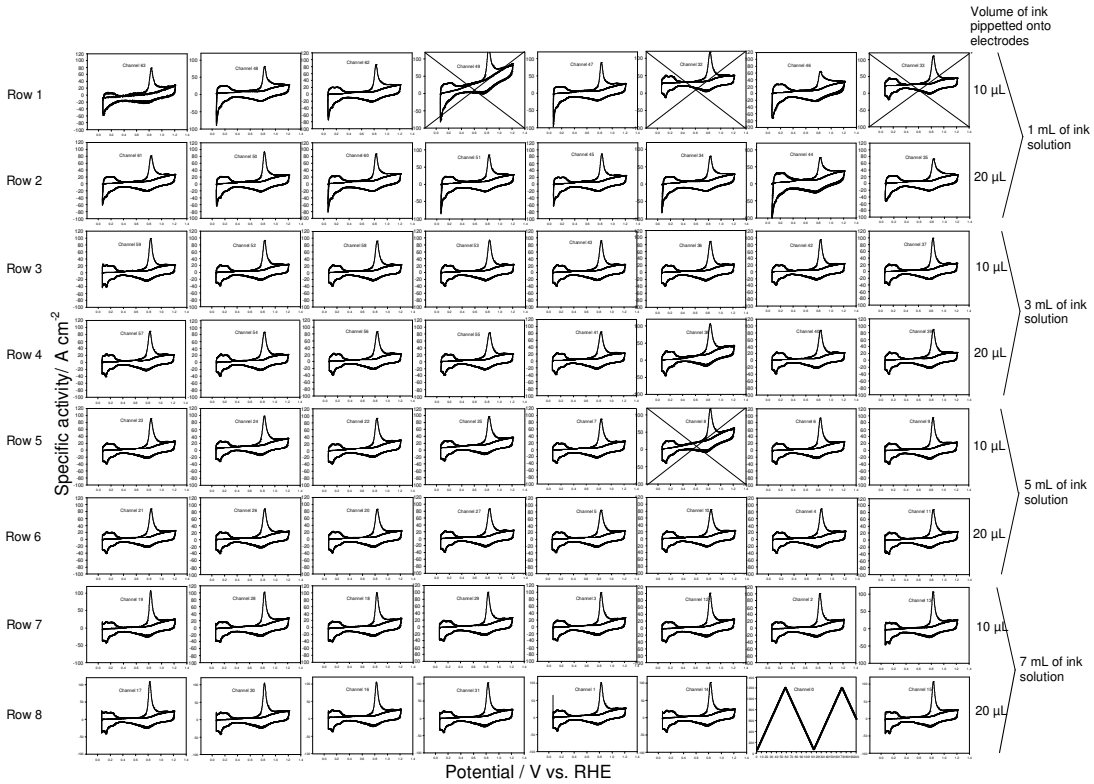

Figure 10 Reproducibility test using 20 wt. % Pt/C catalysts showing the same 63 stripping voltammograms as in Figure 8 but in this case normalised by Pt real surface area. All the experimental details are identical as depicted in the Figure 8 caption. The scale of potential in each panel is -0.2 to 1.4 V vs. RHE. Full scale of specific activity for each panel is -100 to 120 µA cm^{-2}.

3.2 ORR

The main purpose of constructing the 64 channel array screening system was to measure ORR kinetics of Pt based catalysts. Hence, a range of experiments was carried out with the purpose of trusting and understanding the system. One of the most important aims was to achieve the ability to measure 64 different Pt catalyst formulations simultaneously. The advantage of this system was the potential for using statistical methods in order to eliminate the factors connected with experimental errors. Single channel methods such as 'wet' half cell do not guarantee reliability and reproducibility in ORR testing. In this system, the mass transport controlled region is not sufficiently controlled. Thus, dissimilarity in the results of two replicate experiments occurred and the data provided are dissimilar. In theory, as shown in RDE experiments [31, 32], the mass transfer controlled region should not influence the kinetic region of ORR. Unfortunately, for a single electrode system, the problem with data quality led to the conclusion that some difficulties occurred. It was very hard to estimate what is the main problem in a single electrode system.

An experiment was run to resolve this problem and to prove the reproducibility of ORR for multichannel 64 array cell. Statistical analysis can disclose problems much faster than conventional single electrode systems. Polarisation curve experiments were carried out using the same 20 wt. % Pt/C catalyst with different ink preparation methods. The experiment was performed in this same cell after the CO stripping measurements described in the section 3.1 of this chapter.

The electrolyte was purged for 20 minutes prior to and then continuously during measurements with oxygen. The potential was stepped between 0.5 V to 1.2 V vs. RHE and held for 50-second intervals. The potential increments (steps) were 25 mV. The same measurement procedure was used for all the Pt catalysts series tested. The data were analysed with The Analyzer (Visual Basic software) programme and commercially available software such as Excel, Origin and Sigma Plot.

The ORR average Tafel plots for varying ink volumes were plotted and are compared in Figure 11. The catalyst used in this experiment was 20 wt. % Pt/C. The descriptions of the whole solution ink volumes are given in mL and µL for the volume pipetted onto the electrodes accordingly. From Figure 11, it is clear that the Tafel plots for 6 out of 8 inks overlap in the kinetic region, which is placed between 0.825 V and 0.95 V. This means that the ink preparation methods are reliable only for 3, 5 and 7 mL catalyst water dispersions. The 1 mL ink solution did not disperse catalyst uniformly. For this reason, the Pt was not distributed sufficiently onto vitreous carbon electrodes. Above potentials of 0.95 V, a large range of log (specific activity) occurred. The reason is the kinetic controlled limiting current which is placed near zero and in the logarithmic small deviations are amplified. In reality, if the scale is changed to a linear scale, the differences are insignificant.

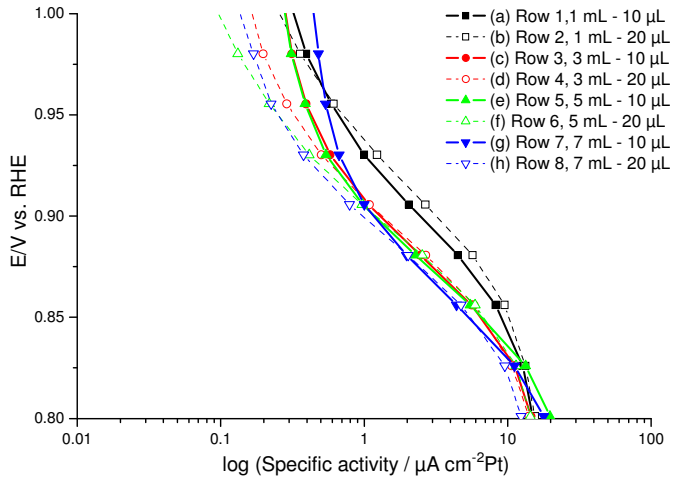

Figure 11 An effect of ink preparation methods on data reproducibility. Average values of 20 wt. % Pt/C catalyst with different dispersions of ink were examined and plotted for comparison.

Furthermore, all the Tafel plots shown in Figure 12 represent all 64 electrodes excluding faulty channels. It can be clearly seen that data obtained using 1 mL (a), (b) ink dispersion are not acceptable in catalyst screening. The Tafel curves do not superimpose and the data are not consistent. The curves plotted using 7 mL (g), (h) ink solution show a discrepancy among electrodes with the same loading. On the other hand, some of the curves overlap and display similar specific activity, which suggests that the catalyst was dispersed in too high a volume of water. Conditionally, this ink dispersion should not be used in catalyst testing. The smallest difference between results occurred for 3 mL solution and 5 mL solution. This suggests that the methods including 3 and 5 mL solutions were the most reliable and reproducible. In addition, each of four inks was deposited in two different volumes: 20 μL drops and 10 μL drops. As a result, the mass of Pt was twice as large for 20 μL, and thus more likely to stay identical on all the electrodes. In summary, the 5 mL ink with 20 μL aliquot was chosen and established as a procedure in catalyst testing for the 'new' 64 channel array. All the experiments reported in further work were completed using this catalyst dispersion and volume of ink deposited onto the electrodes.

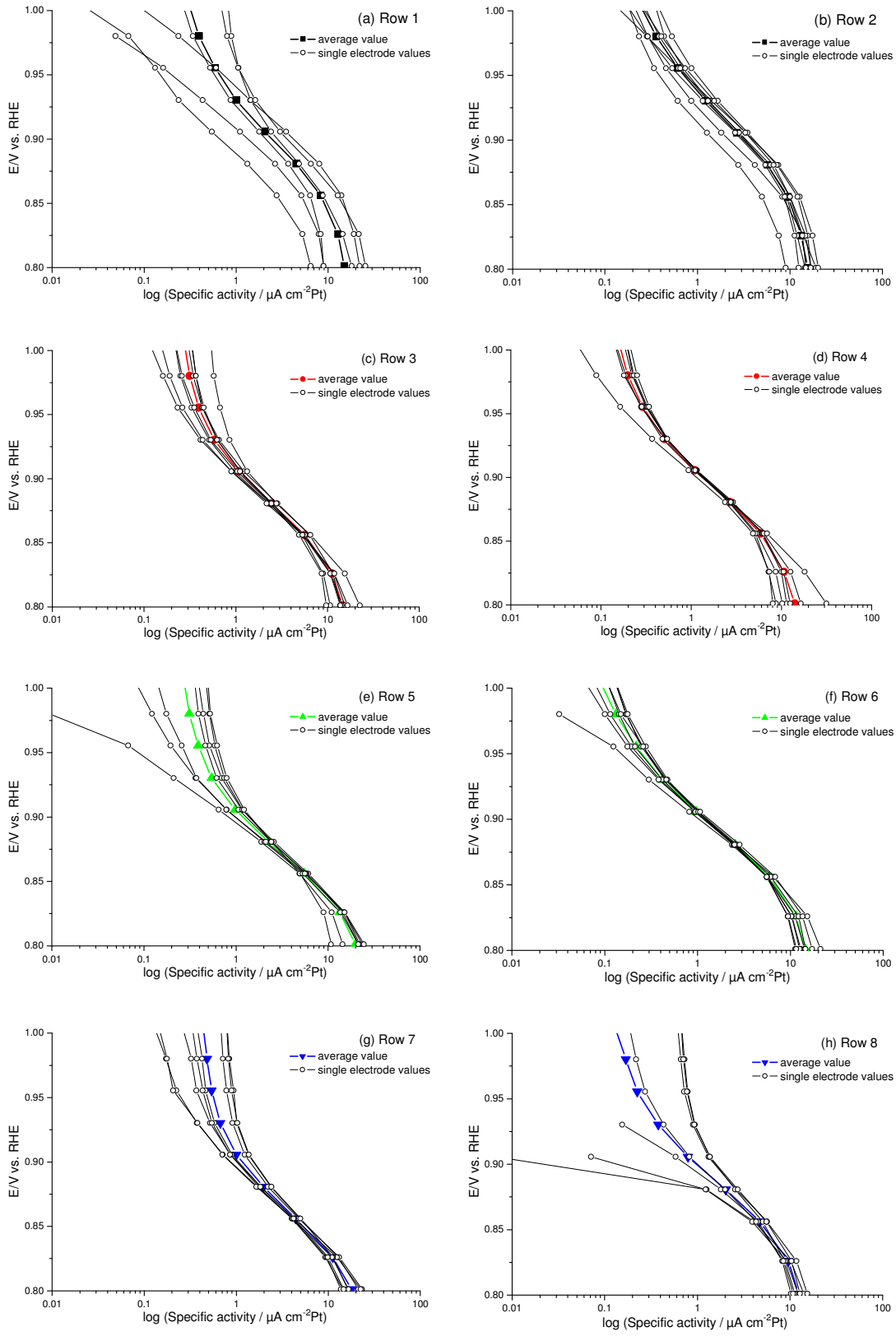

Figure 12 Tafel plots for ORR experiment testing 20 wt. % Pt/C. Different method of ink preparation present the volume of water (mL) apply to disperse 10 mg of catalyst and volume of ink (µL) disposed onto electrode (a) 1 mL, 10 µL (b) 1 mL, 20 µL (c) 3 mL, 10 µL (d) 3 mL, 20 µL (e) 5 mL, 10 µL (f) 5 mL, 20 µL (g) 7 mL, 10 µL (h) 7 mL, 20 µL

4 Results and Discussion

4.1 Qualitative agreement - Particle size effect on PtCo/C

The array cell was used to rank the ORR activities of a series of PtCo/C catalysts [33]. The results obtained were compared to the activities obtained using a 50 cm^2 fuel cell at Johnson Matthey Technology Centre by Dr Sarah Ball. The main aim of this study was to establish the level of qualitative agreement and reproducibility of the measurements performed using a new 64 channel array system compared to the previous results. Details of the catalysts studied are presented in Table 2.

Table 2 Details of the PtCo/C catalysts investigated.

No.	Catalyst code	Composition	XRD - Crystal Size (nm)	XRD - Lattice Parameter (Å)
(a)	-----	20 wt% Pt / C	-----	-----
(b)	05/76	40 wt% Pt (Pt:Co 3:1) / C	3.6	3.85
(c)	04/118	40 wt% Pt (Pt:Co 3:1) / C	3.7	3.85
(d)	04/111	40 wt% Pt (Pt:Co 3:1) / C	5.9	3.85
(e)	04/132	40 wt% Pt (Pt:Co 3:1) / C	12.6	3.85

4.1.1 Cyclic voltammetry

Cyclic voltammograms for each of the catalysts obtained using the new 64 channel array and 0.5 H_2SO_4 mol dm^{-3} are shown in Figure 13. The CVs are reported as obtained (A) and after correction for the real Pt surface area (B), which was obtained using the CO stripping area as described in Chapter 2 section 3.2. The real surface areas are illustrated in Figure 14 to show the variation caused by the method. However, as illustrated in Figure 13B, the normalisation accents for all this variation and the normalised CVs are all on the same scale.

As seen in Figure 13A, the catalysts (b) 05/76 and (c) 04/118 showed similarities, and the magnitude of the raw currents are almost identical. It is important to note that the hydride region, double layer region and CO stripping peak shape look similar. In conclusion, increasing the particle size from 3.6 nm to 3.7 nm does not change the magnitude of currents much. On the other hand, if the particle diameter increases significantly to 5.9 nm, as for catalyst (d) 04/111, the magnitude of current decreases rapidly. If the Pt particles are larger, proportionally less of the Pt atoms are available at the surface for the catalytic ORR reaction. Thus, the disadvantage of larger particles is that the ORR mass activity is lower for larger

particles. However, this is balanced by the advantage that the active sites are more well organised at the surface and hence the ORR specific activity is greater for larger particles.

Figure 13 B is a demonstration of the same results as in Figure 13 A. In this case, the currents were normalised by Pt real surface area obtained in CO stripping experiment and converted into specific activity. From this graph, it can be seen that the magnitudes of currents are similar. The essential peak features are different between the catalysts. For example, hydride adsorption and desorption peak together with hydrogen evolution peaks do not look similar. The hydride region for catalysts (b) and (c) are almost identical, and peaks responsible for hydrogen evolution almost do not appear in hydride region of cyclic voltammogram. As the particle size for (d) 04/111 catalyst increases, the shapes of the hydrogen evolution peaks alter and are of much greater currents. The largest hydrogen evolution peaks appear for (e) 04/132 catalyst with particle size 12.6 nm. Hydrogen evolution was visible in the voltammograms between 0.05 and 0.1 V, the extent of which was related to the size of the Pt particles; more hydrogen evolution being observed for larger particles and the onset of hydrogen evolution being negative of 0.05 V for the smallest particles. In conclusion, as particle size increased hydrogen evolution moved toward more positive potentials. Another interesting feature is the second CO stripping peak, which appeared at around 0.6 V. A very small peak was observed in the CV acquired for (d) 04/111 catalyst. At the same potential, the CV collected for the 04/132 sample showed a much greater peak. This could be connected with the much more organized structure of the Pt centres. Crystallographic sites arise at larger Pt centres that do not exist at smaller particles.

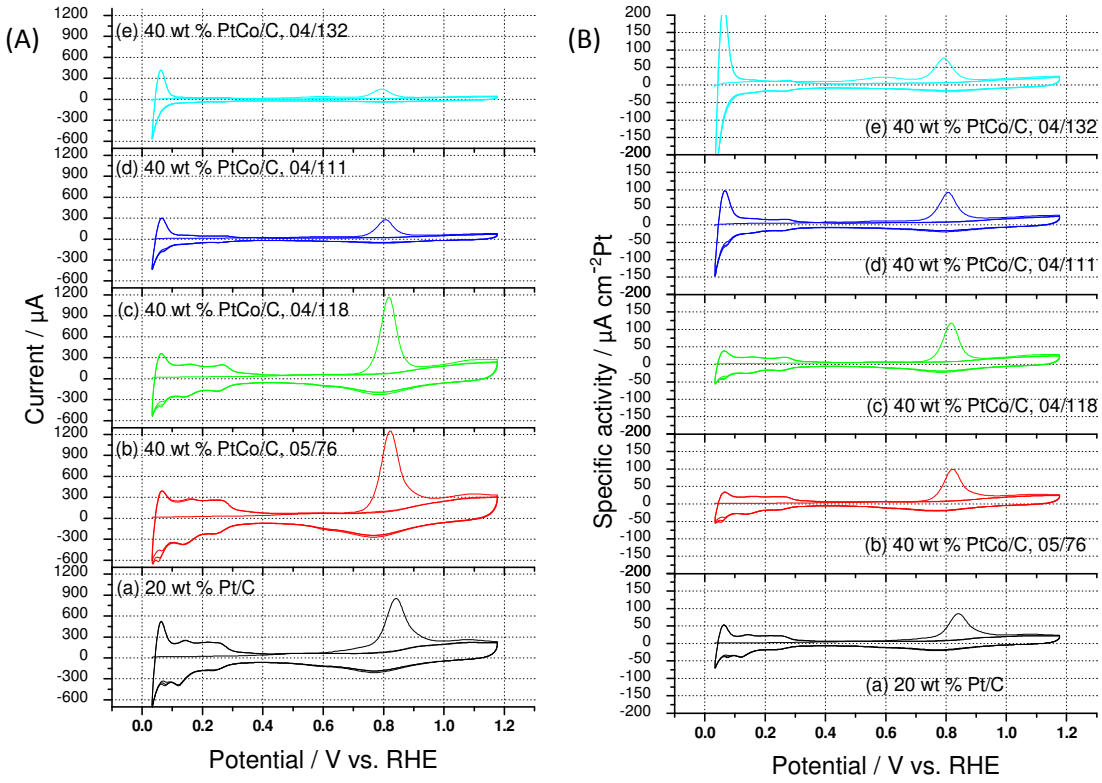

Figure 13 CO stripping voltammograms showing average results obtained for catalysts described in Table 2 (A) raw data – currents without normalisation (B) normalized currents - specific activity (mA cm^{-2}_{Pt}).

Pt real surface area was used to normalise cyclic voltammograms acquired during both experiments. This area was calculated using CO stripping peak charge. Shows in Figure 14 a comparison of Pt real surface area for each of the catalysts measured obtained in two replicate experiments. As can be seen, the difference was not large between the two experiments, except for the electrode with 20 wt. % Pt/C. The results were similar to each other and placed in a range of error bars. As a result, a clear trend could be established for group of 40 wt. % Pt/C catalyst. The Pt real surface area decreased in an order (b) 3.6 > (c) 3.7 >> (d) 5.9 > (e) 12.6 nm particle size diameter. The data for the electrode with 20 wt. % Pt/C was excluded from this trend due to the enormous difference in its Pt real surface obtained during both replicate experiments.

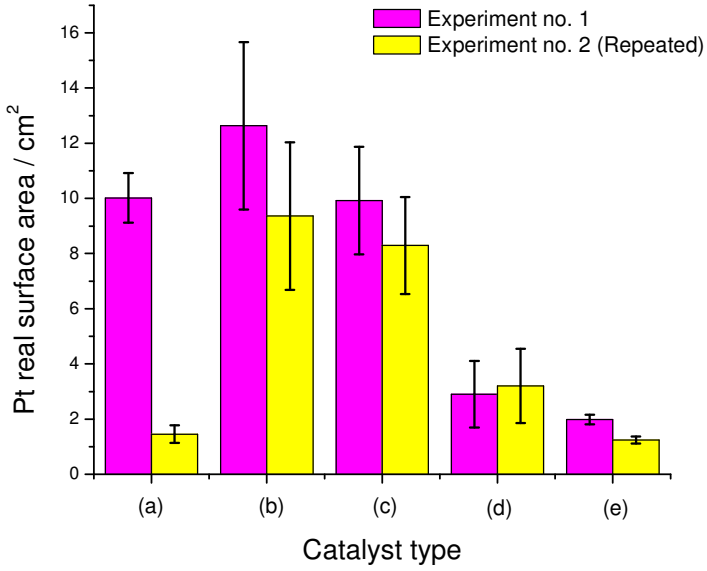

Figure 14 Comparison of Pt real surface area obtained in two replicate experiments calculated from CO stripping peak charge.A series of PtCo/C along with Pt/C catalyst described in Table 2 was investigated.

Figure 15 is an illustration of the CO stripping onset potentials extracted from CVs (Figure 13) obtained for both replicate experiments. In this case, the problem occurred again with 20 wt. % Pt/C catalyst. The difference of current onset potentials for this sample was enormous. For this reason, the catalyst was excluded from the analysis. The tendency to shift onset of the peak toward lower potentials was observed for a series of 40 wt. % Pt/C catalysts as follows (b) 3.6 > (c) 3.7 > (d) 5.9 > (e) 12.6 nm particle size diameter.

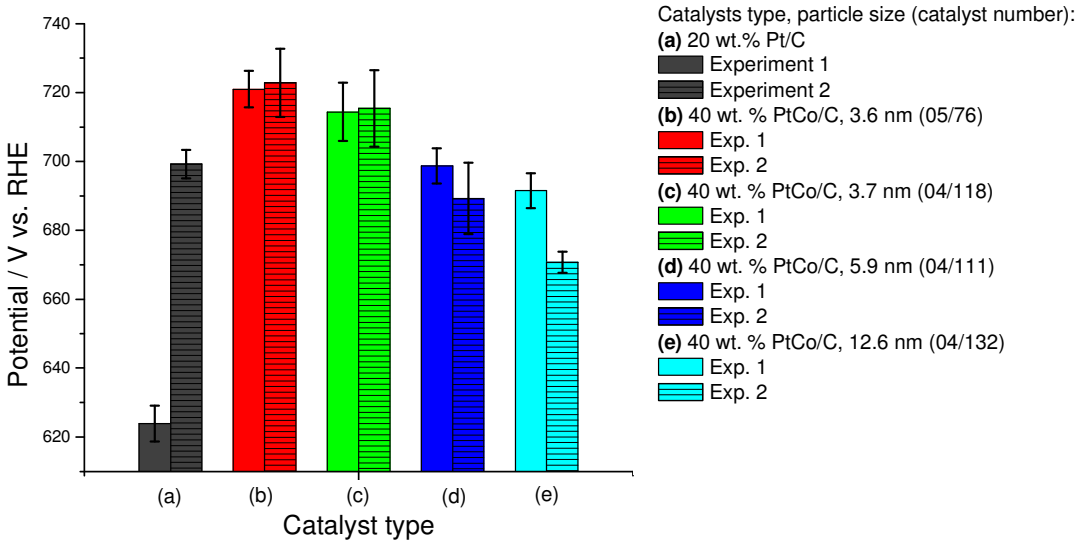

Figure 15 Comparison of average CO stripping peak onset potentials (mV) display with associated standard deviation. The values were extracted from CO stripping voltammograms acquired for catalysts described in Table 2. Two replicates were completed for the experiment.

The maximum of CO stripping peak potential shifted in the opposite direction, in contrast to the trend obtained for onset potential. In theory, cyclic voltammograms acquired at the same scan rate should have the same maximum peak potential; the potential of the peak is independent of Pt loading. This applies to the electrode with 20 wt. % Pt/C catalyst, which revealed a huge difference in Pt loading between two replicable experiments, but the peak potential remained the same. The maximum of CO stripping peak shifted towards lower potential values in order (a) > (b) > (c) > (d) > (e) and established a clear trend. The values obtained for replicate experiments are in perfect agreement for all the catalysts.

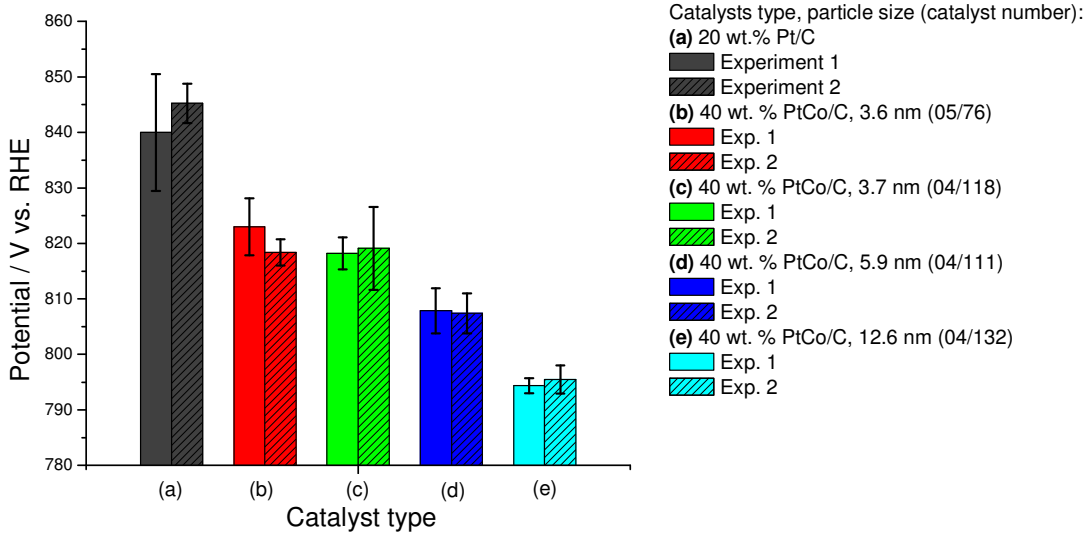

Figure 16 Comparison of average CO stripping maximum current peak potential (mV).

The comparison of maximum oxide reduction peak positions is shown in Figure 17. It can be seen that the results agreed between the replicate experiments and remained within the error of the measurements. The only dissimilarity occurred for (b) 05/76 catalyst. The oxide maximum peak position extracted from cyclic voltammograms form a clear trend. The highest potential on the scale is for catalyst (e) with the largest particle diameter of 12.6 nm. When particle size decreased gradually the position of the oxide peak shifted toward lower potentials as ordered by (e) > (d) > (c) > (b) > (a).

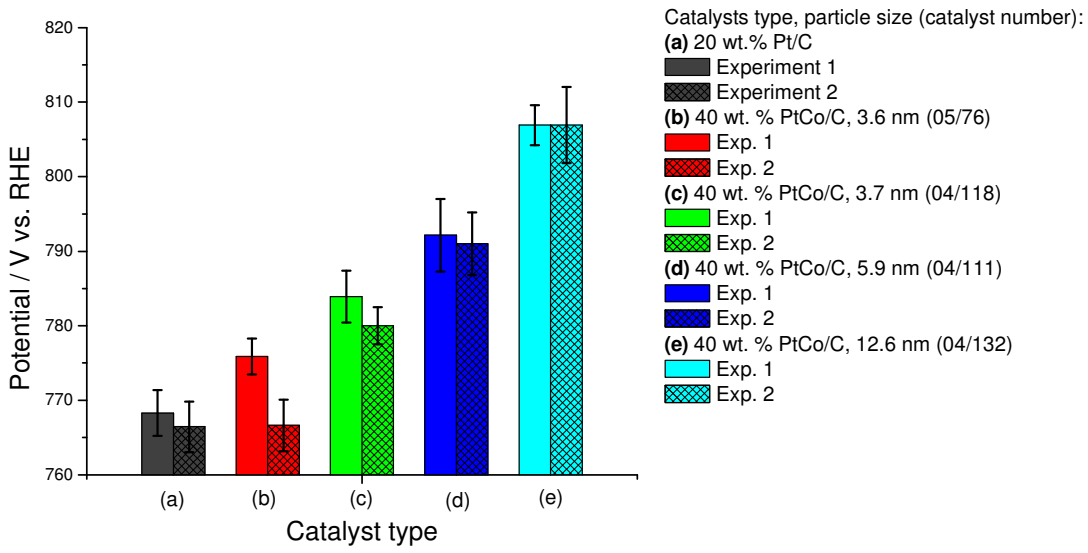

Figure 17 Comparison of average oxide reduction maximum current peak potential.

In conclusion, the clear trends in the rankings were established for maximum of CO stripping and oxide peak positions. Other factors such as Pt real surface area measured using two methods and CO stripping onset peak position were clear for a series of 40 wt. % Pt/C catalysts. Unfortunately, the 20 wt. % Pt/C catalyst was excluded from the trend due to a problem which occurred in preparation of the electrodes.

4.1.2 ORR

The second part of the investigation was the ORR experiment. The tests were carried out using the same procedure as described in section 3.2. Two replicate experiments were run with the aim of proving the reproducibility of the measurements. Initially, the polarisation curves were plotted as presented in Figure 18A. Due to sluggish kinetic processes in the ORR, most scientists concentrate on the kinetic region of the polarisation curve. In this case the region was positioned between 0.88 V and 1 V potential limits. All the catalysts of the same type presented similar and reproducible specific activities in this range. The problems occurred with only one catalyst, 20 wt. % Pt/C, which was similarly illustrated and depicted in the CV experiment in the previous section. Both the kinetic and mass transport regions could be observed in the full polarisation curve (Figure 18). The mass transport region appeared at potentials below 0.88 V and data in this region were not reproducible. However, data in the kinetic region were reproducible and could be used to rank the catalysts. An illustration of the typical results is shown in Figure 18 for catalyst (e) 04/132 with 12.6 nm particle diameter (Figure 18A). The Tafel plot of the data in Figure 18A is shown in

Figure 18B. In theory a straight line of the Tafel plot region corresponds to the kinetic region, as described in detail in Chapter 2 section 3.3

(A)

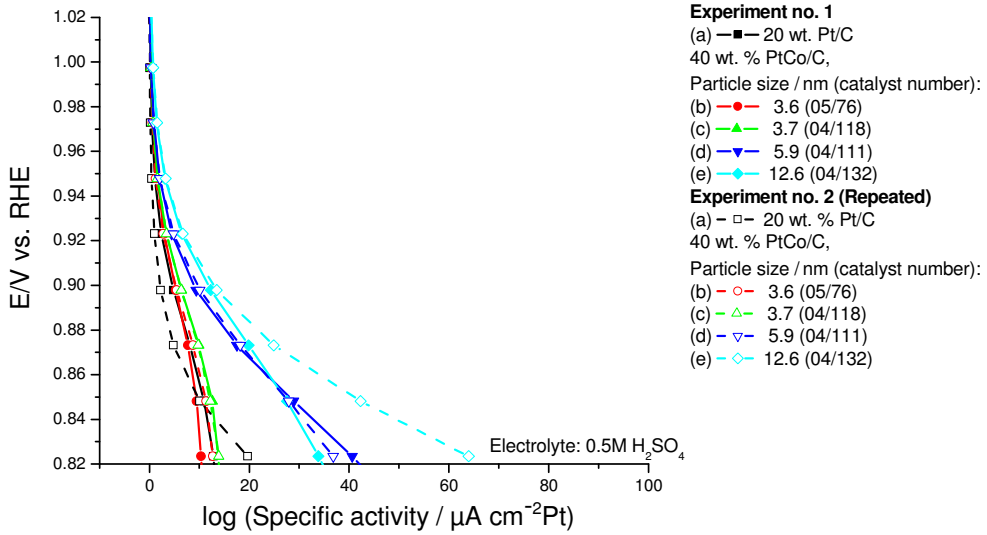

(B)

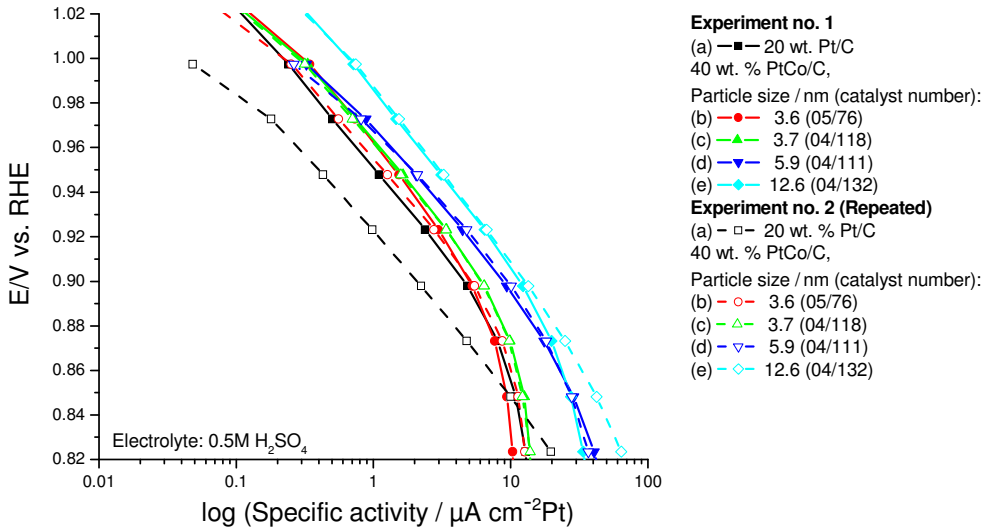

Figure 18 Two replicates experiments carried out using the new 64 channel array cell with 5 mm diameter vitreous carbon working electrodes. The currents were normalized per unit of Pt active surface area determined from the CO stripping peak area and then averaged over all the electrodes of the same type. Both experiments were run using the same catalysts. All 40 wt % PtCo/C catalysts have different particle diameter. Figure (A) polarisation curves - specific activity on the x-scale and (B) Tafel plots – logarithm 10 of specific activity on the x-scale.

Excellent reproducibility was obtained for all the catalysts tested with exception of 20 wt. % Pt/C catalyst. The best ORR electrocatalytic properties were obtained with demonstrate catalyst (e) 04/132 with 12.8 nm particle diameter. As expected the catalysts with similar particle diameters of (b) 05/76, 3.6 nm and (c) 04/118, 3.7 nm produced very similar results. Slightly better catalytic properties were displayed by catalyst (d) 04/111 with

particle diameter of 5.9 nm. In summary, the particle size effect for 40 wt. % PtCo/C catalysts set is clear and forms a trend. The specific activity increased as particle size increased (high specific activity>12.8>5.9>3.7>3.6>low specific activity). Similar results were reported in previous studies [34-37].

4.2 Acid leached samples

In order to prove the accuracy and quality of the new 64 channel array, experiments with the catalysts of the same Pt content and identical structure parameters were carried out. The catalysts described in Table 3 were used to run replicate experiments. The set contained standard 20 wt. % Pt/C and three 40 wt. % PtCo/C catalysts. All PtCo/C catalysts were similarly prepared e.g. fired with hydrogen gas at 1000 °C. The preparation method vary only in one variation. This means that each catalyst was leached [37-39] with a different acid or without using acid (H_2SO_4, $HClO_4$, no acid) in the preparation method. The acid leaching were carried out at Johnson Matthey Technology Centre (Sonning Common). XRD results revealed that leaching of the catalysts did not modify the structure. Hence, the particle crystal size (5.8 nm) and lattice parameter (3.85 Å) were identical for all the samples.

Considering the structure and composition for each 40 wt. % PtCo/C catalyst, the data collected should not display much diversity. The only exception was 20 wt. % Pt/C, which was likely to demonstrate lower performance.

Table 3 Catalysts used in both replicate experiments.

No.	Catalyst code	Composition	Acid leached	XRD - Crystal Size (nm)	XRD - Lattice Parameter (Å)
(a)	-----	20 wt. % (Pt) / C	-----	-----	-----
(b)	04/111	40 wt% Pt (Pt:Co 3:1) / C	no	5.9	3.85
(c)	05/19	40 wt% Pt (Pt:Co 3:1) / C	H_2SO_4	5.9	3.85
(d)	05/66	40 wt% Pt (Pt:Co 3:1) / C	$HClO_4$	5.9	3.85

Figure 19 presents CO stripping voltammograms as a first scan together with the following second scan. Similarly to the previous section, in this set of catalysts the maximum of CO stripping peak also shifted. Both catalysts (c) 05/19 and (d) 05/66 leached with acids had the same value of 848 mV, while catalyst without acid leaching (b) 04/111 had a maximum at 828 mV. The current peak for the 20 wt. % Pt/C sample occurred at 845 mV (RHE).

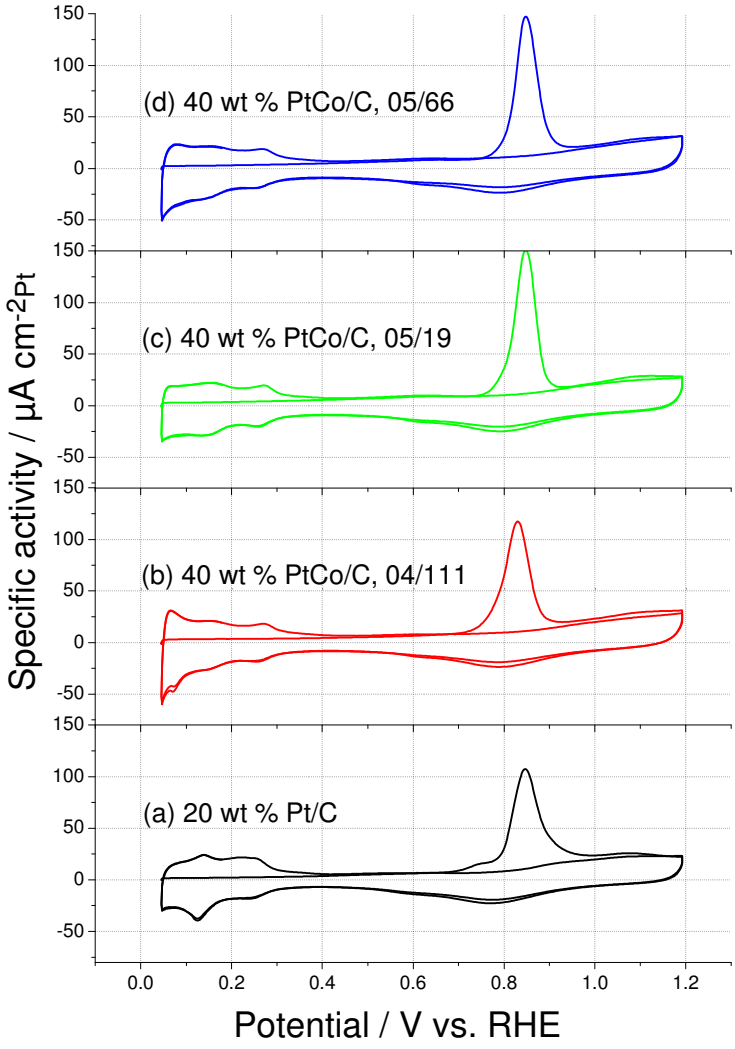

Figure 19 CO stripping voltammograms obtained for set of catalysts described in Table 3.

The new 64 channel array results showed a small but very accurate difference between Tafel plots for each catalyst (Figure 20). The performances of the catalysts were in the order (d)>(b)≥(c)>>(a), with (b) being slightly more active than (c).

The results were repeated in the second replicate experiment, The best performance was achieved for catalyst (d) 05/66 leached with perchloric acid. The second best performer was catalyst (b) 04/111 without acid leaching, and the third sample displaying the third performance was (c) 05/19 leached with sulphuric acid. Unquestionably, the lowest performance appears again for (a) 20 wt. % Pt/C catalyst, which was measured here for comparison similarly as in every set tested.

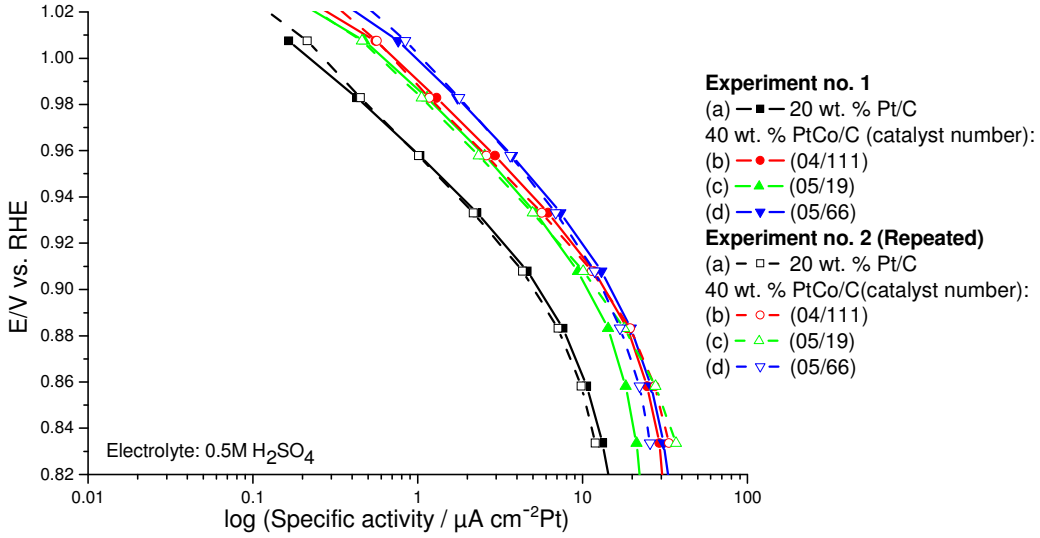

Figure 20 Tafel plots - Comparison of the series of 40 wt. % PtCo/C catalysts along with 20 wt. % Pt/C (Table 3). The experiment carried out in two replicates. Different acids was used to leach catalysts ($HClO_4$, H_2SO_4 and without any). The currents for each separate electrode were normalized per unit of Pt active surface area determined from the CO stripping peak area.

4.3 Binary catalyst composition effect

The effects of binary alloy composition were explored by examining a series of PtCo catalysts with various Pt:Co ratios [35-37, 39, 40] as shown in Table 4. All the other preparation parameters such as firing in hydrogen gas at a temperature of 1000 °C stayed unchanged for 40 wt. % Pt/C catalysts. It is clearly seen that the particle diameter (nm) and lattice parameter (Å) changed as the ratio was modified.

Table 4 A set of catalysts used in experiments testing surface composition dissimilarity.

No.	Catalyst code	Composition	XRD - Crystal Size (nm)	XRD - Lattice Parameter (Å)
(a)	-----	20 wt. % (Pt) / XC72R		
(b)	04/111	40 wt% Pt (Pt:Co 3:1) / Ketjen	5.9	3.85
(c)	05/74	40 wt% Pt (Pt:Co 87.5 % Pt/12 % Co) / Ketjen	7.2	3.88
(d)	05/99	40 wt% Pt (Pt:Co 50 % Pt/50 % Co) / Ketjen	6.6	tetragonal

Figure 21 is an illustration of CO stripping voltammograms as a first scan together with a second following scan. The CO stripping peak for each catalyst possesses a different shape and position. As can be seen, the most significant shift of the current peak towards more positive potential occurred for 20 wt. % Pt/C and was 836 mV. The current peaks of 40 wt. % Pt/C catalysts occurred at similar potentials. Sample (b) 04/111 had a value of 795 mV, and the next catalyst in the trend was (d) 05/99 with maximum at 800 mV. It is

interesting that hydrogen evolution peaks for catalyst with larger particle size appeared at higher potentials than for samples with lower particle diameter. It can be seen that peak magnitude decreased in the order (c) 7.2 > (d) 6.6 > (b) 5.9 nm > (a). Particle size influence on the hydrogen evolution reaction was similarly described in section 4.1.1.

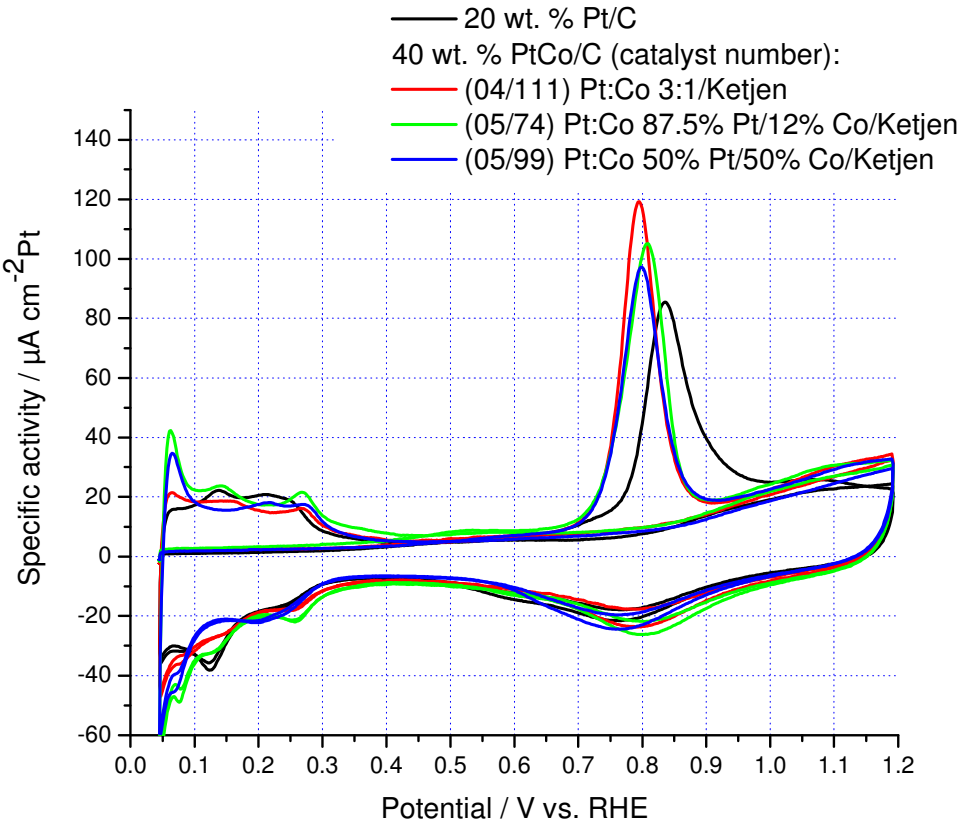

Figure 21 Comparison of average CO stripping voltammograms obtained for catalysts described in Table 4.

The properties of ORR activity were determined by plotting Tafel plots as shown in Figure 22, showing results for two replicate experiments. The curves of the same catalysts do not superimpose perfectly. However, trends can still be distinguished. The ranking of the ORR activity is (c)>(b)≈(d)>>(a), with (b) being a little better than (d) catalyst. In conclusion, as the Pt:Co ratio was modified towards higher Pt percentage content, then the ORR activity was higher.

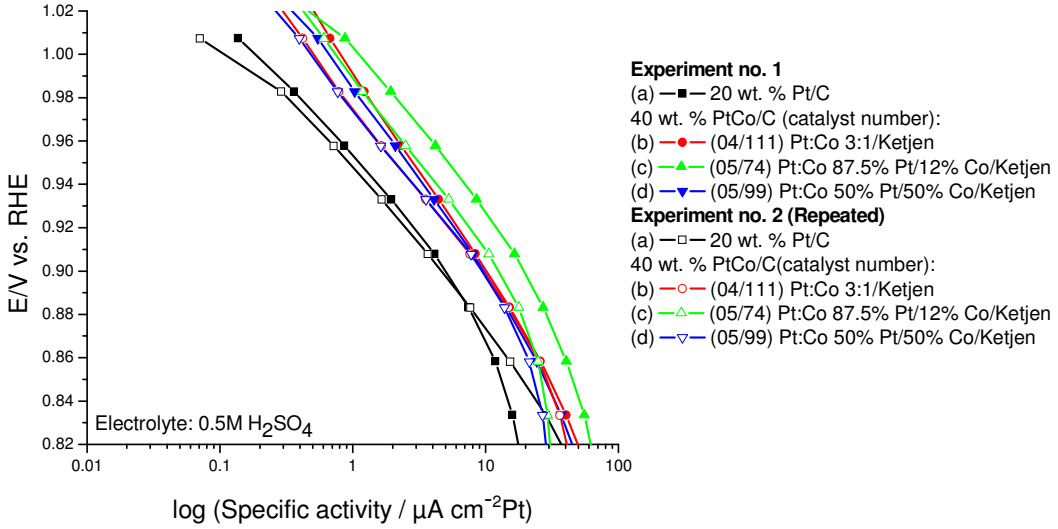

Figure 22 Comparison of Tafel plots obtained for catalyst described in Table 4. Data calculated from two separate experiments carried out as described in section 3.2.

5 Conclusions and Future Directions – Recommendations

In conclusion, the enhanced cell design helped to acquire better quality data. The results described above showed good reproducibility of the new apparatus. The trends were consistent and agreed with results obtained using the RDE method (Chapter 3). However, data quality still needed to be improved. In order to apply the cell as a reliable general measuring technique, many details still need to be improved. One of the recurring problems was the sealing of the cell, especially where vitreous carbon working electrodes adhere to the bottom PTFE plate. Enhancements could be made by changing the orientation of the electrodes, which can be positioned upside down, embedded into a top plate, having spring loaded pin contacts from the top. In this case, the acid would not penetrate upwards against the force of gravity.

A second factor obstructing high quality data acquisition was the ink preparation and the electrode preparation. The work of testing different solvents as catalyst dispersive media needs to be carried out. A range of solvents with different surface tension, which allow a uniform deposition of the catalyst layer onto the electrode surface, should be explored in order to obtain more reproducible data. A third interesting enhancement could be the application of elevated temperature to the new system. The actual fuel cell operational temperature is around 80 °C. For this reason, the application of a higher temperature in the cell environment should help to collect data that are more comparable to data acquired in real conditions. Another problem to solve is the method of data processing. At the moment, calculation and graph plotting are completed manually by using up to four different

software. To improve the simplicity of data processing new software needs to be written. The program should include features to automate the transformation of simple but time-consuming calculations. Moreover, the application of the new purging tube system should, at least to some extent, control and stabilize mass transfer in the solution. More details will be described in Chapter 6, which summarises and compares the similarities and differences between the three systems, RDE, 64 channel array, and Array Fuel Cell.

6 References

1. A. W. Czarnik and S. H. DeWitt, A Practical Guide to Combinatorial Chemistry, Oxford University Press, 1998.
2. S. J. Pollack, J. W. Jacobs, and P. G. Schultz, Science 234:1570 (1986).
3. T. A. Dickinson, D. R. Walt, J. White, and J. S. Kauer, Analytical Chemistry 69:3413 (1997).
4. D. Pei, H. D. Ulrich, and P. G. Schultz, Science 253:1408 (1991).
5. C. J. Ziegler, A. P. Silverman, and S. J. Lippard, Journal of Biological Inorganic Chemistry 5:774 (2000).
6. X. D. Xiang, X. D. Sun, G. Briceno, Y. L. Lou, K. A. Wang, H. Y. Chang, W. G. Wallacefreedman, S. W. Chen, and P. G. Schultz, Science 268:1738 (1995).
7. R. S. Glass, S. P. Perone, and D. R. Ciarlo, Analytical Chemistry 62:1914 (1990).
8. E. Reddington, A. Sapienza, B. Gurau, R. Viswanathan, S. Sarangapani, E. S. Smotkin, and T. E. Mallouk, Science 280:1735 (1998).
9. G. Y. Chen, D. A. Delafuente, S. Sarangapani, and T. E. Mallouk, Catalysis Today 67:341 (2001).
10. N. D. Morris and T. E. Mallouk, Journal of the American Chemical Society 124:11114 (2002).
11. Y. P. Sun, H. Buck, and T. E. Mallouk, Analytical Chemistry 73:1599 (2001).
12. Z. Fei and J. L. Hudson, Journal of Physical Chemistry B 101:10356 (1997).
13. Z. Fei, R. G. Kelly, and J. L. Hudson, Journal of Physical Chemistry 100:18986 (1996).
14. M. G. Sullivan, H. Utomo, P. J. Fagan, and M. D. Ward, Analytical Chemistry 71:4369 (1999).
15. J. S. Cooper, G. H. Zhang, and P. J. McGinn, Review of Scientific Instruments 76 (2005).
16. S. Guerin, B. E. Hayden, C. E. Lee, C. Mormiche, J. R. Owen, A. E. Russell, B. Theobald, and D. Thompsett, Journal of Combinatorial Chemistry 6:149 (2004).
17. A. D. Spong, G. Vitins, S. Guerin, B. E. Hayden, A. E. Russell, and J. R. Owen, Journal of Power Sources 119:778 (2003).
18. P. Strasser, Q. Fan, M. Devenney, W. H. Weinberg, P. Liu, and J. K. Norskov, Journal of Physical Chemistry B 107:11013 (2003).
19. E. S. Smotkin, J. H. Jiang, A. Nayar, and R. X. Liu, Applied Surface Science 252:2573 (2006).
20. R. Liu and E. S. Smotkin, Journal of Electroanalytical Chemistry 535:49 (2002).

21. B. C. Chan, R. X. Liu, K. Jambunathan, H. Zhang, G. Y. Chen, T. E. Mallouk, and E. S. Smotkin, Journal of the Electrochemical Society 152:A594 (2005).
22. R. R. Diaz-Morales, R. X. Liu, E. Fachini, G. Y. Chen, C. U. Segre, A. Martinez, C. Cabrera, and E. S. Smotkin, Journal of the Electrochemical Society 151:A1314 (2004).
23. E. S. Smotkin and R. R. Diaz-Morales, Annual Review of Materials Research 33:557 (2003).
24. S. Guerin, B. E. Hayden, C. E. Lee, C. Mormiche, and A. E. Russell, Journal of Physical Chemistry B 110:14355 (2006).
25. A. Hagemeyer, P. Strasser, and A. F. Volpe, High-Throughput Screening in Chemical Catalysis WILEY-VCH Verlag GmbH & Co. KGaA, 2004.
26. B. Gurau, R. Viswanathan, R. X. Liu, T. J. Lafrenz, K. L. Ley, E. S. Smotkin, E. Reddington, A. Sapienza, B. C. Chan, T. E. Mallouk, and S. Sarangapani, Journal of Physical Chemistry B 102:9997 (1998).
27. X.-D. Xiang, Applied Surface Science 223:54 (2004).
28. S. Miertus, G. Fassina, and P. F. Seneci, Chemicke Listy 94:1104 (2000).
29. U. Koponen, H. Kumpulainen, M. Bergelin, J. Keskinen, T. Peltonen, M. Valkiainen, and M. Wasberg, Journal of Power Sources 118:325 (2003).
30. K. Kinoshita, Journal of the Electrochemical Society 137:845 (1990).
31. H. A. Gasteiger, S. S. Kocha, B. Sompalli, and F. T. Wagner, Applied Catalysis B-Environmental 56:9 (2005).
32. U. A. Paulus, T. J. Schmidt, H. A. Gasteiger, and R. J. Behm, Journal of Electroanalytical Chemistry 495:134 (2001).
33. B. C. Beard and P. N. Ross, Journal of the Electrochemical Society 137:3368 (1990).
34. J. N. Soderberg, A. H. C. Sirk, S. A. Campbell, and V. I. Birss, Journal of the Electrochemical Society 152:A2017 (2005).
35. E. Antolini, J. R. C. Salgado, M. J. Giz, and E. R. Gonzalez, International Journal of Hydrogen Energy 30:1213 (2005).
36. U. A. Paulus, A. Wokaun, G. G. Scherer, T. J. Schmidt, V. Stamenkovic, V. Radmilovic, N. M. Markovic, and P. N. Ross, Journal of Physical Chemistry B 106:4181 (2002).
37. U. A. Paulus, A. Wokaun, G. G. Scherer, T. J. Schmidt, V. Stamenkovic, N. M. Markovic, and P. N. Ross, Electrochimica Acta 47:3787 (2002).
38. M. Teliska, V. S. Murthi, S. Mukerjee, and D. E. Ramaker, Journal of the Electrochemical Society 152:A2159 (2005).

39. V. Stamenkovic, T. J. Schmidt, P. N. Ross, and N. M. Markovic, Journal of Physical Chemistry B 106:11970 (2002).

40. P. Hernandez-Fernandez, S. Rojas, P. Ocon, J. L. G. de la Fuente, P. Terreros, M. A. Pena, and J. L. Garcia-Fierro, Applied Catalysis B: Environmental 77:19 (2007).

Contents

Chapter Five: Array Fuel Cell (AFC)

1 Introduction

The next stage in developing a screening method for testing fuel cell catalysts was to move to testing the catalysts in a fuel cell environment, i.e. as membrane electrode assemblies (MEA) and with the fuel and air supplied from the gas phase. To this end, a 25 electrode parallel array cell has been developed, based on the design reported by, and in collaboration with, Smotkin [1-4]. The original cell was designed for methanol oxidation studies and modifications were necessary for PEM FC studies. The primary difference between Smotkin's original design and that reported in this chapter is that a parallel flow field was used for the working electrodes rather then the serpentine flow field used in the original.

In this chapter the design of the array cell and key experimental parameters and protocols will be described. The cell was then used to screen several sets of catalysts as previously described in Chapter 3 (Rotating Disc Electrode) and 4 (64 channel array).

1.1 System components

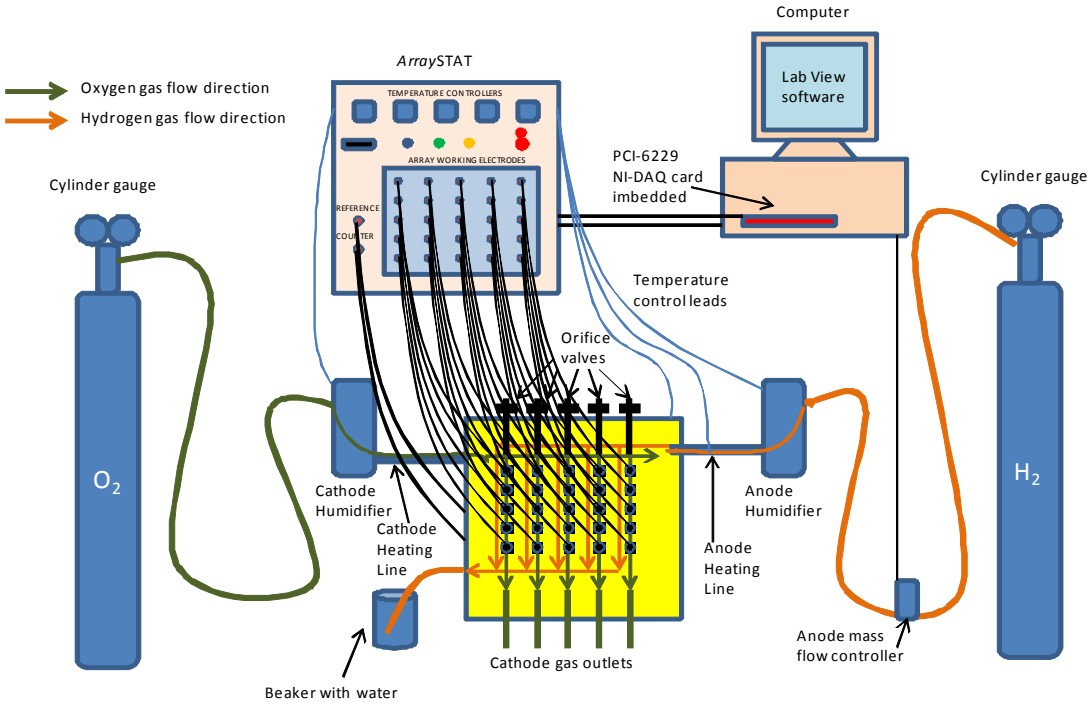

Figure 1 Schematic of the 25 channel array system

A schematic diagram of the array fuel cell system is shown in Figure 1. The system is made of a 25 channel parallel flow field fuel cell, two humidifiers, a high power potentiostat (Arraystat) designed and manufactured at NuVant Systems Inc., acquisition card embedded into a PC, and gas cylinders (hydrogen, oxygen, nitrogen and carbon monoxide). The gases

were passed through humidifiers before reaching the MEA cell. Temperature controllers and electrode connections were plugged into the potentiostat. LabView software was used to control the PCI-6229 acquisition card, which regulated the Arraystat. In addition, 8 mass flow controllers could be controlled with the software. Each of the array electrodes could be controlled separately using a current follower embedded into the potentiostat. Each of these components is described in more detail below.

1.1.1 Array Fuel Cell

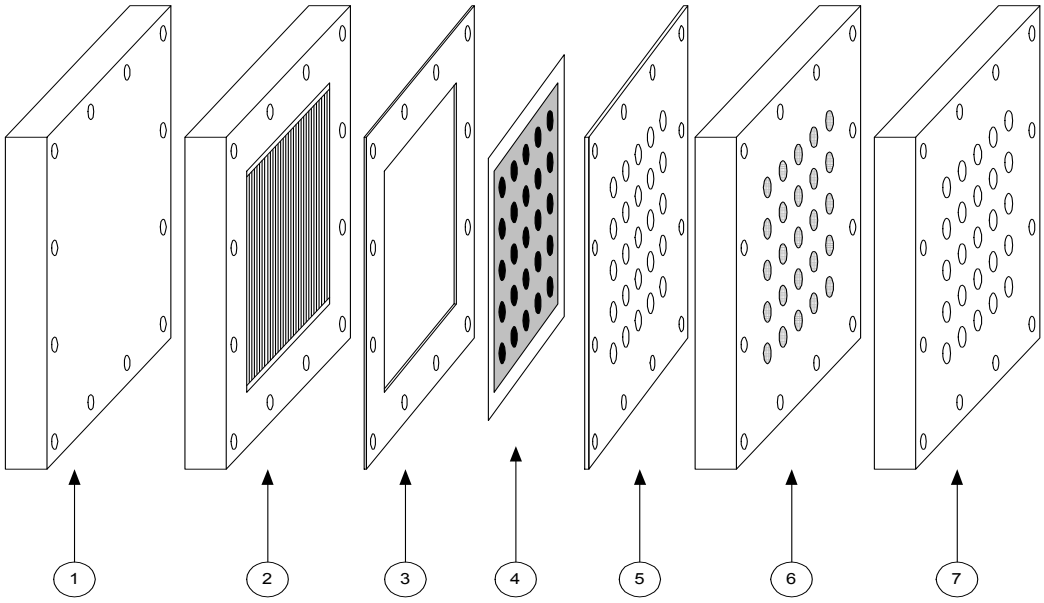

Figure 2 Exploded schematic of array fuel cell assembly 1. Counter-side end plate; 2. Graphite counter flow field block; 3. Gasket on the counter electrode for gas sealing; 4. Membrane Electrode Assembly (MEA); 5. Gasket on array electrode for sealing; 6. Sensor array block; 7. Sensor-side end plate [2]

The array cell is shown schematically in Figure 2 and photographs are shown in Figure 3. The cell consists of components as indicated in Figure 2. The MEA (described in greater detail in section 1.1.2) is placed in the centre of the cell (4). On the working electrode side the components are a reinforced Teflon gasket on an array electrode for sealing purposes (5), a sensor array block made of isolation-reinforced resin plastic (garolite) with 25 graphite sensor electrodes (6), and a stainless steel sensor-side end plate (7). On the counter electrode side the components are a reinforced Teflon gasket (3), the counter electrode flow field plate/counter collector (2) and a stainless end plate (1). In addition, the array cell has holes to insert thermocouples and heater cartridges. 25 contact leads individually connect the working electrode sensors to the Arraystat.

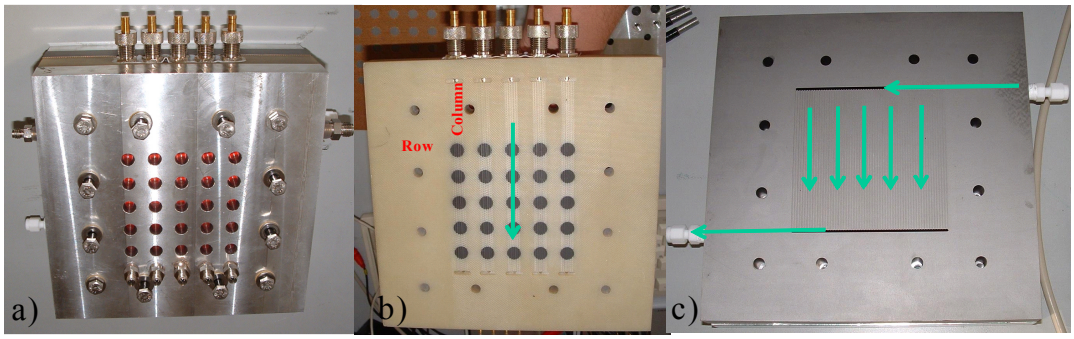

Figure 3 Array cell: a) full assembly – top view; b) working electrode plate with 25 graphite sensors positioned in five flow fields; c) counter/reference flow field plate. Green arrows denote gas flow direction.

As shown in Figure 3 the sensor block for the working electrode side also serves as the flow field, supplying gases to the 25 working electrodes. The supply consists of 5 parallel flow paths, one down each column of electrodes. These are fed by one gas inlet which then feeds 5 high precision orifice valves that are manually adjusted to provide the designed flow rates of gases to the electrodes. The 5 flow fields terminate at five separate outlet paths at the bottom of the cell.

On the counter electrode side (panel C of Figure 3), the flow field/current collector is made from a graphite block. Gas flow fields were machined into this block and consist of a single inlet path at the top of the cell, which is then split into parallel feed paths (0.74 mm wide and 0.74 mm deep) that terminate in a single outlet path at the bottom of the cell.

1.1.2 MEA

The membrane electrode assembly (MEA)[8] is made of a common counter/reference electrode, Nafion 117® membrane and 25 working electrodes [1] (Figure 4). The counter electrode was 103 cm^2 and 0.19 mm thick and was a Pt catalyst supported on carbon mixed with Nafion® polymer [11] deposited on a gas diffusion layer (Toray paper) to yield 0.4 $mg_{Pt}\,cm^{-2}$. The catalyst side of the electrode is facing the Nafion 117® membrane [12-15] (0.18 mm thickness). 25 disc electrodes (0.713 cm^2) were hot pressed on the side opposite to the counter electrode. The working electrodes' discs have the same thickness as the counter electrode. Specific details of the compositions of the working electrodes will be given as required later in this chapter.

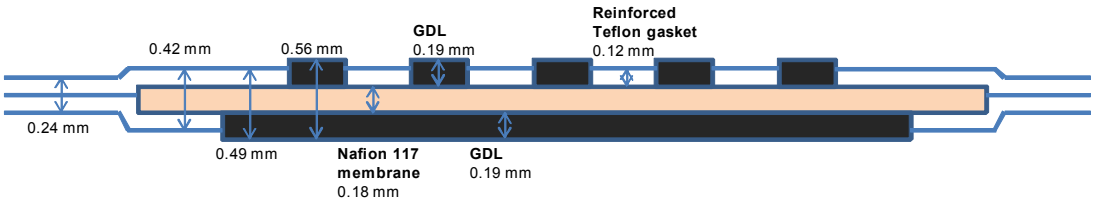

Figure 4 A schematic of cross section of the MEA including gaskets used in array fuel cell assembly.

1.1.3 Humidifiers

The gases were heated and humidified prior to entering the fuel cell by purging through purified water at elevated temperature. Each humidifier had 500 cm^3 volume. The temperature was controlled by a thermocouple positioned in the gas phase as an alternative to placing it in the liquid phase inside the humidifier.

1.1.4 Arraystat

The Arraystat was designed for simultaneous evaluation of 25 polarisation curves. The control system allowed simultaneous and individual independent acquisition of the data from electrodes on the array.

The potentiostat has 25 channel inputs; each can be controlled separately with the software and acquisition card. The potentiostat can control the potential over the range ± 10 Volts with resolution 3 mV. However, the potentiostat cannot exceed a total current range of 13.5 A. If it does, some of the channels are automatically switched off. Thus, when all the channels are switched on the maximum current per channel is 540 mA (760 mA cm^{-2}, 0.713 cm^2 disc electrodes) with resolution 0.3 mA. On the other hand, when only one row (five electrodes) is switched on, the maximum current at each electrode can exceed 2 A but no more than 13.5 A jointly. The potentiostat also can control up to five temperature controllers. Eight K-type thermocouples were used.

1.1.5 Software and hardware

The LabView software, NuVant Computer-Assisted Screening Environment (CASE) written by Jun Zhang (NuVant Systems Inc.) V2.001, was used to control the Arraystat, acquire data and display graphs. NuVant CASE controls the PC embedded hardware PCI-6229, NI-DAQmx card, which is connected to Arraystat directly by USB-485 cable. A National Instruments card was used to apply commands to the potentiostat, which were set by the operator in the software. The software could run in two modes, simulation and DAQ card (real experiment). Thus, it is possible to run the software in simulation mode without connecting the Arraystat. The LabView based program (NuVant CASE) could control a maximum of eight mass flow controllers (model: BROOKS 5850S) in addition to the potentiostat (NuVant Arraystat). In addition, the software was developed during the experiments conducted as part of this thesis and I added additional features such as windows for coloured potential-current graphs and a folders list. This helps to save time needed for data analysis. Previously the researcher need to wait for the experiment to be completed and then perform the analysis. The modifications I introduced allowed the results of polarisation curves to be observed as test was running. The various polarisation curves were colour

coded to aid comparison. Similarly, the addition of a folder list meant that the data could be organized in a more easily accessible manner.

2 Key adjustable parameters

Use of the array fuel cell for screening of ORR catalysts first required optimisation of the operating conditions. In this section, each of the key adjustable parameters and its role in determining cell performance will be described.

2.1 The MEA

2.1.1 Compression of the MEA

One of the most important parameters influencing the results is compression of the MEA [16-18]. At the time of assembly of the array cell, the MEA is sandwiched between a graphite (anode) plate and a Garolite polymer plate with 25 embedded graphite sensors, and aligned with bolts positioned at the edges of the array. After that, the MEA was compressed. Initially the assembly was tightened with a torque wrench, applying 35 inch pounds torque on each bolt evenly in a symmetrical procedure. After approximately one hour, 50 inch pounds were applied similarly. This is according to the procedure defined by Smotkin's group at NuVant for DMFC testing. A blade feeler gauge was used to measure the gap thickness between plates and the compression was found to be greater than 40 %. This excessive compression crushes the Torray paper backing and diffusion layers of the MEA. This resulted in noisy and poorly reproducible data, so the procedure was modified.

As suggested by Ge et al. [19] roughly 75-85 % compression is expected to be most appropriate. Unfortunately, in the experiments, the available gasket thickness did not allow exactly 80 % compression to a thickness of 0.448 mm based on the Nafion 117 membrane (180 μm), carbon Toray paper – gas diffusion layer (190 μm) and reinforced Teflon gasket (120 μm). The thicknesses of catalysts' layers were omitted from the calculation, as these were deemed insignificant.

Thus, during every experiment carried out with different catalyst sets, all MEAs were compressed to between 305 μm (54.5%) – 356 μm (63.5%) values of compression. This over-compression allows good sealing of the MEA and prevents leaking of the gases in the array cell. After the MEA was assembled, a leak test was performed using liquid soap. The assembly was tightened with a torque wrench and the compression was confirmed using a blade feeler gauge.

2.1.2 Electrode distribution in the array

The standard test should include reliable and reproducible data. To achieve full reliability of the results, correct distribution of the electrodes of the same type needs to be accomplished. In other words, at least one electrode of the same kind has to be positioned in each of five flow fields. To accomplish this a Latin square [1], such as that shown in Figure 5, was used.

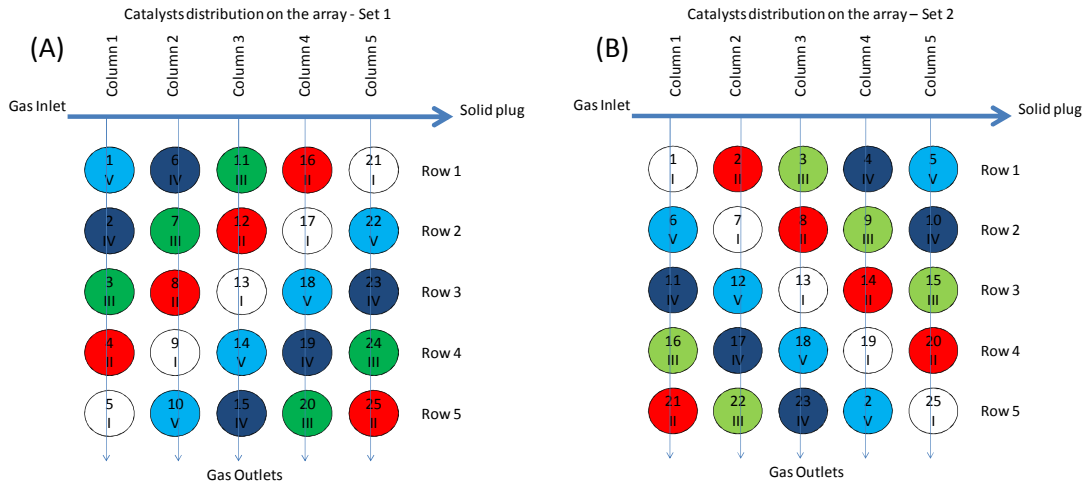

Figure 5 Five different catalysts were distributed on the array in a Latin square arrangement. A pattern for (A) First experiment (B) Repeated experiment using new MEA with different electrode distribution, made of the same set of electrodes.

Data were typically collected for two minor arrangements of the Latin square by rotating the MEA, as there is the additional factor of the position of the gas inlet.

2.2 Flow rate calibration

2.2.1 Anode

The anode graphite plate has a large common flow field of 103 cm^2 area. In theory, gas distribution should be homogenous and have the same flow rate over the whole flow field region. Unfortunately, performances could change locally. The problems were flooding, rapid drying out and high proton resistance of the Nafion® membrane. For this reason, the appropriate flow rate needed to be established. The pressure of the gas cylinder (N_2 or H_2) was set to 80 psig. The flow rate was set to 100 SCCM (cm^3 min^{-1}) and was controlled by a precise mass flow controller. Too fast a flow rate can dry out the MEA. A sluggish flow does not provide enough water to humidify the membrane properly because of humidifier performance. A rapid flow can blow water out of the system.

2.2.2 Cathode

Control of the cathode flow rates was much more complicated. Figure 6 shows the array cell with highlighted gas flow directions and orifice valves. The gas cylinder (N_2 or O_2) was set

to 80 psig as in the anode. The difficulties start at the five orifices, which provide, conduct and regulate gas flow rate to the five separate flow fields. The major pressure drop occurred at the orifice valves. In addition, the orifices cannot conduct gases at high humidities as excess water can stick inside the orifices and block the flow. Flow rates on each flow field were adjusted using the valves to provide 80 SCCM (cm^3 min^{-1}). The orifices needed to be tested several times after calibration and the flow rates were checked several times to make sure they did not change over time. Flow rate calibration was performed using a digital flow meter (ambient temperature gases only) and bubble-o-meter (10 cm^3 and 100 cm^3 volumes) for heated gases.

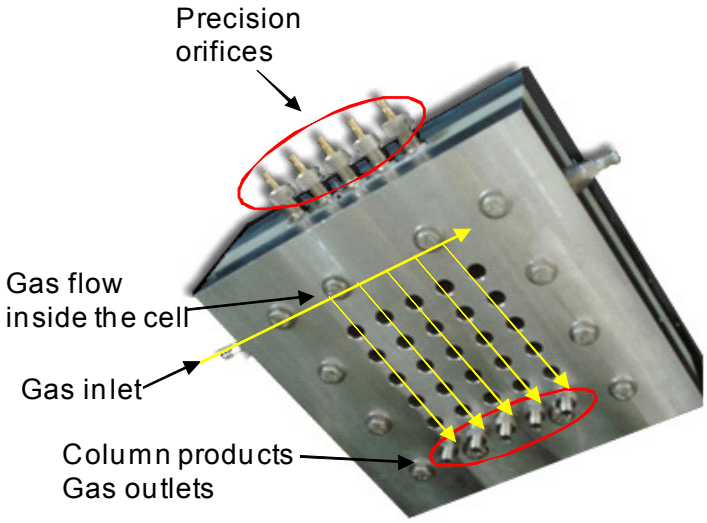

Figure 6 Orifice valve location and gas flow on the cathode flow fields in the cell.

2.3 Temperature of the system

The system can have up to eight temperature controllers which coordinate heat application. Temperature controllers are placed both in humidifiers and in the lines providing humidified gases to the array cell. Furthermore, both sides of the cell were heated with two heating cartridges provided by Watlow (100 W each cartridge, serial number C6A-7595) each side (Figure 7). In addition, heating tape was applied to heat up cold parts of the cell such as the orifice valves. Moreover, my suggestion to relocate a relief valve, which was located on the other side of the arraycell, to a position opposite the cathode gas inlet, was a success. The relief valve had been acting as a 'cold finger' when in the original position. The temperature of the MEA is assumed to be that of the anode as the cathode plate is an insulator.

2.3.1 Cell heating cartridges

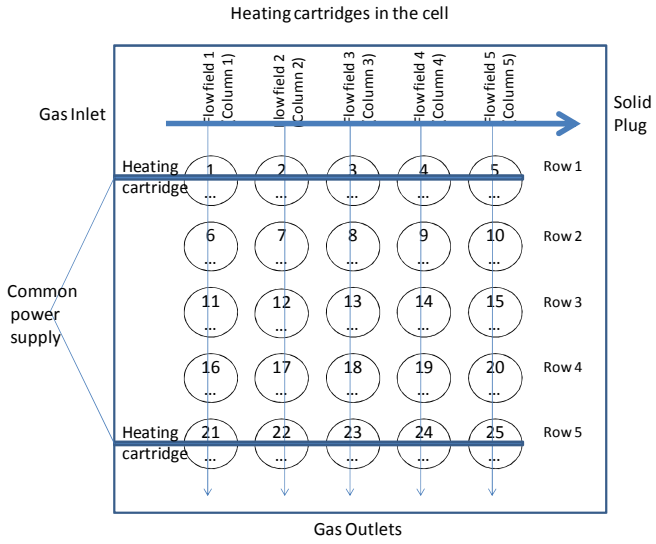

Figure 7 Position of heating cartridges in the array cell (anode graphite plate).

Application of heat to the array cell is performed using heating cartridges (anode graphite plate), whose positions are presented in Figure 7. The cartridges were inserted and positioned near Row 1 and Row 5. A thermocouple was positioned in between two heating cartridges near Row 3. To make sure the temperature distribution in the array cell was uniform, measurements with a thermal visor camera were conducted. The image of the temperature gradient on the front panel of the cell is shown in Figure 8.

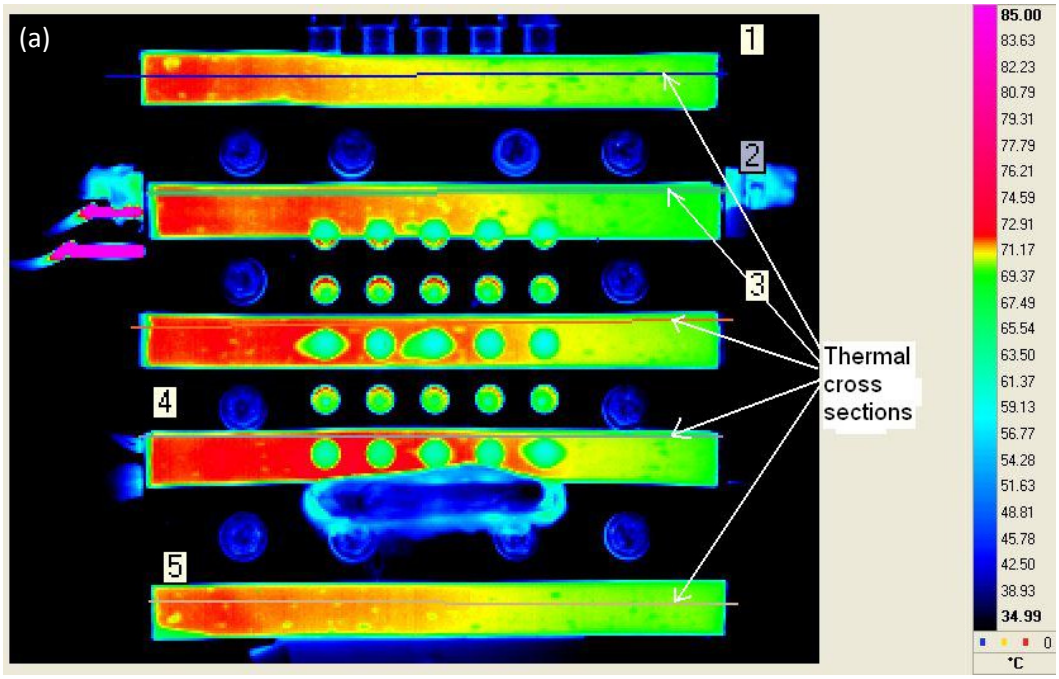

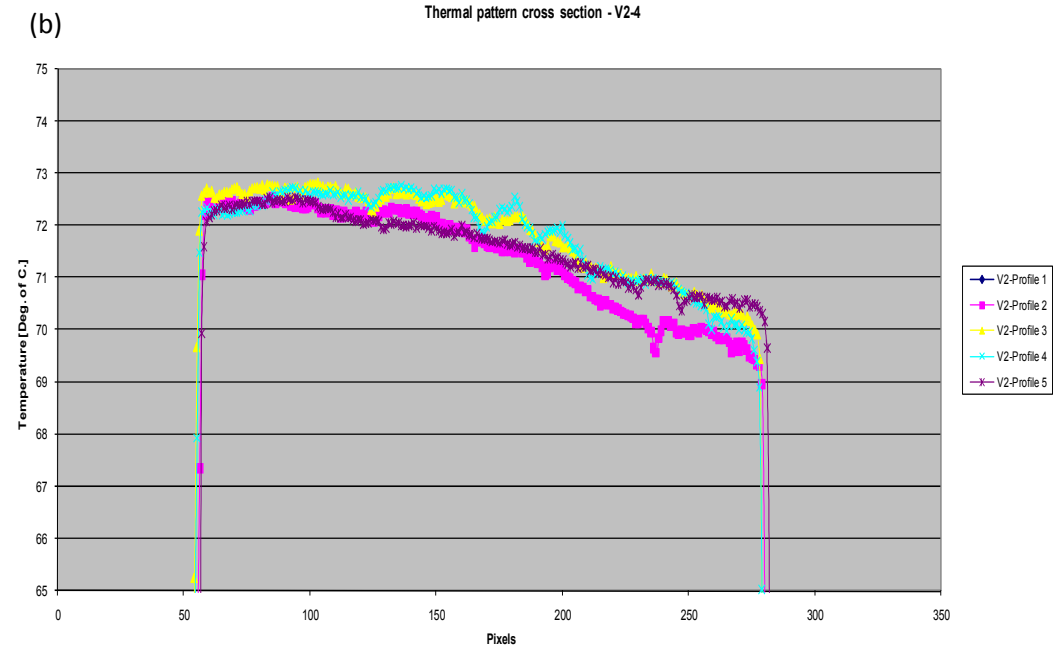

Figure 8 The thermal visor (a) image of the front panel (b) profiles of the front panel of array cell.

Five thermal cross sections can be identified in Figure 8(a); these cross sections represent the thermal profiles extracted and shown in Figure 8(b). A drop in temperature of approximately 2.5 $^{\circ}$C occurred from the right to the left side of the front panel. However, the temperature of the central area of the panel, where the 'array' is positioned, was similar with the exception of the column 5 region. To heat the entire plate uniformly, a better design of heating system is needed.

2.3.2 Humidifiers and heating lines

During the experiments both humidifiers were controlled by thermocouples placed just above the water level. The small capacity of the humidifier (500 cm^2) enabled a constant temperature of 90 °C to be applied for no longer than 6 hours. After this time the chamber ran out of water. The humidifier was refilled with cold water and consequently it took 30 to 45 minutes to stabilise the temperature.

2.4 Humidification studies

An investigation of the effects of humidification conditions [6, 9, 10, 20-23] on ORR activity performance was carried out by varying the temperatures of the array cell and the external fuel cell system components. Variation of the water balance in the system was achieved by increasing the counter humidifier (CH) temperature while maintaining the graphite plate (Cell) at 50 °C (Figure 9 A-D), while the working humidifier (WH) remained at 40 °C. This low temperature had the effect of reducing the partial pressure of water at the cathode side. Similarly the effects of cell temperature were investigated and the results are shown in Figure 9 E-G.

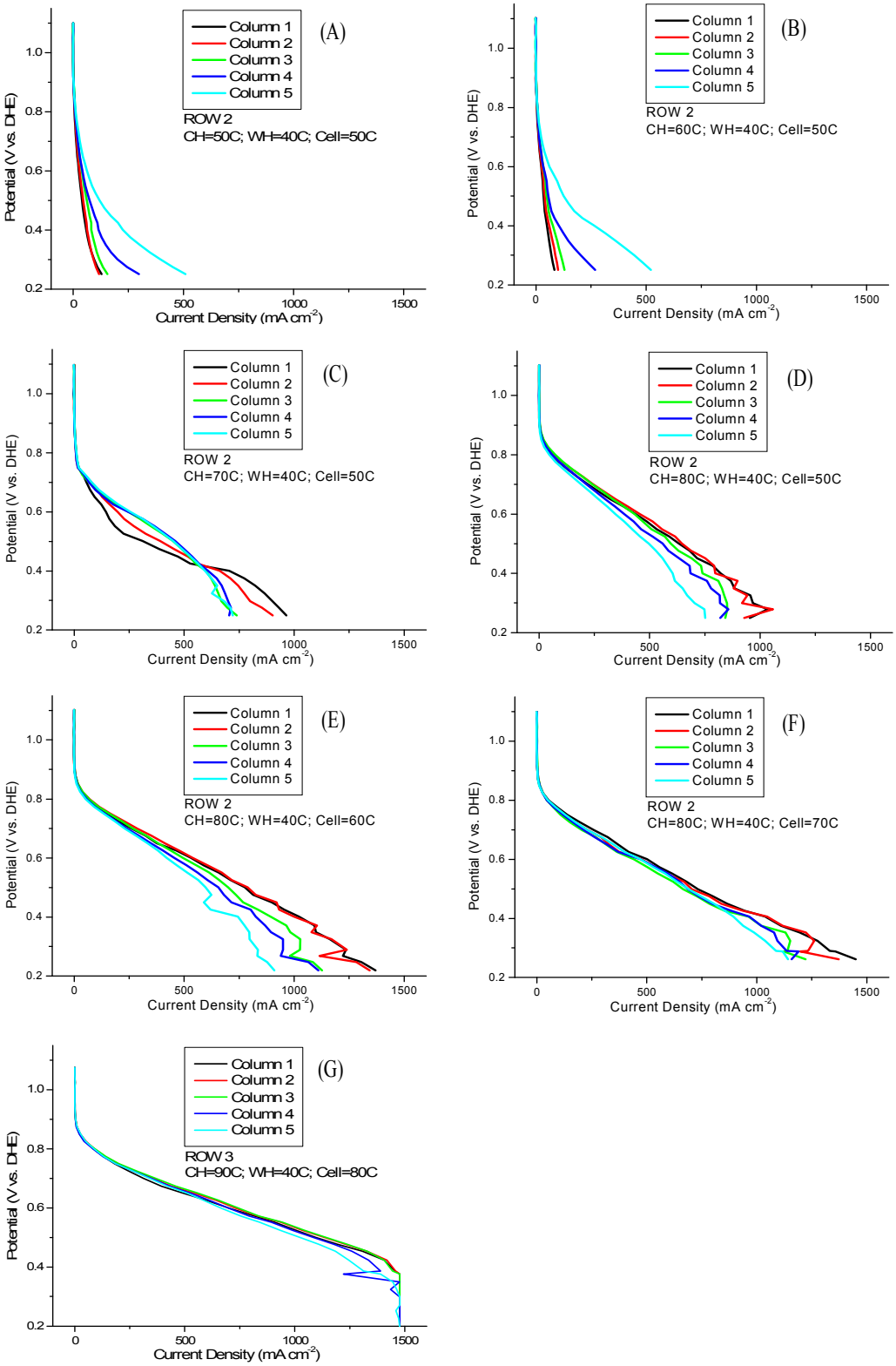

Figure 9 Polarisation curves acquired at different temperatures of the system elements: counter humidifier (CH), graphite plate – counter/reference electrode (cell), working humidifier (WH). The MEA consisted of 25 identical 60 wt % Pt/C (0.457 mg_{Pt} cm^{-2}) working electrodes, a Nafion 117® membrane and a 60 wt % Pt/C anode (0.38 mg_{Pt} cm^{-2}).

The effects of increasing the counter humidifier temperature are seen by employing panels A (50 °C), B (60 °C), C (70 °C) and D (80 °C). As humidification was increased, the current densities achieved increased and the data became more reproducible over the five columns/flow fields. Similarly, the effects of increasing the cell temperature whilst keeping CH at 80 °C can be seen by comparing panels D (50 °C), E (60 °C) and F (70 °C). The effects of the cell temperature are less significant than the variation of the humidification, but the most reproducible data were obtained for the higher temperature.

To account for incomplete humidification, the humidifier temperature should be maintained at least 10 °C above the cell temperature. Thus, for the final data set in this series, panel G, the cathode humidifier temperature was increased to 90 °C for a cell temperature of 80 °C. The results are very similar to those of Figure 9 F and accordingly the retrieved 80 °C (CH)/ 70 °C cell or 90 °C (CH)/ 80 °C cell temperatures were used in the studies repeated later in this chapter.

2.5 Scan rate and potential limits

The main purpose of the experiment presented below was to elucidate the influence of varying potential scan rate on data acquisition and data quality.

The scans shown in Figure 10 were carried out between potential limits of 0.6 V and 0.95 V vs. the dynamic hydrogen electrode (DHE) [24], which is the anode of the MEA. These limits represent the kinetically controlled region of the polarisation curves. Applications of potentials higher than 0.95 V were avoided as catalyst degradation and significant platinum surface area losses have been reported [24-28] at high cathode potentials.

In this experiment, the potentials were held for different time intervals followed by potential steps of (A) 5 mV, (B) 10 mV or (C) 25 mV. The time intervals between the steps were 30 s, 30 s, and 60 s, respectively. The temperatures of the system components were as follows for all the experiments: the counter humidifier (CH) was set at 90 °C, the graphite plate – counter/reference electrode side (Cell) 80 °C, aluminium plate – array working electrode side (Al) 50 °C and working electrode humidifier (WH) 40 °C. The data were collected with an array electrode inlet-pressure of 80 psig (O_2) on the high-pressure side of the orifice valves, which correlates to about 80 cm^3 min^{-1} at near zero gauge pressure across each column of electrodes. Humidified H_2 was delivered to the counter electrode at 100 cm^3 min^{-1} at 0 psig back pressure.

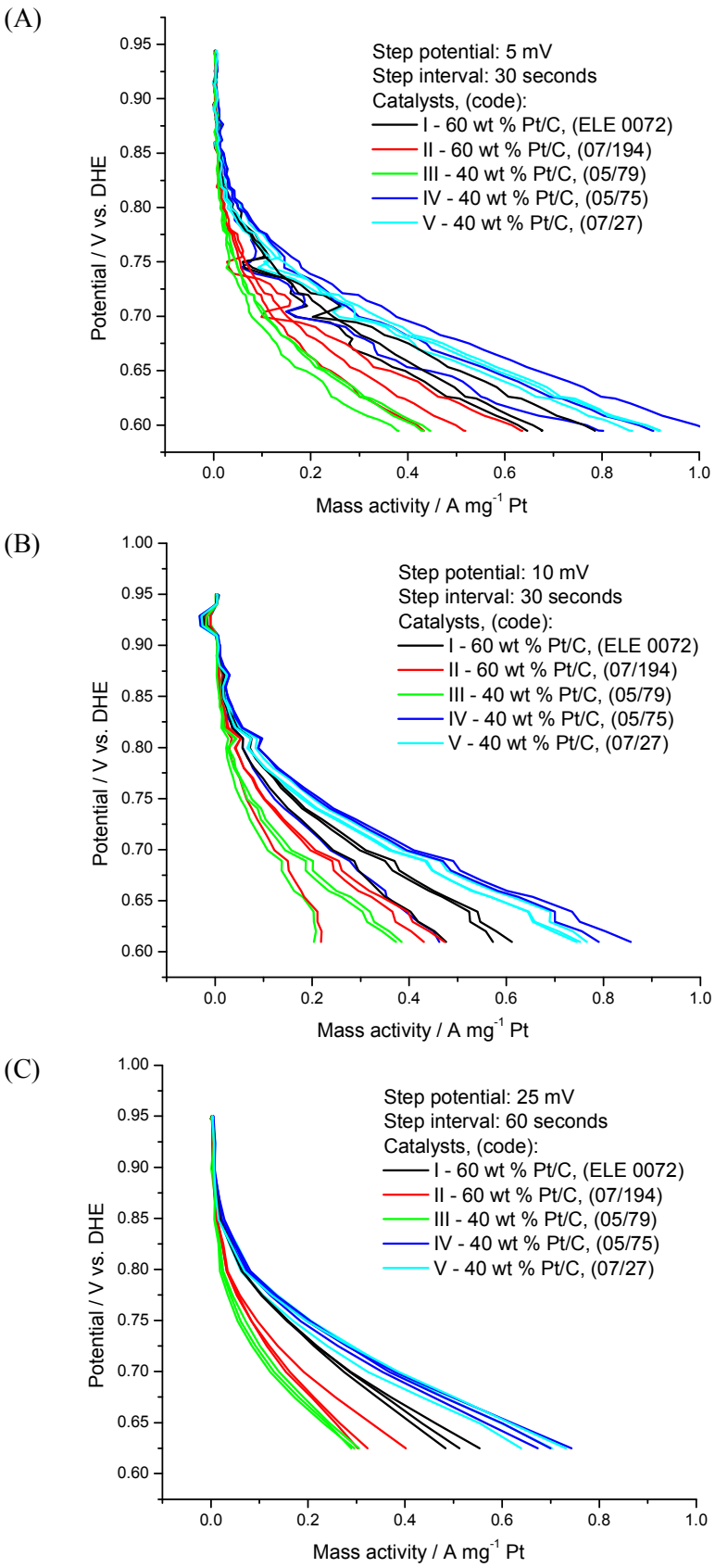

Figure 10 Effect on data acquisition quality of different scan rates: A) step potential 5 mV, step interval 30 seconds; B) step potential 10 mV, step interval 30 seconds; C) step potential 25 mV, step interval 60 seconds. Each curve represents results collected for one electrode on the array.

The data acquisition method plays an important role in determining data quality. After each potential step a stabilisation period is required. Only the very last data points of each step potential are used to plot the polarisation curve. A compromise must be made between data density (step size) and speed of measurement (step interval). As can be seen in Figure 10, the cleanest looking data are obtained with a 25 mV step size and 60 s step interval. Accordingly these conditions were used throughout the rest of the work reported in this chapter.

2.6 Collection modes

The new design of the Arraystat potentiostat allowed electrode switching to be applied. If a particular channel is not needed to take part in the experiment, then it may be excluded by changing a software setting. This means that any channel could be eliminated from the measurements at any time. In this case, the experiments were run in two modes described in detail below. The first investigation was named 'simultaneous mode' because all the electrodes remained turned on during the whole experiment. The second collection method was termed 'row switching mode'. This feature was used to avoid problems caused by inconsistencies in the reactant concentration and water content.

2.6.1 Simultaneous mode

The scan shown below in Figure 11 was carried out using simultaneous mode, i.e. all 25 electrodes were scanned at the same time. This method suffered from 'downstream effects' in which water produced during the cathode reaction at the electrodes at the top of the cell affected the humidification of electrodes lower down the cell. This locally produced water could have a dramatic effect on the humidification of electrodes positioned lower down in the cathode flow field.

The simultaneous scan was run from 1 V to 0.6 V potential. Each averaged data point was collected following a 25 mV step with 60 second interval. The hydrogen gas flow on the anode – counter/reference electrode (103 cm^2) side was set at 100 cm^3 min^{-1}. The oxygen at the Cathode/25 channel array – working electrodes (0.713 cm^2 area each) side electrode inlet-pressure was 80 psig (O_2) on the high-pressure side of the orifice valves. The oxygen gas flow was set at around 80 cm^3 min^{-1} for each of five flow fields. The temperature of the cell was set to 80 °C. Anode humidifier temperature was set to 90 °C and the cathode humidifier was at 40 °C. Different cathode catalysts were used, arranged in the Latin square shown in Figure 5.

The individual polarisation curves for each of the 25 electrodes are plotted in Figure 11. The five curves for each catalyst type (colour of line) are grouped together, but there is a fairly wide spread to the data. In particular, for catalyst (a) and (e) there are clear outliers. These curves correspond to electrodes where the working electrode discs did not line up well with the sensor electrodes and were excluded from further analysis.

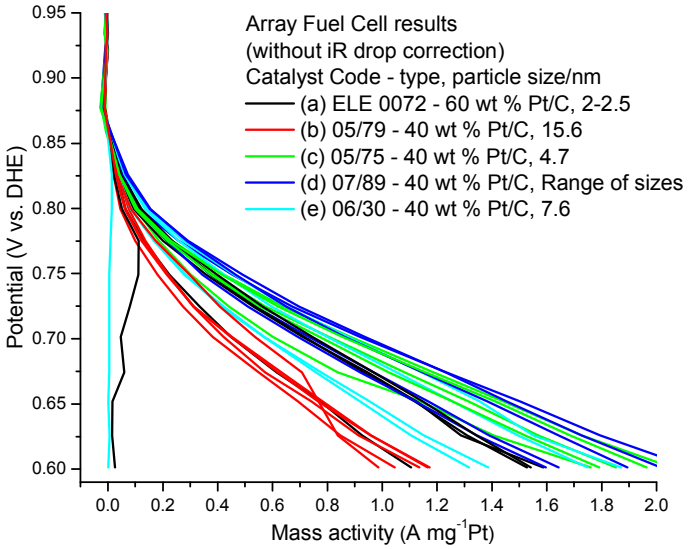

Figure 11 Polarisation curves of all 25 array electrodes. The array ORR polarisation curves were acquired simultaneously and the data were normalised by Pt loading. The voltage of the cell was not iR corrected. The details of five catalysts tested were depicted in Table 1. Array conditions: The scans were run from 1 V to 0.6 V potential. On the Anode – counter/reference electrode (103 cm^2) side hydrogen gas flow was set at 100 cm^3 min^{-1}. The temperature of the cell was 80 °C. Anode humidifier temperature was 90 °C. On the Cathode/Array – working electrodes (0.713 cm^2 area each) side oxygen gas flow was set at around 80 cm^3 min^{-1}. Cathode humidifier was at 40 °C. On both sides of the gas flow back pressure was not applied.

The five curves for each catalyst type were combined, excluding the outliers mentioned above, and the results are presented in Figure 12. The error bars represent the standard deviations at each point. The details of the effects of each catalyst type for this set will be discussed later in section 4.1.1. The results obtained in simultaneous mode are satisfactory, and have the advantage of collection speed compared to the row switching mode described below.

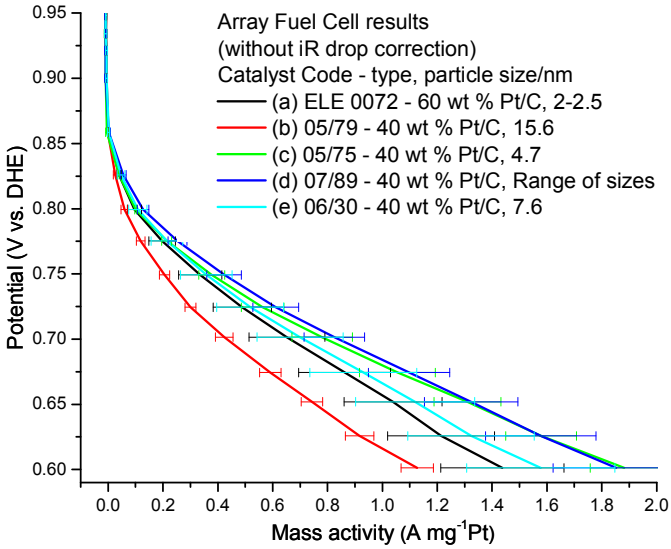

Figure 12 Average results of five electrodes examined take out from Figure 11.

2.6.2 Row switching mode – Five catalysts set

Row switching mode was applied to eliminate reactant depletion and water production (downstream) effects. In this mode each row is tested separately, starting from the bottom row of the cell.

Prior to commencing the scan, each row was preconditioned (soaked) at 0.7 V potential for two hours. The row switching mode scans were run from 1 V to 0.15 V potential, stepping every 25 mV and holding for 60 second intervals. The hydrogen gas flow on the anode side was set at 100 cm^3 min^{-1}. The oxygen at the cathode side electrode was set to 80 psig (O_2) on the high pressure side of the orifice valves. The oxygen gas flow was regulated manually using orifice valves at around 80 cm^3 min^{-1} for each of five flow fields. The temperature of the cell was set to 80 °C, the anode humidifier to 90 °C and the cathode humidifier to 40 °C. The same MEA was used as in the simultaneous collection presented in section 2.6.1.

The results for all 25 catalyst electrodes are shown in Figure 13, to enable comparison of the spread of the data with that presented in Figure 11 for the simultaneous collection. Finally, the averaged data are presented in Figure 14. Unfortunately, the expected improvements in the reproducibility of the data were not realised by use of the row switching mode. We speculate that this may be attributed to variations in cell temperature and humidification between measurements at each row that are greater than the variations caused by the downstream effects present in the simultaneous measurements.

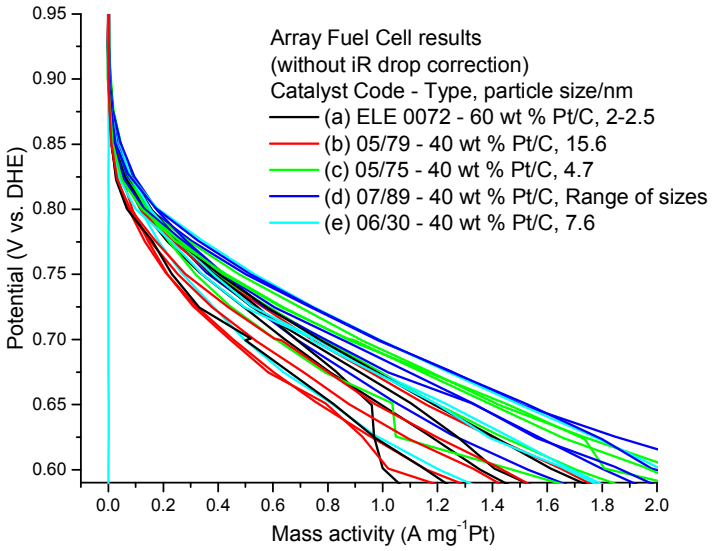

Figure 13 Results obtained using row switching mode. All the results from five rows were plotted on the same graph for comparison. The experiment starts scanning from the bottom Row 5, sequentially going up the cell, Row 4, Row 3 etc. respectively. Switching mode was used to eliminate reactant depletion (downstream) effects. Each row was preconditioned (soaked) at 0.7 V potential for two hours. The scans were run from 1.1 V to 0.15 V potential. All the other parameters were the same as in the caption of Figure 11.

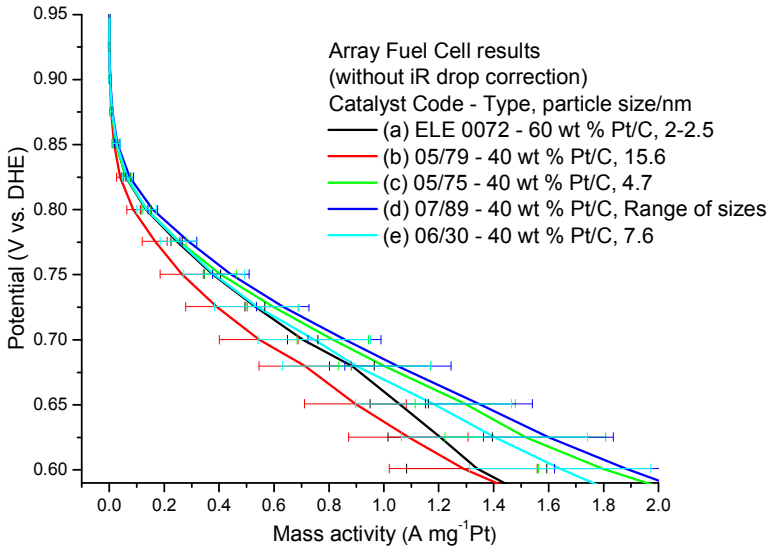

Figure 14 Average of the results derived from row switching measurements of Figure 13.

3 Reproducibility tests – Electrochemical characterisation

An important feature of testing catalysts using the array cell is the ability to obtain enough data simultaneously to ensure the statistical significance of array results. Such statistical significance, however, relies upon confidence in the reproducibility of the data and its independence of the position of the electrode in the cell. This was tested by preparing an MEA in which all 25 electrodes were identical.

A series of experiments with varying temperature and scan rate was carried out using an MEA consisting of a common counter electrode and 25 identical working electrode discs. Both electrodes were made of 60 wt. % Pt/C (ELE 0072) catalyst. In theory, the ORR activity of all 25 cathode (working) electrodes should be identical. However, differences in performance were observed in practice. These differences may be attributed to either the MEA preparation, e.g. difficulty occurred with good fitting of the working discs into the gasket, or variations in gas composition, flow rate, humidification or temperature as a function of position in the array. These effects are explored and quantified in this section.

3.1 Cyclic voltammetry

Before the ORR testing procedure was applied, the MEA was checked by measuring cyclic voltammograms of each of the electrodes in the array. This helps to check the reproducibility of the electrodes on the array. Faulty connections were detected and those electrodes which were not aligned properly at the time of MEA preparation were revealed. Normally, the 'dead' electrodes are apparent through the lack of or small amplitude of the current in comparison to others from the same row. Such faulty electrodes were excluded from further analysis.

Figure 15 presents averaged CVs for each of the rows in the cell obtained using a 2 mV s^{-1} scan rate. Current is observed below 0.1 V, corresponding to hydrogen evolution. No features attributed to the usual hydrogen adsorption/desorption or oxide formation/stripping at Pt were observed. However, these cyclic voltammograms clearly indicate the current offset of the system. Each Arraystat has a different specific offset on the current scale and this is identified by placing the double layer region of the cyclic voltammogram around zero current. In this case, the CVs are approximately straight lines and are positioned above zero, by 1 to 3 mA for all 25 channels. An average value 2 mA was taken as the offset. This value was be subtracted from every experiment performed using this particular Arraystat.

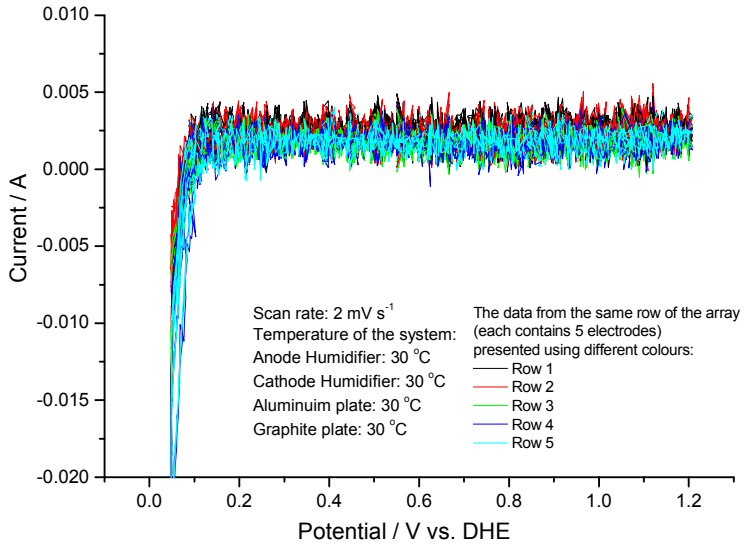

Figure 15 Experiment showing offset of the potentiostat. Scans were carried out at 2 mV s^{-1} scan rate. Cyclic voltammograms performed using all 25 identical electrodes, 60 wt % Pt/C. The potential was cycled between 0.05 and 1.2 V vs. DHE. The temperature of all the system components was 30 °C. Hydrogen flow rate at the anode was 100 cm^3 min^{-1} (0 psi back pressure). Nitrogen flow rates were 80 cm^3 min^{-1} for each flow field (0 psi back pressure).

Cyclic voltammetry was also used to establish appropriate temperature, humidification and gas pressure conditions for data acquisition. Changing the temperature of the system components will amend the humidification conditions. Due to that process, the performance of the entire system could change the testing environment. CVs acquired at cell temperatures below 50 °C show a wide spread of current densities, especially if the comparison is made within columns (flow fields), as shown in Figure 16. On the other hand, the CVs within rows showed remarkable similarity. An important observation is that in the same flow field the cathode flow rate is identical. This means that there must be issues other than flow rate and this is not the dominant factor determining the response of individual electrodes.

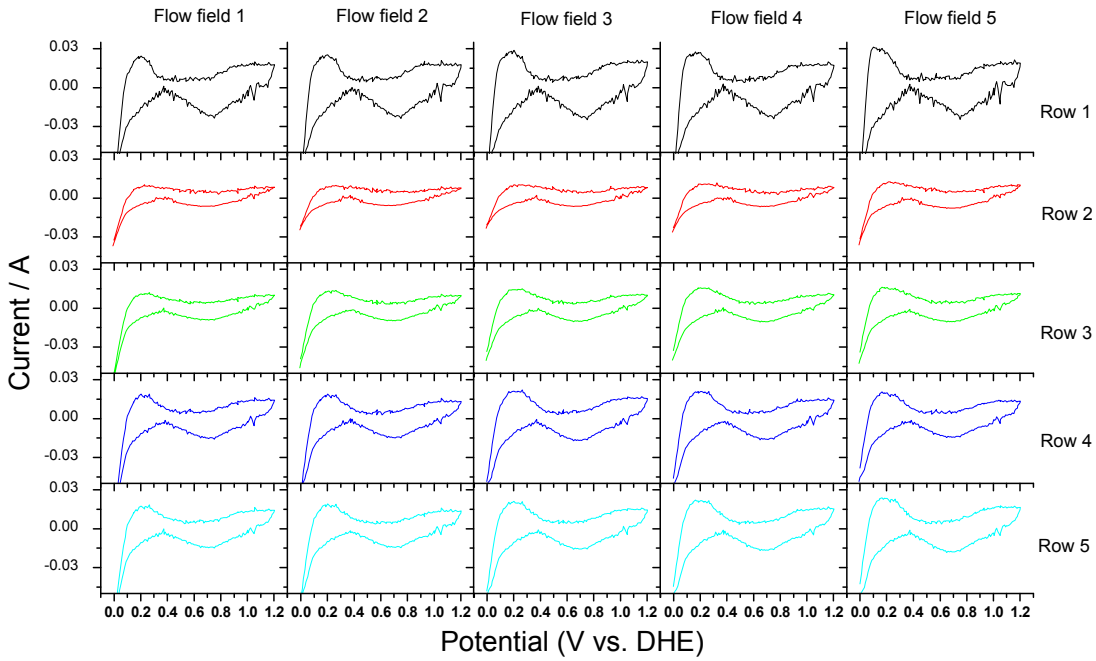

Figure 16 Comparison of cyclic voltammograms for 25 identical electrodes on the array, made of 60 wt. % Pt/C (ELE 0072) electrocatalyst. The potential was cycled between 0.05 and 1.2 V vs. DHE (Dynamic Hydrogen Electrode). The first scan is shown. The voltammograms present currents without normalisation. Experiments were carried out at 100 mV s^{-1} scan rate. The temperature of all the system components was 50 °C. Hydrogen flow rate on the anode was 100 cm^3 min^{-1} (0 psi back pressure). Oxygen flow rates were around 80 cm^3 min^{-1} for each flow field (0 psi back pressure).

There are two other obvious parameters which may determine response: temperature and humidification. The two heating cartridges are positioned in the graphite plate of the anode, which is responsible for cell temperature, near Row 1 and Row 5, and the resulting temperature gradient could be significant. The higher temperatures near the top (Row 1) and bottom (Row 5) rows appear to affect activity, and CVs from electrodes located in those rows appear to have higher current densities and sharper features.

This is further highlighted in Figure 17, which shows the average of all five electrodes in each row and the corresponding standard deviations (error bars). Row 1 had the highest performance. However, very similar results were found for Rows 4 and 5, thus suggesting that the temperature gradient was not sufficient to explain the variation.

It is of particular note that Row 1, which is closest to the inlet (orifice) valves, tended to perform better than the other rows. A pressure drop occurs across the orifice valves and it is likely that water from the humidification of the gases would condense out at this point. This water would keep both the Nafion 117® membrane and Nafion® in the catalyst layer more completely hydrated in comparison to the other rows. The utilisation of the catalyst layer

(apparent active surface area of the Pt catalyst) is greater when the electrodes are well hydrated. The explanation of why Row 2 gave a poor current response remains unclear.

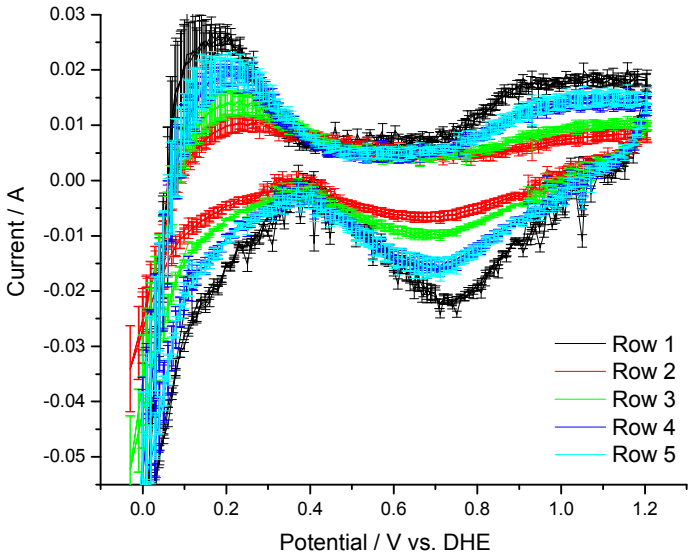

Figure 17 Cyclic voltammograms shown are average results with error bar (standard deviation) from Figure 16. CVs were averaged over five electrodes of the same row.

CVs were also obtained with the array operating at 60 °C and the results are more uniform across the entire array, as shown in Figure 18. The CVs from Row 1 have a bit more noise and slightly higher current densities. The noise may be related to the proximity of the orifice valves or some problems with the equipment. It is likely that a further increase in temperature would result in additional improvements in the quality and reproducibility of the data, but this was not possible with the system at the time of these measurements.

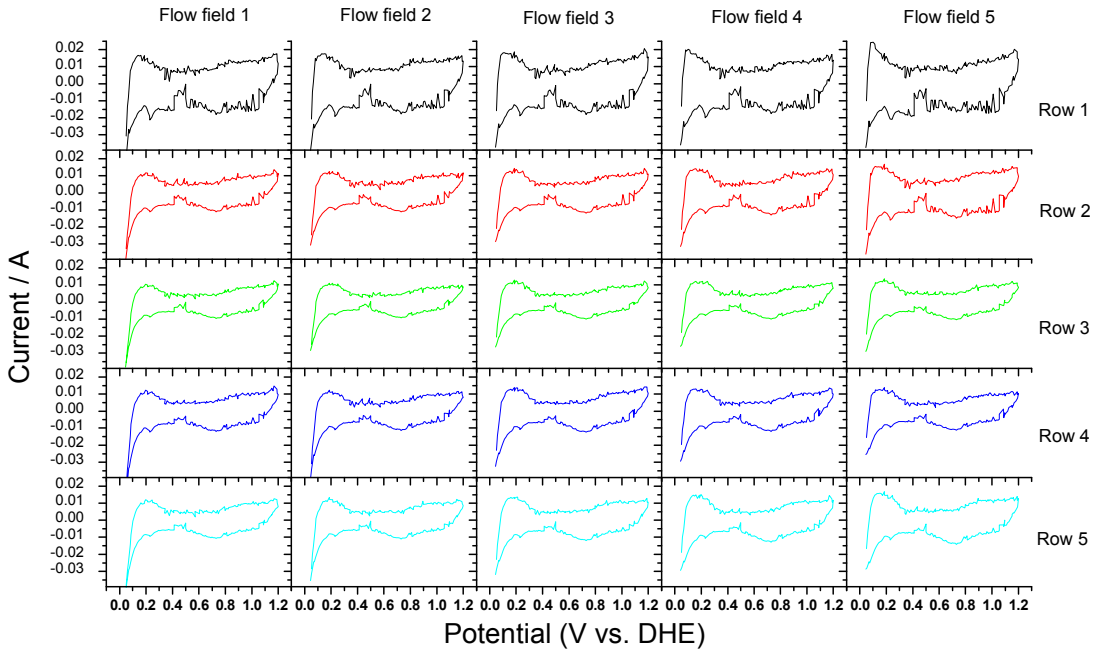

Figure 18 Cyclic voltammograms for 25 identical electrodes on the array at 60 °C at 50 mV s^{-1}.

The average CVs including error bars (standard deviation) for each row are shown in Figure 19. The CV experiments indicate that reasonable reproducibility can be obtained for Rows 2 through 5.

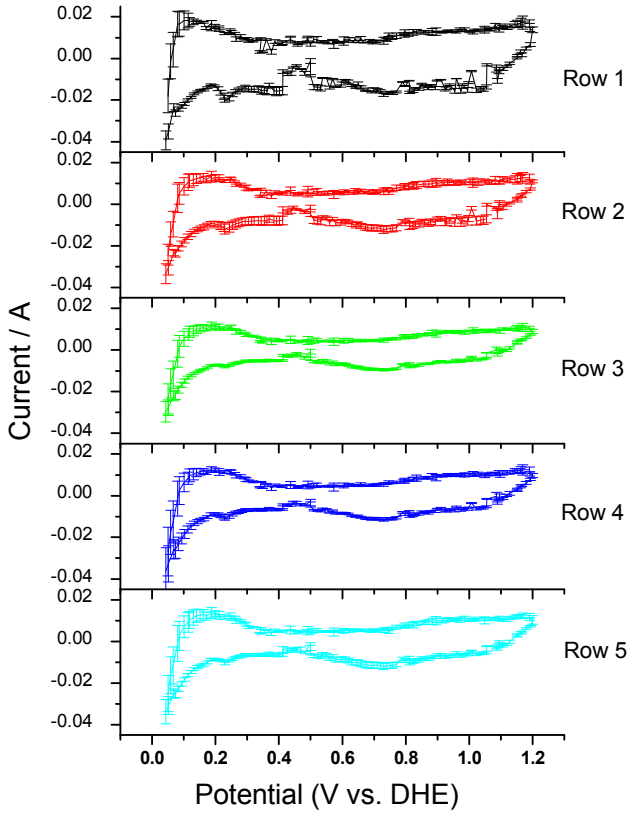

Figure 19 Cyclic voltammograms present average results with error bar (standard deviation) from Figure 18. CVs shown were averaged over five electrodes of the same row.

3.2 Oxygen Reduction Reaction – Polarisation Curves

3.2.1 25 identical electrodes

Once reproducible conditions for the cyclic voltammograms had been established, the reproducibility of the oxygen reduction behaviour of the array was established using the same 25 identical electrode MEA. The scans were run between 0.2 V and 1.1 V vs. the Dynamic Hydrogen Electrode (DHE). The potential was held for 60 second intervals following 25 mV steps. The temperatures of the system components were set to counter humidifier (CH) 80 °C, graphite plate – counter/reference electrode side (Cell) 70 °C, aluminium plate – array working electrode side (Al) 50 °C, working humidifier (WH) 40 °C. The inlet pressure was set to 80 psig for oxygen on the high pressure side of the orifice valves, which correlates to approximately 80 cm^3 min^{-1} at near zero gauge pressure across each of the five flow fields (columns). Humidified hydrogen was fed to the anode-counter/reference side at 100 cm^3 min^{-1} with 0 psig back pressure delivered to the counter electrode.

Figure 20 shows representative data obtained with the counter electrode and all array spots loaded with 0.457 mg cm^{-2} of 60 wt. % Pt/C. Nafion 117 membrane was used. The data were acquired using the row switching mode as described in section 2.6.2; i.e. only the five electrodes in the row were measured simultaneously. The experimental procedure was set to acquire the bottom row, Row 5, first, going gradually up the flow field, to Row 4, Row 3 etc. This avoided excessive water produced at the row above from influencing the data for the next row scanned.

It is clearly seen from Figure 20 that problems with gas flow occurred in column/flow field 5. These difficulties are attributed to flooding of the flow field channels. Water produced in ORR reaction at high current densities (lower potentials) together with water supplied to the system with humidified gases causes this problem.

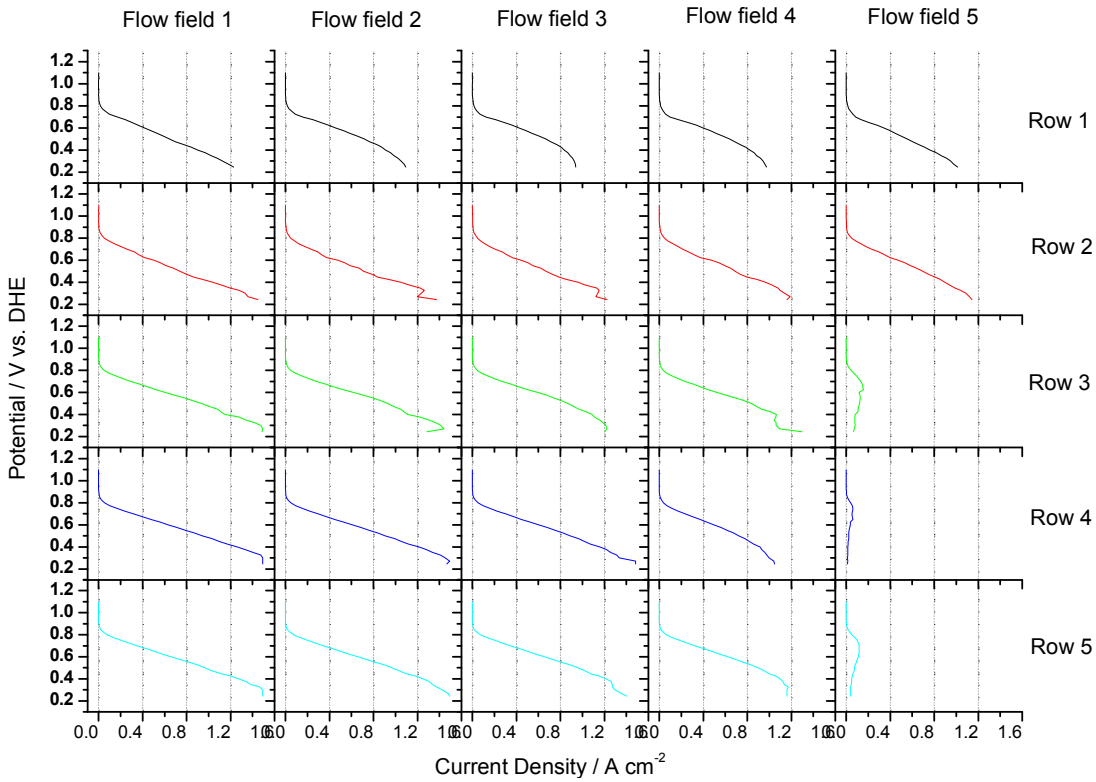

Figure 20 Effect of row switching mode on the performance of 25 identical working electrodes (60 wt % Pt/C) Parallel array cell set at 70 °C. Both electrodes 0 psig back pressure. Anode – counter/reference H2 flow set at 100 $cm^3 min^{-1}$. Anode humidifier at 80 °C: Array – working, cathode: O2 at around 80 cm^3 min^{-1}, Cathode humidifier at 40 °C. Switching mode used to eliminate reactant depletion (downstream) effects.

The anode gas inlet is positioned next to Flow field 5 and Row 1. The position of the inlet may cause flooding of the electrodes nearest to the inlet, as the water from humidification of the anode gas is more likely to condense at the gas inlet of the anode flow field. Some experiments revealed good performance for all 25 electrodes. Unfortunately, even then differences in current performances could still be identified, especially at potentials below 0.75 V.

Figure 21 shows the current densities at 0.8 V vs. DHE extracted from the experimental polarisation curves presented in Figure 20. The lowest performance was observed for Row 1, and this could be attributed to lack of oxygen humidification on the cathode side. The cathode sparger was set to only 40 °C; this did not ensure high enough humidification. Humidification is contributed mostly by the anode gases and is more effective further from the cathode inlet. Due to better Nafion® membrane hydration, the resistance is lower, hence the greater currents. Gradually going down the flow field the rows showed higher current density performances, which is attributed to an increase in the oxygen humidification due to water migration through the membrane. This can explain why current densities changed as the temperature and humidification conditions in the array were varied. Only 20 electrodes

out of 25 show reasonable reproducibility. The average results for these 20 electrodes (Rows 2 -5) collected at 0.8 V potential equal 0.052 A cm $^{-2}$ with standard deviation of 0.013 A cm $^{-2}$.

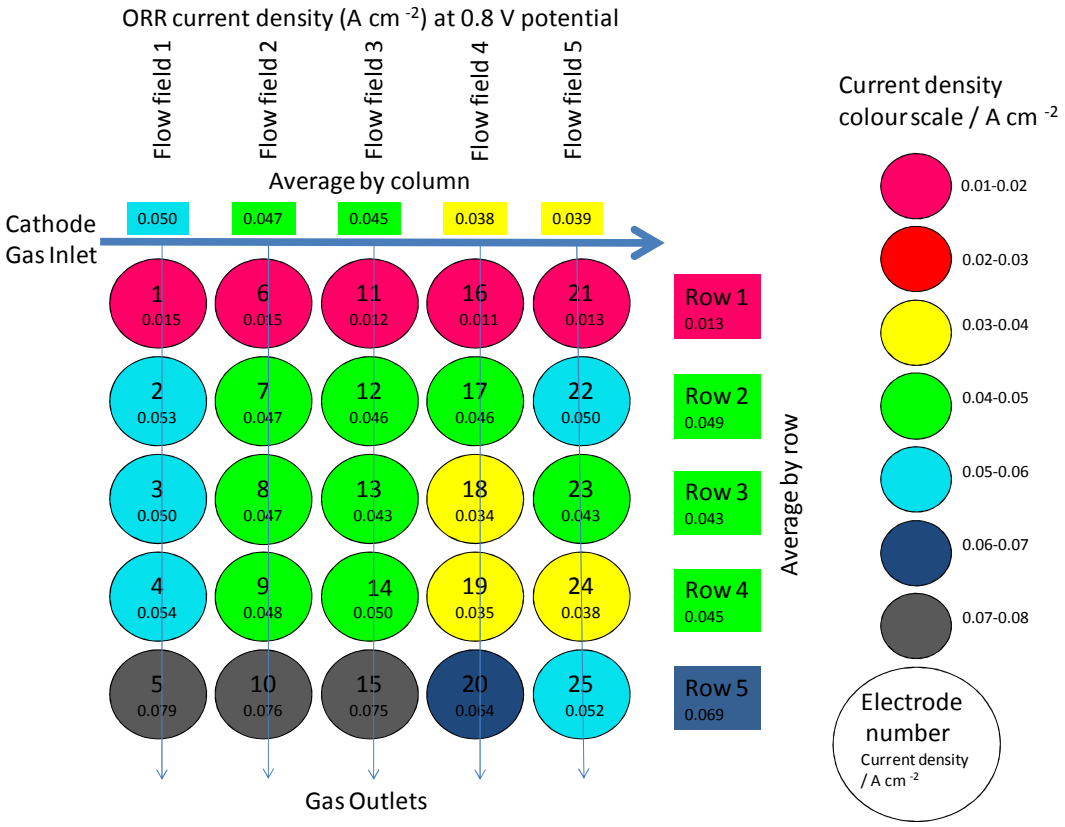

Figure 21 Schematic of all 25 array electrodes performance. Current density measured at 0.8 V potential vs. DHE. Full experimental scans for each electrode are shown in Figure 20.

3.2.2 Experiment with five different catalysts

This experiment was carried out to prove the reproducibility of the results acquired in the conditions described below. The second purpose of this experiment was to investigate how the ORR performance was affected by different particle size [27, 29-31] and carbon types [32, 33] of the Pt catalysts.

The scans were run between 0.6 V and 1.0 V vs. Dynamic Hydrogen Electrode (DHE). The data from each row were acquired separately in two-hour intervals using row switching mode. The MEA consisted of 5 different working electrode catalysts as described in Table 1 arranged in the Latin square shown in Figure 5, a Nafion 117® membrane, and common 60 wt % Pt/C anode. Before each acquisition scan, the electrodes from each row were conditioned by soaking at 0.7 V for one hour. The potential was held for 60 second intervals following 25 mV steps. The temperatures of the system components were set to counter humidifier (CH) 90 °C, graphite plate – counter/reference electrode side (cell) 80 °C,

aluminium plate – array working electrode side (Al) 50 °C, working humidifier (WH) 40 °C. The inlet pressure was set to 80 cm^3 min^{-1} for oxygen on the high pressure side of the orifice valves, which correlates to approximately 80 cm^3 min^{-1} at near zero gauge pressure across each of the five flow fields (columns). Humidified hydrogen was fed to the anode-counter/reference side at 100 cm^3 min^{-1} with 0 psig back pressure.

Table 1 Catalysts used in the experiment. Five electrodes made of each type of catalyst were positioned in the array using a Latin square method as shown in Figure 5(a).

Investigation of Pt surface area – particle size effect no.1					
Catalyst order	**Catalyst code**	**Catalyst type**	**Pt loading / mg_{Pt} cm^{-2}**	**Particle size (XRD results)**	**CO metal area / m^2 g^{-1}_{Pt}**
(a)	ELE 0072	60%Pt/C	0.457	2 – 2.5	78-100
(b)	05/79	40%Pt/C	0.32	15.6	13
(c)	05/75	40%Pt/C	0.31	4.7	83
(d)	07/89	40%Pt/C	0.31	Range of sizes	43
(e)	06/30	40%Pt/C	0.35	7.6	---

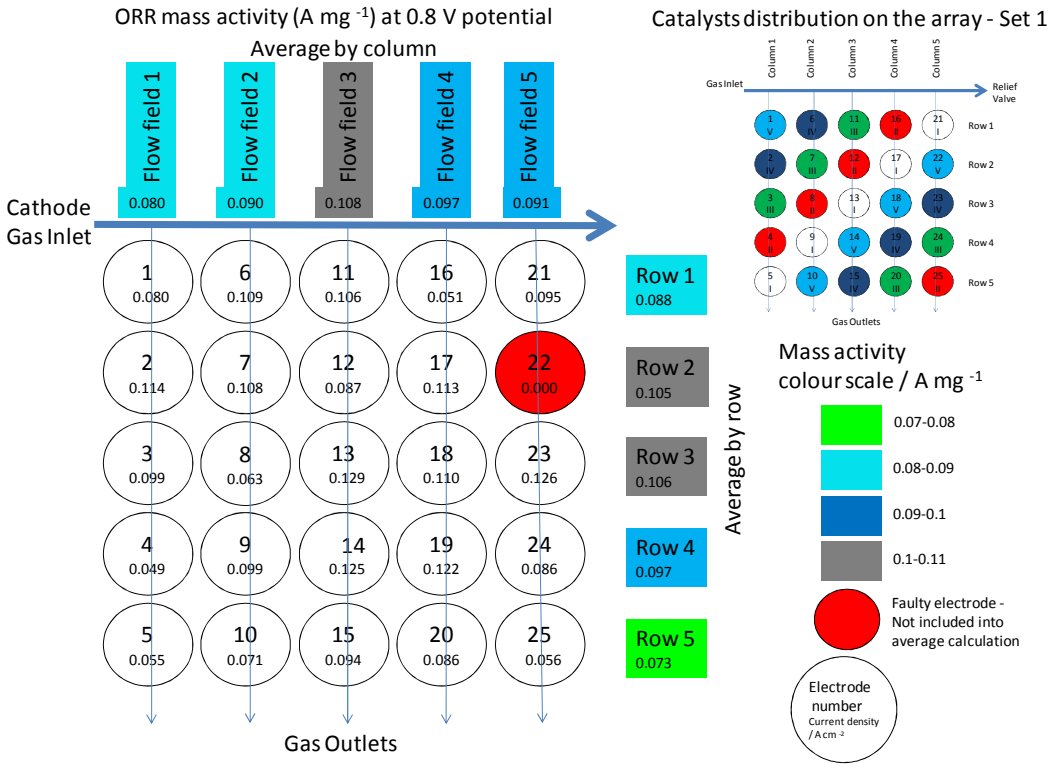

Figure 22 Schematic of the performance of the 5 catalysts in the 25 channel array. The mass activity (A mg^{-1}) measured at 0.8 V potential vs. DHE is given for each electrode.

Row switching polarisation curves were recorded and the current densities at 0.8 V were then converted to mass activities, based on the catalyst loadings. The results are depicted in Figure 23 and Figure 24. In Figure 24 the height of the column represents the mass activity for each electrode. Some variation in the performance of each catalyst type was observed,

depending on the row. However, the trends in activities are reported in each row. The average mass activity values acquired at 0.8 V vs. DHE for all five catalysts were calculated and are shown in Figure 24. The trend agrees well with ORR mass activity trends from experiments carried out at the Johnson Matthey Technology Centre (JMTC) by Sarah Ball using a 50 cm^2 single fuel cell.

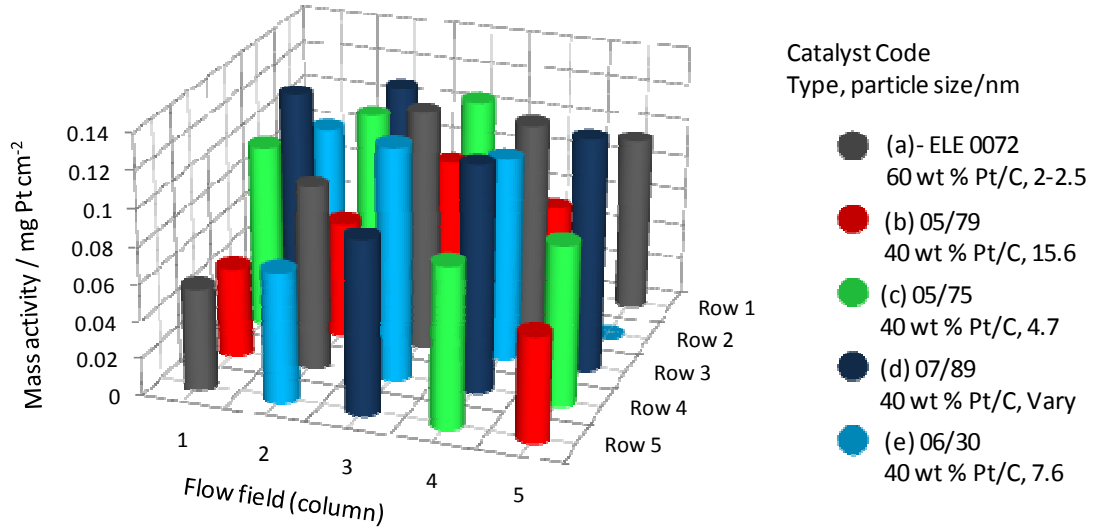

Figure 23 Mass activities at 0.8 V vs. DHE potential, for the 5 catalysts, as described in Table 1.

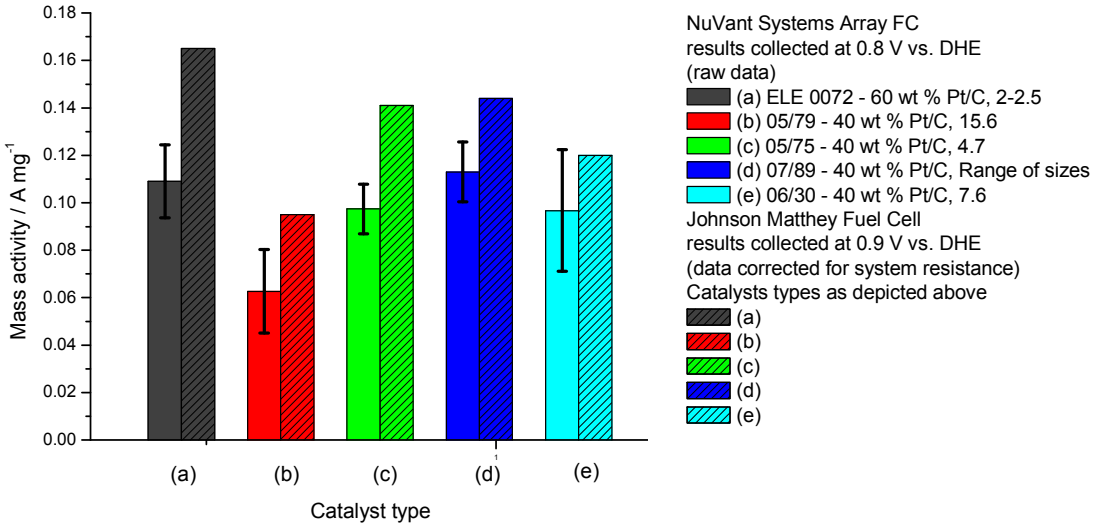

Figure 24 Comparison of the average mass activity for the five catalysts obtained using the array (no resistance correction) at 0.8 V vs. DHE and iR corrected fuel cell data supplied by JMTC at 0.9 V vs. RHE.

In agreement with the JMTC results, (c), (d) and (e) performed better than catalyst (b), but catalyst (a) does not show the expected increase in performance.

The average values for each row and column are shown in the rectangles at the top and side in Figure 22. This evaluation involves row and column averages. In theory, each row and column should have the same average mass activity, as each column and row have only one

catalyst of each type. In practice, as seen in Figure 22, the mass activities in the rows and columns are very similar; the only lower performance row seems to be Row 5, which has a slightly lower mass activity.

Considering that the system needs further development, the quality and reproducibility of the data at temperature of 80 °C conditions are satisfactory. However, the data that were acquired at a relatively low cell temperature (70 °C) did not display such reproducibility. Thus, operation at 80 °C is much more appropriate for catalyst testing and this temperature was used in all subsequent measurements.

4 Catalyst Screening - Qualitative agreement

A range of Pt catalysts was screened using the array fuel cell system during the period of this PhD. The electrode sheets were made and provided by the Johnson Matthey Technology Centre (JMTC). The electrodes were divided into groups of specific similarities and differences in their technical parameters such as different particle size, carbon types and Pt loading. Each of this set was tested at the same conditions of temperature, pressure and gas flow. Moreover, each group of electrodes contained a standard (ELE 0072 60 wt. % Pt/C) electrode to aid comparison. For ease of comparison, the reference/standard catalyst is named and positioned as (a) in each set of catalysts (see Table 1,Table 3 and Table 5). Each trend obtained for a particular set of catalysts was compared with the data acquired by Sarah Ball at JMTC using a single electrode fuel cell. This fuel cell with 50 cm^2 area was used as the main method to determine the properties of the catalysts.

The aim of the results presented here was to check and confirm the reproducibility of the array system in comparison to the standard fuel cell. This will be stressed throughout this section. The oxygen mass activities determined at JMTC with the standard cell for equivalent samples were measured at 80 °C, 100 % relative humidity, an O_2 stoichiometry of 10 and the data were corrected for membrane and system resistance [8, 34, 35] and Pt loading. In contrast, array cell data were not corrected for resistance as current interrupt measurements were not possible with the software available. The current interrupt method may help to obtain realistic gradients from Tafel plots. In consequence, only the trends may be compared.

4.1 Investigation of Pt surface area – particle size effect

One of the main parameters used to describe catalyst structure is the particle size. In each array experiment the MEAs were made of 25 working electrodes and were scanned many times to establish repeatability. As in previous chapters, the effects of particle size on the ORR activity were screened using two sets as defined in Table 1 (Set 1) and Table 3 (Set 2).

4.1.1 Particle size effect - Set 1

In this section, data collected using simultaneous and row switching modes are presented. These experimental results represent further analysis of the data shown in the reproducibility study described in section 3.2.2. Table 1 summarises the individual parameters of the samples tested: catalyst type, Pt loading, particle size (XRD results) and CO metal area.

This section focuses on the qualitative agreement and comparison with results obtained at JMTC using a standard fuel cell. Quantitative comparison is not possible, as the array cell data cannot be corrected for the effects of resistance. However, if we assume that the resistance effects are the same for all catalysts in the set, then the trend should match the reference data provided by Sarah Ball from JMTC.

After mass normalisation, the results for simultaneous and row switching modes shown in Figure 25 displayed similar trends. The catalyst (b) 05/79 with 15.6 nm particle diameter displayed the worst ORR activity amongst the catalysts examined for both array and fuel cell (JM) results. On the other hand, catalysts (c) 05/75 and (d) 07/89 show almost identical performance comparing results acquired using both array and fuel cell methods. Slightly lower ORR mass activities in contrast to those two catalysts were displayed by (e) 06/30 with 7.6 nm particle diameter. This situation occurred again for both methods and for both modes using the array.

As seen in Figure 25 , the trends obtained for all the experiments and reported here were consistent with the JM data in all cases except, unfortunately, for the standard catalyst which was worse than expected. Catalyst (a) ELE 0072 with Pt centres of 2-2.5 nm diameter was termed as our standard. Unfortunately this problem affects all the experiments performed using the 25 channel array cell. All the electrodes of this type were punched out of the same electrode sheet (38 x 26 cm) made at JM. The reason why the performance is different from the trend acquired at JM remains unexplained.

Some differences appeared between simultaneous and row switching mode experiments. For instance the average values from the row switching mode have much wider error bars. As previously noted in section 2.6.2, the scans using the row switching mode were carried out separately at three-hour intervals and the increased variation is attributed to differences in the humidification, temperature and pressure conditions that arose over such long time intervals.

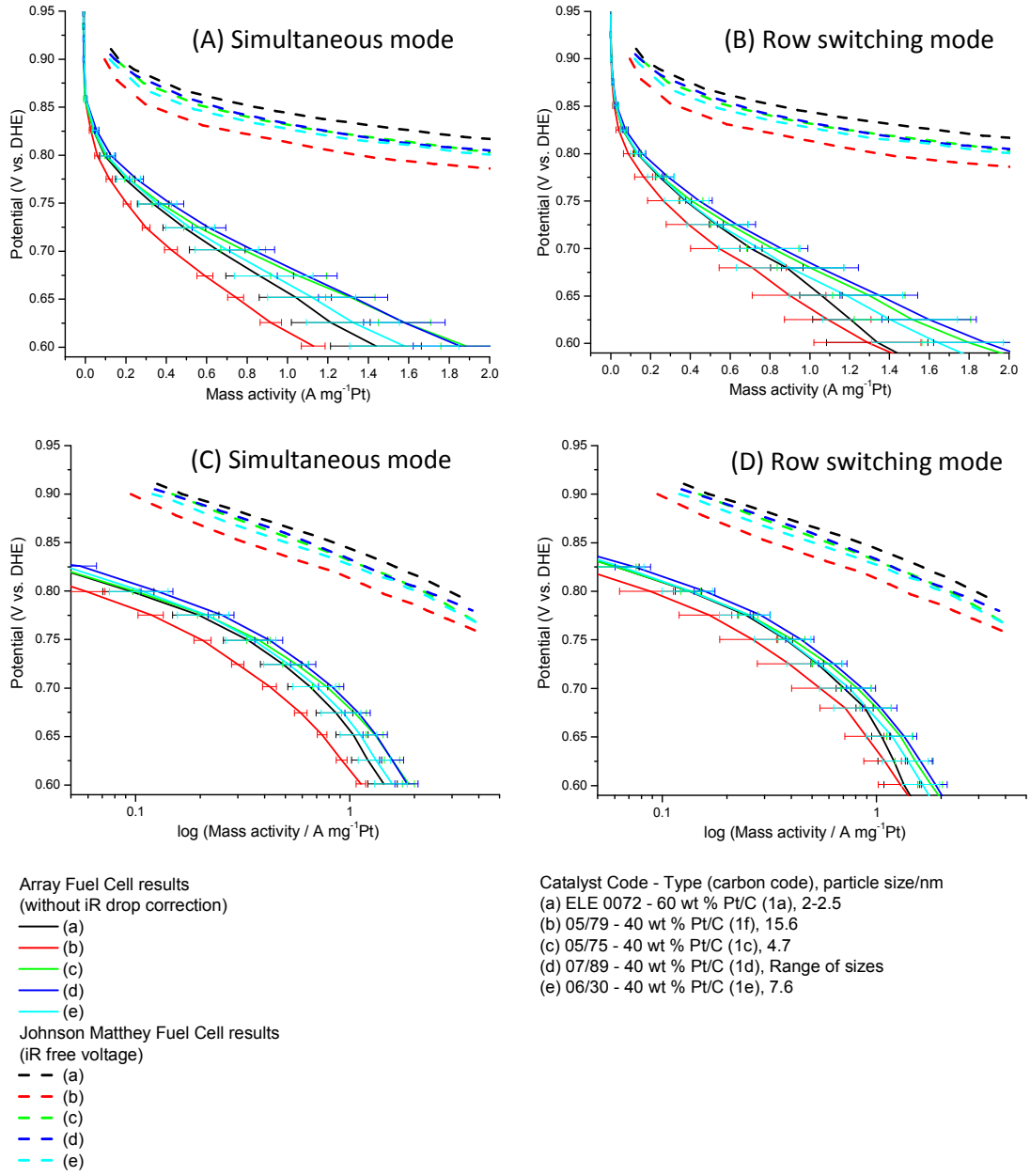

Figure 25 Comparison of two separate experiments carried out using simultaneous and row switching modes. Average array cell results (faulty electrodes were excluded) of five catalysts (Table 1) were plotted with data obtained at Johnson Matthey Technology Centre (JMTC). Average results were collected and presented as (A) Simultaneous mode - polarisation curves (B) Row switching mode - polarisation curves (C) Simultaneous mode - Tafel plots (D) Row switching mode - Tafel plots. Tafel plots were derived directly from polarisation curves where mass activities were altered to logarithmic scale. The experimental details are described in section 2.6.

The Tafel plots shown in Figure 25 (C) and (D) were obtained directly from the polarisation curves shown in Figure 25 (A) and (B), respectively. Detailed explanation of Tafel plot theory has been given elsewhere, in Chapter 2 section 3.3. JM results were corrected by cell and membrane resistance and displayed iR free voltage. For this reason, when mass activities were transformed into logarithm scale the curves form straight lines which agree well with the Tafel plot theory [36]. On the other hand, the array cell results (Figure 25 C

and D) do not show such behaviour in potential range presented here. This is connected with the lack of correction for resistance of the membrane and other system components. The array system does not yet possess a procedure for measuring the resistance. A straight/linear Tafel slope was only obtained for potentials ≥ 0.75 V. If the data could be corrected for system and membrane resistance, the curves should be straight over a more extensive potential range. Nevertheless, the trends observed for polarisation curves of both Figure 25 (A) and (B) stayed identical for Tafel plots as well as Figure 25 (C) and (D).

Table 2 is a demonstration of mass activities performance at 0.8 V, 0.75 V and 0.6 V. The values were extracted from the polarisation curves shown in Figure 25. For all the potentials and both collection modes identical trend of ORR mass activities was observed, decreasing in order (d) 07/89, range of sizes ≥ (c) 05/75, 4.7 nm > (e) 06/30, 7.6 nm ≥ (a) ELE 0072, 2-2.5 nm >> (b) 05/79, 15.6 nm particle diameter.

Table 2 Comparison of mass activities values extracted from polarisation curves shown in Figure 25 (A) and (B) obtained using array cell along with results obtained at Johnson Matthey TC. Simultaneous and row switching mode scans were run from 1.1 V to 0.6 V potential.

	JM Fuel Cell results	**Array fuel cell results**					
Catalyst	**Mass activity at 0.9 V**	**Mass activity at 0.8 V**		**Mass activity at 0.75 V**		**Mass activity at 0.65 V**	
	Standard scan / A mg^{-1}	**Simultaneous mode/A mg^{-1}**	**Row switching mode/ A mg^{-1}**	**Simultaneous mode/A mg^{-1}**	**Row switching mode/ A mg^{-1}**	**Simultaneous mode/A mg^{-1}**	**Row switching mode/ A mg^{-1}**
(a) ELE 0072	0.165	0.094 ± 0.023	0.133 ± 0.018	0.330 ± 0.079	0.378 ± 0.036	1.050 ± 0.178	1.059 ± 0.111
(b) 05/79	0.095	0.058 ± 0.013	0.088 ± 0.025	0.203 ± 0.018	0.266 ± 0.120	0.758 ± 0.034	0.904 ± 0.194
(c) 05/75	0.141	0.099 ± 0.005	0.133 ± 0.012	0.370 ± 0.048	0.408 ± 0.061	1.329 ± 0.121	1.301 ± 0.190
(d) 07/89	0.144	0.126 ± 0.022	0.160 ± 0.019	0.416 ± 0.063	0.447 ± 0.066	1.348 ± 0.173	1.355 ± 0.199
(e) 06/30	0.120	0.107 ± 0.033	0.133 ± 0.033	0.350 ± 0.096	0.385 ± 0.113	1.130 ± 0.220	1.186 ± 0.291

4.1.2 Particle size effect – Set 2

The second part of the investigation again involved samples with various sizes of Pt centres. Three out of five catalysts tested in this experiment were the same as in the previous part (see section 4.1.1). The description of the electrodes used in the experiment and their parameters is shown in Table 3. The old Arraystat (NUV 200) was used. This model does

not have many embedded helpful functions such as row switching mode and temperature controllers. However, in this case the controllers could be set externally. For this reason, all ORR polarisation curves were acquired simultaneously. The polarisation curves shown in Figure 26 are representative of two scans collected separately. The temperature, humidification and pressure conditions at which the scans were acquired were described in detail in section 2.6.1. Both simultaneous mode scans presented here were run from 0.6 V to 0.95 V. To check reproducibility, the second scan was run using the same MEA after a six-hour interval.

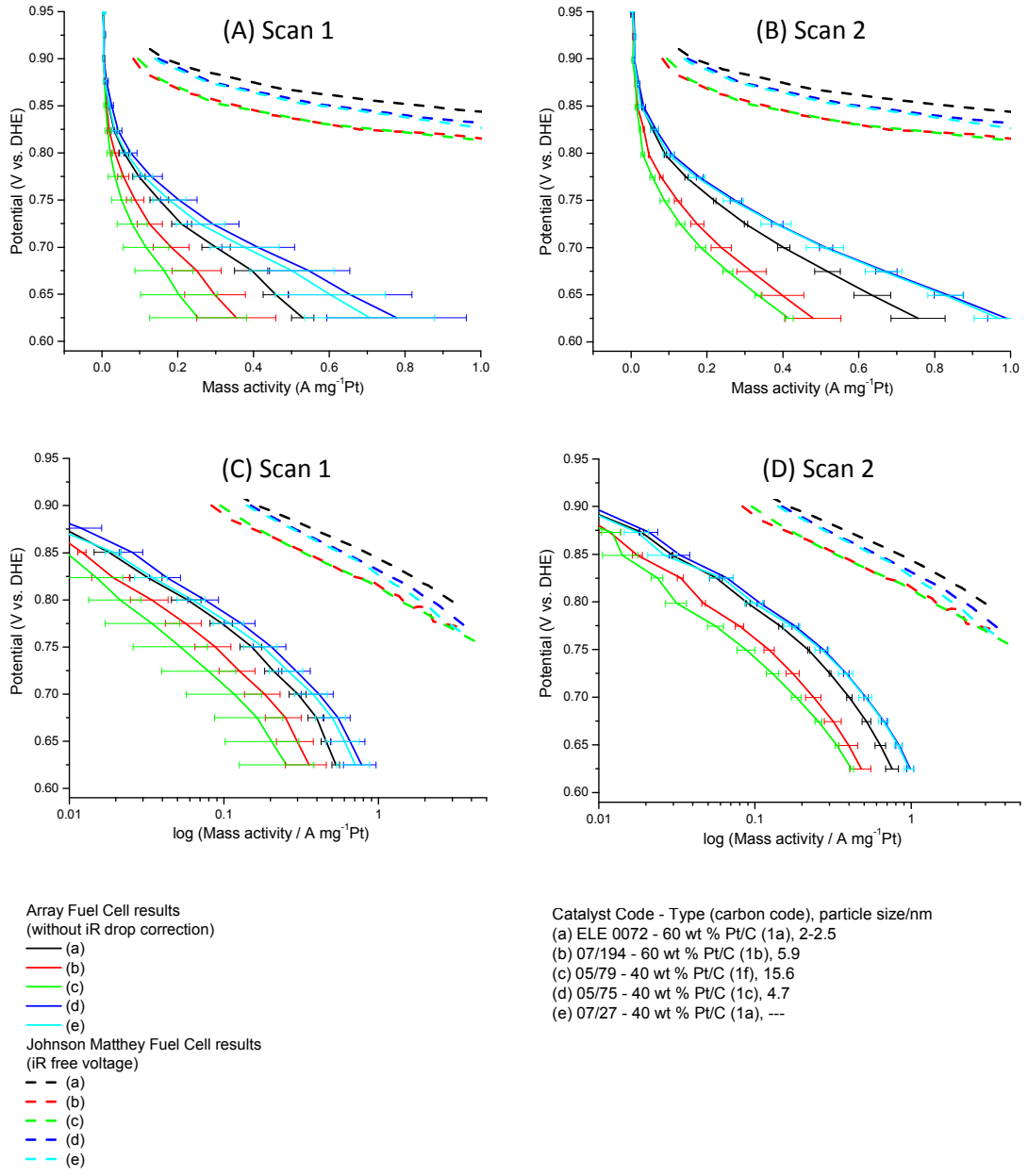

Figure 26 Comparison of array ORR average polarisation curves (without iR voltage correction) and Tafel plots with JM results for the same type of electrodes (iR free voltage). (A) Polarisation curves – Scan 1; (B) Polarisation curves – Scan 2; (C) Tafel plots – Scan 1; (D) Tafel plots – Scan 2. Both scans were carried out from 0.6 V to 0.95 V potential. Tafel plots for the 25 channel array and JM single cell results were extracted directly from polarisation curves.

Table 3 Description of the electrodes that were used in the experiment and their parameters.

Investigation of Pt surface area – particle size effect no.2					
Catalyst order	**Catalyst code**	**Catalyst type**	**Pt loading / mg_{Pt} cm^{-2}**	**Particle size (XRD results)**	**CO metal area / m^2 g^{-1}_{Pt}**
(a)	ELE 0072	60%Pt/C	0.457	2 – 2.5	78-100
(b)	07/194	60%Pt/ C	0.44	5.9	22
(c)	05/79	40%Pt/C	0.32	15.6	13
(d)	05/75	40%Pt/C	0.31	4.7	83
(e)	07/27	40%Pt/C	0.33	---	---

The polarisation curves and corresponding Tafel plots for both scans are shown in Figure 26. The data points represent the average mass activities of the 4 out of 5 electrodes of each catalyst type and the error bars show the standard deviation. The catalyst electrodes in flow field/column 5 were excluded as they presented very poor performance, which was attributed to effects usually from the position of the gas inlet on the anode side of the cell, as described previously. The trend in catalyst activity (c) 15.6 nm < (b) 5.9 nm << (a) 2-2.5 nm < (d) 4.7 ≈ (e) are the same in both scans. However, there is a slight improvement in mass activity for all the catalyst in scan 2 over that observed in scan 1. Such an improvement is commonly observed when testing PEM fuel cell MEAs and is usually attributed to improved utilisation and decreased resistance as the membrane and catalyst layer 'wet up' during operation.

Whilst the absolute mass activities obtained using the array cell are much lower than the fuel cell data provided by S. Ball (attributed to lack of IR correction, differences in humidification and the lack of application of any back pressure to the system), the trends in activity are consistent, with the exception of the reference catalyst (black curves). As mentioned previously, this catalyst underperformed in all the studies performed/described in this chapter.

Mass activities at 0.8 V, 0.75 V and 0.6 V are presented in Table 4. The values were extracted from the polarisation curves shown in Figure 26. Only at the higher potential of 0.8 V do the mass activity values have similar performance in both scans. However, identical trends are observed for all the catalysts. Johnson Matthey fuel cell results obtained at 0.9 V were set in Table 4 for comparison purposes.

Table 4 Comparison of mass activities values extracted from polarisation curves shown in Figure 26 (A) and (B) obtained using array cell along with results obtained at Johnson Matthey TC. Both scans were acquired using Simultaneous mode and were run from 0.6 V to 0.95 V potential.

	JM Fuel Cell results	**Array fuel cell results - Simultaneous mode**					
Catalyst	**Mass activity at 0.9 V**	**Mass activity at 0.8 V**		**Mass activity at 0.75 V**		**Mass activity at 0.65 V**	
	Standard scan / A mg^{-1}	**Scan 1 /A mg^{-1}**	**Scan 2 / A mg^{-1}**	**Scan 1 /A mg^{-1}**	**Scan 2 / A mg^{-1}**	**Scan 1 /A mg^{-1}**	**Scan 2 / A mg^{-1}**
(a) ELE 0072	0.165	0.058 ± 0.013	0.090 ± 0.003	0.151 ± 0.025	0.220 ± 0.003	0.460 ± 0.035	0.635 ± 0.050
(b) 07/194	0.083	0.034 ± 0.010	0.046 ± 0.001	0.088 ± 0.018	0.124 ± 0.011	0.298 ± 0.078	0.400 ± 0.057
(c) 05/79	0.095	0.021 ± 0.008	0.031 ± 0.005	0.052 ± 0.026	0.088 ± 0.011	0.203 ± 0.105	0.334 ± 0.010
(d) 05/75	0.141	0.075 ± 0.016	0.108 ± 0.006	0.203 ± 0.048	0.275 ± 0.013	0.655 ± 0.163	0.840 ± 0.040
(e) 07/27	0.141	0.063 ± 0.014	0.099 ± 0.014	0.177 ± 0.044	0.269 ± 0.027	0.602 ± 0.143	0.828 ± 0.048

4.2 Investigation of Pt utilisation

The effects of catalyst utilisation were investigated by screening a set of 60 wt. % Pt/C catalysts with different catalyst layer thicknesses or loadings. If full utilisation of the catalysts is made throughout the measurements, identical mass activity polarisation curves should be obtained for all the electrodes in this set.

Table 5 Detailed descriptions of the catalysts used in the experiment depicted below.

Investigation of Pt loading					
Catalyst order	**Catalyst code**	**Catalyst type**	**Pt loading / mg_{Pt} cm^{-2}**	**Particle size (XRD results)**	**CO metal area / m^2 g^{-1}_{Pt}**
(a)	ELE 0072	60%Pt/C	0.457	2 – 2.5	78-100
(b)	ELE 0034	60%Pt/ C	0.39	2 – 2.5	---
(c)	ELE 0065	60%Pt/ C	0.2	2 – 2.5	---
(d)	Production 1	60%Pt/ C	0.34	2 – 2.5	---
(e)	Production 2	60%Pt/ C	0.4	2 – 2.5	---

The details of the catalysts in this set are given in Table 5. Two simultaneous collection scans were run. The mass activity polarisation curves and corresponding Tafel plots are shown in Figure 27. The two scans were run in opposite directions: Figure 27A was obtained from 1.0 V to 0.6 V, while Figure 27 B from 0.6 V to 1.0 V, both using 25 mV step and a 60

second hold interval. The mass activity trends are identical for both scans, with the second scan giving consistently higher values of mass activity (Table 6) than the first, especially in the kinetic region. The two scans were run one after another; the increased activity for the second scan is attributed to improved utilisation and reduced resistance following the wetting of the catalyst layer that is a result of water production at the cathode, which is a product of the ORR reaction.

For both simultaneous experiments at 0.8 V potential, the best performance was obtained for electrodes made of catalyst (c), which is the electrode with the lowest Pt loading of 0.2 mg cm^{-2}, and the worst performance was obtained with catalyst (a), 0.457 mg cm^{-2}. In the kinetically controlled region of the polarisation curves, $E \leq 0.8$ V, the differences in mass activities are within the error/standard deviations of the data points. It is only when mass transport effects become significant that the differences lie outside the error bars in Figure 27. Thus, although the potential range and mass activity range over which kinetic control is maintained are restricted, we are able to conclude that catalyst utilisation is not a significant barrier to ranking cathode catalyst activities for catalysts of the type investigated in this thesis.

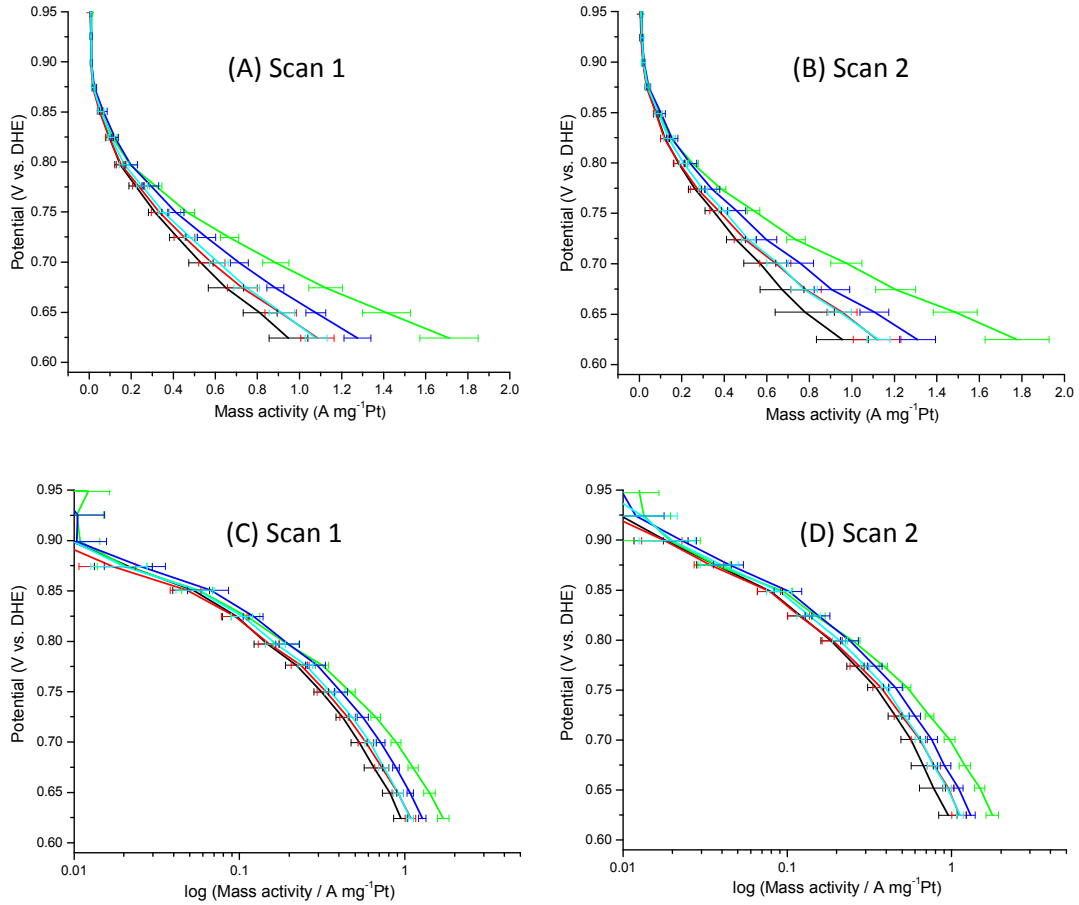

Figure 27 Comparison of two ORR average polarisation curves acquired using array cell (without iR voltage correction) and Tafel plots. Simultaneous experiments: (A) Polarisation curves – Scan 1; (B) Polarisation curves – Scan 2; (C) Tafel plots – Scan 1; (D) Tafel plots – Scan 2. Scan 1 was carried out from 1.0 V to 0.6 V potential (forward scan). Scan 2 was run from 0.6 V to 1.0 V potential (reverse scan). Tafel plots for the 25 channel array were extracted directly from polarisation curves. The mass activities values were converted into logarithm scale. The experimental details are described in section 2.6.1.

Table 6 Comparison of mass activity values extracted from polarisation curves shown in Figure 27 (A) and (B). Scan 1 was carried out from 1.0 V to 0.6 V potential (forward scan) and Scan 2 in opposite direction 0.6 V to 1.0 V potential (reverse scan).

Catalyst	Mass activity at 0.8 V Simultaneous mode		Mass activity at 0.75 V Simultaneous mode		Mass activity at 0.65 V Simultaneous mode	
	Scan 1/A mg^{-1}	Scan 2/A mg^{-1}	Scan 1/A mg^{-1}	Scan 2/A mg^{-1}	Scan 1/A mg^{-1}	Scan 2/A mg^{-1}
(a) ELE 0072	0.142 ± 0.026	0.184 ± 0.024	0.312 ± 0.033	0.357 ± 0.055	0.806 ± 0.084	0.790 ± 0.142
(b) ELE 0034	0.146 ± 0.021	0.188 ± 0.031	0.332 ± 0.041	0.385 ± 0.043	0.907 ± 0.082	0.965 ± 0.077
(c) ELE 0065	0.186 ± 0.034	0.250 ± 0.023	0.466 ± 0.040	0.556 ± 0.040	1.410 ± 0.113	1.507 ± 0.040
(d) Production 1	0.191 ± 0.033	0.239 ± 0.032	0.410 ± 0.043	0.470 ± 0.046	1.072 ± 0.045	1.122 ± 0.072
(e) Production 2	0.160 ± 0.022	0.208 ± 0.034	0.354 ± 0.030	0.408 ± 0.022	0.913 ± 0.066	0.954 ± 0.062

In summary, the results obtained were in almost perfect agreement between the two experiments run using the same MEA. All the potential range ORR specific activity performances were established in order (c)>>(d)>(e)=(b)>(a). A narrow range of error bars, fully reproducible trends, and the same magnitude of currents suggested that the data from this investigation were of very high quality.

5 Conclusions and Recommendations

From the information and results gathered in this chapter, several conclusions and recommendations can be made regarding system development, reproducibility and qualitative agreement. At the moment, the array fuel cell system is undergoing intensive development. Pleasingly, for each of the catalyst sets tested, the trends in mass activities obtained were the same as those derived from fuel cell tests, with the notable exception of the control catalysts.

In general, better results were obtained using the simultaneous collection mode and following conditions of the catalyst electrodes either by running multiple scans or by simply starting at 0.6 V rather than 1.0 V. The latter was attributed to improved catalyst utilisation and decreased resistance and is a known effect observed in fuel cell testing. Quantitative agreement with the fuel cell data was not obtained, which limits the references of the data. Achieving such agreement refers to: (i) development of procedures for measurement of the resistances in the array cell, for example using the current interrupt technique used for fuel cell testing; (ii) improvements in temperature and humidification control; and (iii) control and application of back pressure to the cell.

The decision to use a parallel flow field in the work presented in this thesis was based on earlier unsuccessful ORR tests performed at NuVant system using serpentine flow field [1-

4]. Several other designs are possible, but time restrictions prevented their exploration during this project. In retrospect, an interdigitated design, in which the gas flow is forced to travel across the catalyst layer may have proved to yield better results and should be explored in any work that follows on from this thesis.

In addition to improvements in the design of the cell and humidifiers, improvements in the Arraystat potentiostat would be beneficial. Specifically, the inclusion of lower current ranges would enable collection of cyclic voltammograms for each of the catalyst electrodes in the cell, while access to higher current ranges may be required to cope with the increased currents that may accompany the improved cell design. Collection of the CVs will enable the active catalyst area of each electrode to be determined from either the CO or H adsorption areas. Such data will facilitate comparison with either the RDE data presented in Chapter 3 or the 64 channel wet cell data presented in Chapter 4.

Finally, improvements in and automation of the data analysis would dramatically affect the throughput of the measurements using an array fuel cell.

6 References

1. E. S. Smotkin, J. H. Jiang, A. Nayar, and R. X. Liu, Applied Surface Science 252:2573 (2006).
2. R. Liu and E. S. Smotkin, Journal of Electroanalytical Chemistry 535:49 (2002).
3. R. R. Diaz-Morales, R. X. Liu, E. Fachini, G. Y. Chen, C. U. Segre, A. Martinez, C. Cabrera, and E. S. Smotkin, Journal of the Electrochemical Society 151:A1314 (2004).
4. E. S. Smotkin and R. R. Diaz-Morales, Annual Review of Materials Research 33:557 (2003).
5. B. C. Chan, R. X. Liu, K. Jambunathan, H. Zhang, G. Y. Chen, T. E. Mallouk, and E. S. Smotkin, Journal of the Electrochemical Society 152:A594 (2005).
6. H. Li, Y. Tang, Z. Wang, Z. Shi, S. Wu, D. Song, J. Zhang, K. Fatih, J. Zhang, H. Wang, Z. Liu, R. Abouatallah, and A. Mazza, Journal of Power Sources 178:103 (2008).
7. J. Soler, E. Hontañón, and L. Daza, Journal of Power Sources 118:172 (2003).
8. Handbook of Fuel Cells. Fundamentals Technology and Applications, John Wiley & Sons Ltd., 2003.
9. A. D. Larminie, Fuel Cell Systems Explained, John Wiley & Sons, 2003.
10. L. Xianguo, Principles Of Fuel Cells, Taylor, 2005
11. S. J. Lee, S. Mukerjee, J. McBreen, Y. W. Rho, Y. T. Kho, and T. H. Lee, Electrochimica Acta 43:3693 (1998).
12. S. Banerjee and D. E. Curtin, Journal of Fluorine Chemistry 125:1211 (2004).
13. M. N. Tsampas, A. Pikos, S. Brosda, A. Katsaounis, and C. G. Vayenas, Electrochimica Acta 51:2743 (2006).
14. P. D. Beattie, V. I. Basura, and S. Holdcroft, Journal of Electroanalytical Chemistry 468:180 (1999).
15. D. Aaron, S. Yiacoumi, and C. Tsouris, Separation Science and Technology 43:2307 (2008).
16. A. Bazylak, D. Sinton, Z. S. Liu, and N. Djilali, Journal of Power Sources 163:784 (2007).
17. I. Nitta, T. Hottinen, O. Himanen, and M. Mikkola, Journal of Power Sources 171:26 (2007).
18. W.-k. Lee, C.-H. Ho, J. W. Van Zee, and M. Murthy, Journal of Power Sources 84:45 (1999).
19. J. Ge, A. Higier, and H. Liu, Journal of Power Sources 159:922 (2006).

20. A. Kraytsberg and Y. Ein-Eli, Journal of Power Sources 160:194 (2006).
21. X. Liu, H. Guo, and C. Ma, Journal of Power Sources 156:267 (2006).
22. K. Karan, H. Atiyeh, A. Phoenix, E. Halliop, J. Pharoah, and B. Peppley, Electrochemical and Solid State Letters 10:B34 (2007).
23. M. V. Williams, H. R. Kunz, and J. M. Fenton, Journal of Power Sources 135:122 (2004).
24. S. C. Ball, S. L. Hudson, B. R. C. Theobald, and D. Thompsett, ECS Transactions 11:1267 (2007).
25. S. C. Ball, S. L. Hudson, J. H. Leung, A. E. Russell, D. Thompsett, and B. R. C. Theobald, ECS Transactions 11:1247 (2007).
26. P. J. Ferreira, G. J. la O, Y. Shao-Horn, D. Morgan, R. Makharia, S. Kocha, and H. A. Gasteiger, Journal of the Electrochemical Society 152:A2256 (2005).
27. S. C. Ball, S. L. Hudson, D. Thompsett, and B. Theobald, Journal of Power Sources 171:18 (2007).
28. S. Ball, S. Hudson, B. Theobald, and D. Thompsett, ECS Transactions 3:595 (2006).
29. K. Kinoshita, Journal of the Electrochemical Society 137:845 (1990).
30. S. Mukerjee and J. McBreen, Journal of Electroanalytical Chemistry 448:163 (1998).
31. T. J. Schmidt, H. A. Gasteiger, G. D. Stab, P. M. Urban, D. M. Kolb, and R. J. Behm, Journal of the Electrochemical Society 145:2354 (1998).
32. J. J. Wang, G. P. Yin, Y. Y. Shao, S. Zhang, Z. B. Wang, and Y. Z. Gao, Journal of Power Sources 171:331 (2007).
33. D. A. Stevens, M. T. Hicks, G. M. Haugen, and J. R. Dahn, Journal of the Electrochemical Society 152:A2309 (2005).
34. K. C. Neyerlin, H. A. Gasteiger, C. K. Mittelsteadt, J. Jorne, and W. B. Gu, Journal of the Electrochemical Society 152:A1073 (2005).
35. K. C. Neyerlin, W. B. Gu, J. Jorne, and H. A. Gasteiger, Journal of the Electrochemical Society 153:A1955 (2006).
36. D. Pletcher, Instrumental Methods in Electrochemistry, Horwood Publishing, Southampton, 2001.
37. H. A. Gasteiger, J. E. Panels, and S. G. Yan, Journal of Power Sources 127:162 (2004).

Contents

Chapter Six: Conclusions and Future Directions

The kinetics of the ORR need to be improved before PEMFCs can be used widely as energy conversion devices in commercial applications. Enhancement can come from the discovery of inherently more active catalysts. Screening libraries of new formulations requires the development of methods that help to establish the real properties of the catalysts. At the moment, only a few methods of catalyst testing are deemed 'reliable'. Examples are the thin film RDE and standard fuel cell methods. Unfortunately, these systems have weaknesses: the number of samples tested is limited by time and the essential work force required. Thus, fewer catalysts can be tested in a short period of time due to the single channel nature of such measurements.

The principal aim of this project was to develop and benchmark high-throughput screening methods for ORR testing. The first method for rapid catalyst scanning was a 64-channel array developed initially by Guerin et al. [1, 2]. The second system developed during the period of this PhD was a parallel flow field array fuel cell. This method was based on a similar design with a serpentine flow field, which was used as a direct methanol array fuel cell by Smotkin et al. [3-6]. The advantage is the ability to scan a large number of samples simultaneously and in the same environment. The results from these two methods were compared to the 'reliable' rotating disc electrode method [7-15].

The description of the 64-channel array system development was given and results were shown in Chapter 4. Similarly, all the array fuel cell system features, enhancements and data obtained were described in Chapter 5. RDE single channel system results collected for the same type of catalysts as the 64-channel array were presented in Chapter 3. However, no enhancements in the system design for the RDE testing were made. Chapter 6 is an in-depth comparison of the three systems depicted in Chapters 3, 4 and 5.

1 Comparison of system components

First, the components and specifications of the test systems can be compared. Table 1 summarises all the similarities and differences in design and environmental conditions during experiments.

Table 1 Comparison of RDE, 64 channel Array and Array Fuel Cell system components and specifications.

	RDE	64 channel Array	Array Fuel Cell
Number of working electrodes	1	64 (8x8)	25 (5x5)
Working electrode, diameter, area	Glassy carbon 5 mm ø diameter, 0.196 cm^2 area,	Glassy carbon 5 mm ø diameter, 0.196 cm^2 area	Graphite sensor flow field 9.5 mm ø diameter, 0.713 cm^2 area
Reference electrode	MMS (mercury mercurous sulphate) calibrated to RHE (reversible hydrogen electrode) scale	MMS calibrated to RHE scale	Common counter/reference electrode– anode serving as DHE with 103 cm^2 area, 60 wt. % Pt/C, 0.4 mg_{Pt} cm^{-2}, feed with H_2 at 80 cm^3 min^{-1}.
Counter electrode	Pt gauze positioned perpendicular to working electrode	Pt gauze positioned above array of working electrodes	Same as reference electrode
Cell materials	Glass (Chapter 3 Figure 2)	Teflon parts (Cell top, base array plate, bottom plate), glassy carbon working electrode (Chapter 4 Figures 2 and 3)	Aluminium, garolite, graphite working and counter/reference electrode (Chapter 5 Figures 2 and 3)
Potentiostat and system components	Autolab PGSTAT30, PINE AFMSRX Modulated Speed Rotator, exchangeable disc system, Pine instrument rotation rate control unit.	64 channel potentiostat , [1] triangular Waveform Generator (PP RI HI-TEK INSTRUMENTS ENGLAND), current follower 1 mA V^{-1} (max. 10 V)	Arraystat (potential range ± 10 Volts with resolution 3 mV, total current range over 13.5 Amp) with imbedded 5 temperature controllers and current follower
Hardware requirements	PC connected with Autolab interface	PC (Pentium 4, 2.6 GHz, with XP professional operating system), PCI-DAS6402/16 data acquisition card	PC embedded PCI-6229, NI-DAQmx card
Software	Autolab software – GPES 4.9 version	The acquisition wizard and The analyser (Visual Basic based software)	NuVant CASE V2.0 (Lab View based software)
Purging system	One glass tube	Four glass tubes with sinter	Gas flow regulate by mass flow controllers and orifices valves (MEA)
Environment	1 mol dm^{-2} H_2SO_4	0.5 mol dm^{-2} H_2SO_4	MEA (Nafion 117 membrane)
Gases used	O_2, N_2, H_2, CO	O_2, N_2, H_2, CO	O_2, N_2, H_2, CO
Heating system	Water jacket - thermostatically controlled water bath (Grant)	Not regulated	Four heating cartridges, heating lines, heating humidifiers
Temperature	Room or elevated temperature up to 80 °C	room temperature	80 °C – cell, 90 °C – anode humidifier, 40 °C – cathode humidifier
Pressure	Atmospheric	Atmospheric	80 psi - cathode, 100 - psi anode
Flow rate	Unknown (not important if the solution is saturated)	Unknown (not important as long as the solution is saturated)	80 ml min^{-1} cathode, 100 ml min^{-1} anode
Mass transfer control	Rotating electrode – controlled by convection and diffusion forces	No mass transfer control – bubbling gas through solution	Regulate gas flow rate using orifice valves – cathode and mass flow controllers - anode
Electrode cleaning	Polished manually using alumina powder (Buehler, grain sizes of 1, 0.3, 0.05 μm)	98 % ethanol or iso-propanol using cotton-wool, distilled water (16-18 MΩ cm), alumina powders with three particle sizes (0.3, 0.1 and 0.05 μm)	Clean using iso-propanol, methanol and air flux
Complexity of the system	Low	Low	High

The RDE is a single channel system consisting of a rotating electrode which forces the solution towards the electrode surface. This is a unique system amongst methods of measurement in electrochemistry because mass transfer is controlled. On the other hand, the main weaknesses of the RDE are the time each measurement takes and the need for a highly skilled work force. Hence, multichannel methods, such as the 64-channel array and array fuel cell, are better solutions in matters of time and cost. 64-array electrodes do not rotate and are firmly embedded and glued into the PTFE bottom plate. In this case, mass transfer cannot be controlled because of the cell design. Fortunately, the kinetic region of each polarisation curve is independent of mass transfer, and therefore the kinetics of ORR could be measured reproducibly. The array fuel cell also suffers from a lack of mass transfer control, but is a more realistic mimic of the performance in the real MEA environment of a PEMFC.

In the matter of time consumption during measurement, RDE needs an entire month to acquire the same quantity of data as array systems can collect in one day. Additionally, considering the fact that ambient temperature and ambient pressure conditions could fluctuate rapidly over the period of a month, these factors can play a role in experimental error for RDE. On the other hand, the same conditions exist especially in a 64-channel array cell liquid environment with an 8 x 8 electrode library. As long as the electrolyte is saturated with gas, it does not matter where the electrode is positioned in the cell. The array fuel cell system with a 5 x 5 electrode library operates with a gaseous feed of O_2, which is more difficult to control uniformly over the entire cell as the cell could be partially flooded with water delivered from ORR and humidification. Hence, the conditions could change slightly for specific regions in the cell and differences in performance were found to occur in between rows and/or columns.

2 Results

The most important information, which determines which of the three methods is the best, is the reliability and reproducibility of the results. Moreover, the strengths and weaknesses associated with all three methods will be highlighted in this part. All the details concerning the results obtained in this project are described in Table 2.

First of all, only the array fuel cell did not possess an accurate method of Pt real surface area calculation, which is used to obtain electrochemical area (ECA). On the other hand, this method ensures precise estimation of Pt real loading (mg cm^{-2}). Conversely, both RDE and 64-channel array methods were able to obtain Pt real surface area but had difficulties with Pt

real loading estimation, as a very low mass of catalyst was deposited onto the glassy carbon electrodes (typically ≤ 80 μg for 64 channel array and ≤ 10 μg for RDE). The real mass in a drop pipetted onto the electrode appeared to vary by a factor of up to 7x (based upon variations observed in the ECA).

The methods of ink and electrode preparation, which were used mainly in the experiments performed during this PhD, and presented in this thesis were described in chapter 3 section 2.4. for the RDE and in chapter 4 section 2.4.2.1 for the 64 channel array. Different solvents were used in each case to disperse the Pt based catalysts. In addition different ratios of Nafion polymer to catalyst were used in preparation of the electrodes. Normally, the Nafion content for the RDE was only 25 % of that used for the 64 channel array. Moreover, much less catalyst was deposited onto the RDE vitrous carbon electrode, as depicted in the previous paragraph. In the case of the RDE, Nafion polymer was mixed with iso-propanol solution and was pipetted onto already deposited and dried catalyst layer, whilst for the 64 channel array electrode the Nafion was in the ink. The methods of ink and electrode preparation used here were inherited from previous researchers and empirically enhanced to fit the standards of the methods. The methods selected gave the best results of these explained. The investigation of the best electrode preparation methodology for 64 channel pin array was described in chapter 4 section 3(Reproducibility). The volume of Nafion polymer in low weight alcohol solution was set to 50 μL in both cases. It was concluded that too high a volume of Nafion solution significantly affected the diffusion of oxygen species to active sites of the catalyst and contributed to the ohmic losses described in chapter 2 section 3.3.2.

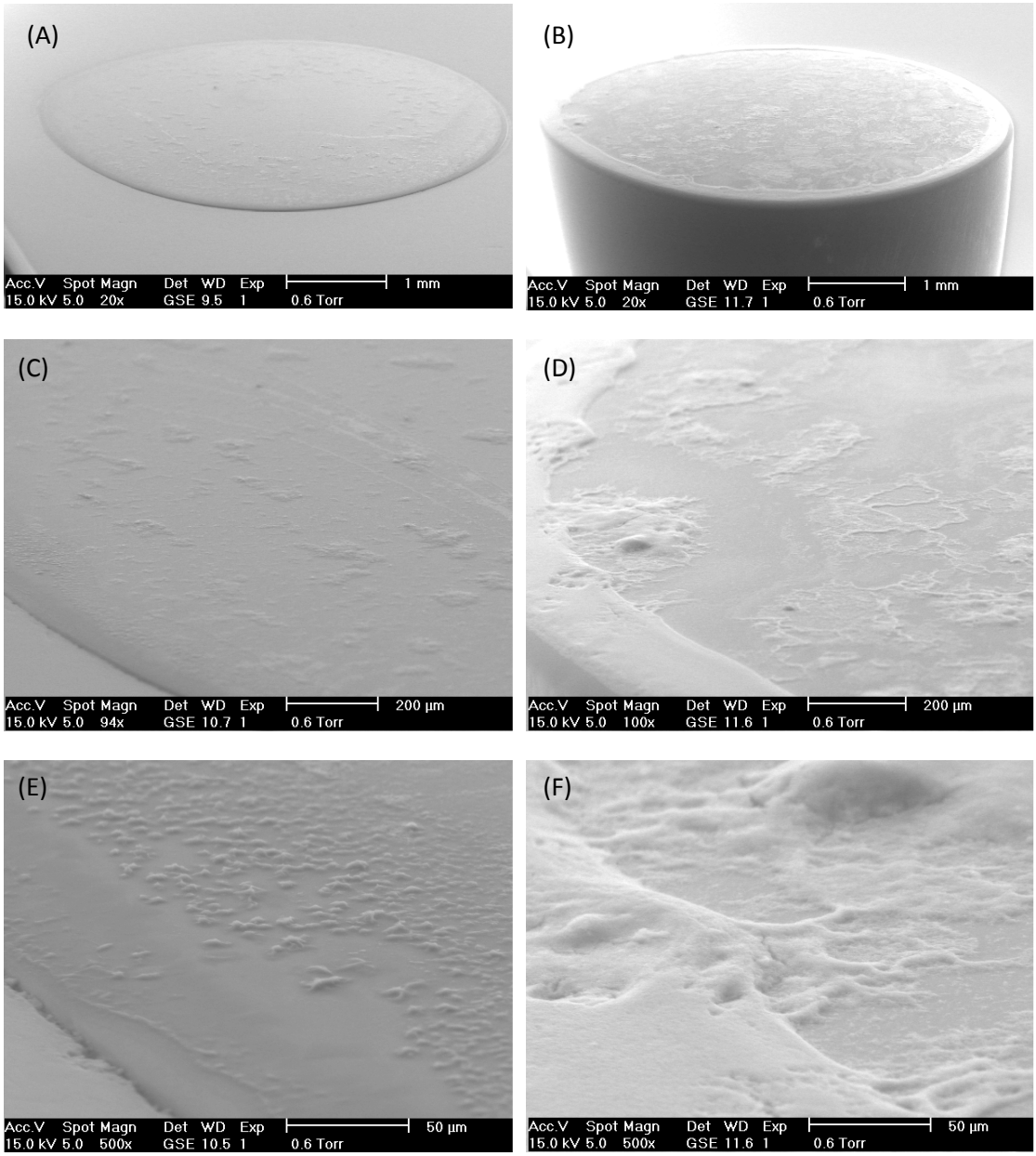

Figure 1 Scanning electron microscopy (SEM) images of RDE (A) x20 magnification with 1mm scale (C) x94 with 200 µm (E) x500 with 50 µm and 64 channel array electrode system (one chosen electrode) (B) x20 with 1mm (D) x94 with 200 µm (F) x500 with 50 µm. The pressure conditions were set at 0.6 Torr and the angle between the surface and the camera focus was set to 22.5 °.

Figure 1 shows a comparison of the surfaces roughness between RDE and 64 channel high throughput electrode using scanning electron microscopy (SEM). The images were collected in three different magnifications, x20 (Figure 1A and B), x94 (Figure 1C and D), x500 (Figure 1E and F), respectively. It is clearly seen from Figure 1 that more catalyst was deposited on the 64 channel electrode (Figure 1A, C and E) than on the RDE electrode (Figure 1B, D and F). Hence the roughness is significantly larger in comparison to the RDE electrode surface and this roughness is expected to vary significantly as the mass of catalyst

deposited each time could not be precisely controlled. All the SEM images were obtained by Ahmet Celiktas, University of Southampton.

The best reproducibility for cyclic voltammograms was acquired for the 64-channel array system. The second in order of quality was the CV collected for the RDE method. The lower quality of the RDE data could be explained by the fact that the CVs were obtained over a longer time interval. The worst quality CVs were obtained using the array fuel cell equipment. However, the origin of the problem with the array fuel cell derives from a different issue than the RDE data, in that the current follower in the potentiostat was not sensitive enough for the much lower currents observed in CV experiments, having been designed for polarisation studies.

Normally after cyclic voltammetry experiments, ORR polarisation curves tests are run. The best reproducibility was obtained for the 64-channel array followed by the array fuel cell. Definitely the worst data quality was obtained using the RDE method. Sometimes only two out of four experiments were reproducible.

The electrodes tested using RDE had the lowest Pt loading of 5-10 μg cm^{-2}. The 64-channel technique examined electrodes with a range of 40-80 μg cm^{-2} Pt loading. The only system which approached the Pt loading on the electrodes used in real fuel cell systems was the array fuel cell, 0.2-0.47 mg cm^{-2}. This is a huge advantage of this method because one can observe more accurately how catalysts behave in real fuel cell conditions with realistic loadings.

Table 2 Comparison of experimental parameters and results obtained.

	RDE	64 channel Array	Array Fuel Cell
Pt real surface area calculation / cm_{Pt}^2	yes	yes	no
Pt real mass estimation / mg_{Pt}	no	no	yes
Specific activity / A cm_{Pt}^{-2}	yes	yes	no
Mass activity / A mg_{Pt}	no	no	yes
Calculation of ECA (electrochemical area) / $m_{Pt}^2\ g_{Pt}^{-1}$	no	no	no
Reproducibility and quality of CV	good	very good	very poor
Reproducibility and quality of polarisation curves in ORR	poor	good	good
Qualitative agreement	The catalyst ORR performance trends agreed with 64 channel results	The catalyst ORR performance trends agreed with RDE results	The catalyst ORR performance trends agreed with fuel cell (50 cm^2 area) data supplied by S. Ball (JMTC)
Ink solvent	Chloroform based ink, Water:iso-propanol based ink	Water based ink	(MEA)
Experimental Pt loading / mg cm^{-2}	0.005 – 0.01	0.04 – 0.08	0.2 – 0.47
Procedure - CV acquisition method	Limits: 0.05 V-1.2 V, Scan rate: 10 mV s^{-1}	Limits: 0.05 V-1.2 V, Scan rate: 20 mV s^{-1}	Limits: 0.05 V-1.2 V, Scan rate: 50 or 100 mV s^{-1}
Procedure - Polarisation curve acquisition method	- ORR experiment at rotation speeds: 900, 1600, 2500 and 3600 rpm Limits: 0.05 V-1 V, Scan rate: 2 mV s^{-1}	- ORR experiment all 64 electrodes tested simultaneously Limits: 0.7 V-1.1 V, Potential Step: 25 mV, Step interval: 60 s	- ORR experiment Simultaneous mode - 25 electrodes tested Row switching mode - 5 electrodes tested simultaneously Limits: 0.6 V-0.95 V, Potential Step: 25 mV, Step interval: 60 s
Kinetic region range	0.75 V – 1.0 V	0.9 V – 1.0 V	0.75 V – 0.9 V (without iR correction)
Time of experiment	Half a day	One day	Two - Three days
Data processing time (depends on experience)	Two hours	Two days	One day

The procedure for the cyclic voltammetry experiment was identical for all three systems; the potential was scanned between 0.05 V and 1.2 V. However, the scan rates were different, 10 and 20, 50-100 mV s^{-1} for RDE, 64-channel array and array fuel cell respectively. The

ORR investigations were carried out slightly differently for the RDE method. Four cyclic voltammetry scans were carried out between 0.05 and 1.0 V limits at different rotation speeds (900, 1600, 2500 and 3600 rpm) with 2 mV s^{-1} scan rate. In comparison, both arrays' polarisation curves were acquired at 25 mV potential step with 60 second intervals.

An important feature in all three systems was the range of the kinetic region. As seen in Table 2, the potential ranges do not superimpose for both high throughput methods. Unfortunately, due to lack of forced mass transfer, the kinetic region for the 64-channel array is very narrow, 0.9 V to 1.0 V. In contrast, for the array fuel cell the kinetic current extended from 0.75 V to 0.9 V. Only RDE data exhibited an extended kinetic region, from 0.75 V to 1.0 V.

Finally, the time needed to run a single investigation and the time required to process a set of data are very important. The shortest time to perform both experiment and data processing was for the RDE method, although one needs to bear in mind that only one catalyst would be tested in a single measurement. The time necessary to perform measurements is longer for the 64-channel array and longest for the array fuel cell, which includes time for MEA preparation and overnight preconditioning before the testing commences. However, the most complex data processing occurred for the 64-channel array. This is connected with the large number of channels involved in the calculations.

After further development, the 64-channel array should be a good substitute for RDE, which is agreed to be one of the most reliable methods at the moment. Similarly, the array fuel cell should become a reliable tool to screen electrodes in a real fuel cell environment.

3 Future enhancements

The RDE method is already established as reliable by the community. The equipment is readily available to carry out experiments without modification of the design. One detail that can be easily modified is the ink preparation procedure. The quality of the ink and hence the electrode strictly influences the results.

Before new multi-channel systems can be more commonly applied to industrial catalyst testing, some of the elements need to be modified, enhanced or redesigned. Some suggestions for the development of 64-channel array system will be made first. The main problem with the system is corrosion of the components, such as the printed circuit board and pin spring loaded connections. All of these components are positioned underneath the PTFE plate, which has the 64 embedded vitreous carbon electrodes. The difficulty with

corrosion should be solvable by modifying the position of the electrodes, upside down to the actual design. In other words, the connections and electrodes should be situated above the cell compartment. Another suggestion to solve the problems associated with corrosion is to enhance the sealing of the cell. Many times sulphuric acid penetrated the parts and gaps between the working electrodes and the PTFE plate.

An application of elevated temperature to the array cell should be another interesting option as a way to enhance the quality of the system. The cell could then operate in a wide range of temperatures from room temperature up to 80 °C. This could be accomplished in the already existing cell prepared by heating the solution from below or by using a jacketed cell.

Similar difficulties with ink and electrode preparation as in the RDE method occurred for the 64-channel array. The quality of the ink plays a crucial role in data quality, so much attention should be put into developing more consistent inks.

The array fuel cell is the third system described in this thesis (Chapter 5). This method was very different from the previous two. The cell is much more sophisticated in its construction, operation and electrode preparation. The chances of adjusting, enhancing or modifying the cell design are much higher compared to both RDE and 64-channel array systems, whose common characteristic feature was simplicity.

One of most important components in the cell design was the gas flow rate orifice valves. Some problems occurred with increased humidity on the cathode/working electrode side with water condensation at the orifices. Therefore, a new flow control system less sensitive for humidified gases should be applied. The second key feature of the cell that should be modified is its sealing gaskets. The experiments carried out in this project were performed under too high compression of the MEA as stated in the literature [16] and the fuel cell data to which the results were compared. For the future, a range of gaskets with different thicknesses and type of material should be prepared in order to run the experiment in appropriate compression and sealing conditions. To avoid gas leakage, the ‘right’ thickness of the gasket has to be identified before the measurements commence.

The array fuel cell results were compared in Chapter 5 with standard 50 cm^2 area fuel cell data. Unfortunately, quantitative evaluation is impossible due to lack of methods of resistance estimation for the array fuel cell. The strong suggestion is to apply methods of measurement of the Nafion membrane and other cell components’ resistance such as current interrupt. This could give a better view of the results obtained and fully compare them with the other systems available on the market.

Difficulties also occurred with the temperature control system for the humidifiers. At a higher temperature (above 90 °C) after the humidifier was refilled with room temperature distilled water the temperature inside the sparger increased. A new precise water refilling system and/or larger volume humidifier is needed to stabilise the temperature and contribution of water to the array cell. Moreover, a new porous ceramic structure design inside the humidifiers should also be considered.

During measurement, problems with equal water supply to the 25 electrodes arise. Some specific regions were drier than others; hence, the poor current response of some working electrodes associated with this fact occurred. It is possible that redesign of the flow fields would help in even delivery of the humidified gases to the working electrodes.

Finally, the last common weakness of both high throughput methods is in data processing. Improved software, supporting and speeding up data calculation, needs to be developed. On the whole this should save lots of time in processing a single experiment data set.

4 Conclusions

In my personal opinion, the quality and reproducibility of the data and cost of the system play the most important roles in deciding which equipment is most useful. For sure, the great diversity of information obtained using the three methods described in this thesis should help to establish the activities and properties of the catalyst tested, but the time obstacle and limited budgets ideally demand the use of only the best one.

In terms of the cost of each particular component, both multichannel methods are very comparable. The RDE system is not much cheaper, as it costs only one-fourth less compared to both high-throughput techniques. The most expensive component of the system in each case is the potentiostat. The actual cell cost is relatively low in comparison to the potentiostat.

In my opinion, it takes too much time to use RDE as the main method of catalyst screening. I would prefer to recommend both high-throughput systems for use as standard methods for Pt based catalyst testing. However, after the problems associated with cyclic voltammetry and repeatability between separate experiments have been solved, I would suggest the array fuel cell system.

5 References

1. S. Guerin, B. E. Hayden, C. E. Lee, C. Mormiche, J. R. Owen, A. E. Russell, B. Theobald, and D. Thompsett, Journal of Combinatorial Chemistry 6:149 (2004).
2. A. D. Spong, G. Vitins, S. Guerin, B. E. Hayden, A. E. Russell, and J. R. Owen, Journal of Power Sources 119:778 (2003).
3. E. S. Smotkin, J. H. Jiang, A. Nayar, and R. X. Liu, Applied Surface Science 252:2573 (2006).
4. R. Liu and E. S. Smotkin, Journal of Electroanalytical Chemistry 535:49 (2002).
5. E. S. Smotkin and R. R. Diaz-Morales, Annual Review of Materials Research 33:557 (2003).
6. R. R. Diaz-Morales, R. X. Liu, E. Fachini, G. Y. Chen, C. U. Segre, A. Martinez, C. Cabrera, and E. S. Smotkin, Journal of the Electrochemical Society 151:A1314 (2004).
7. H. A. Gasteiger, S. S. Kocha, B. Sompalli, and F. T. Wagner, Applied Catalysis B-Environmental 56:9 (2005).
8. F. Gloaguen, P. Convert, S. Gamburzev, O. A. Velev, and S. Srinivasan, in 1997 Joint International Meeting of the International-Society-of-Electrochemistry and the Electrochemical-Society, Pergamon-Elsevier Science Ltd, Paris, France, 1997, p. 3767.
9. N. Markovic, H. Gasteiger, and P. N. Ross, Journal of the Electrochemical Society 144:1591 (1997).
10. U. A. Paulus, T. J. Schmidt, H. A. Gasteiger, and R. J. Behm, Journal of Electroanalytical Chemistry 495:134 (2001).
11. U. A. Paulus, A. Wokaun, G. G. Scherer, T. J. Schmidt, V. Stamenkovic, N. M. Markovic, and P. N. Ross, Electrochimica Acta 47:3787 (2002).
12. U. A. Paulus, A. Wokaun, G. G. Scherer, T. J. Schmidt, V. Stamenkovic, V. Radmilovic, N. M. Markovic, and P. N. Ross, Journal of Physical Chemistry B 106:4181 (2002).
13. T. J. Schmidt and H. A. Gasteiger, in Handbook of Fuel Cells - Fundamentals, Technology and Applications, Vol. 2 Electrocatalysis (W. Vielstich, Gasteiger, H. A., Lamm, A., ed.), John Wiley & Sons, 2003, p. 316 (Chapter 22).
14. T. J. Schmidt, H. A. Gasteiger, G. D. Stab, P. M. Urban, D. M. Kolb, and R. J. Behm, Journal of the Electrochemical Society 145:2354 (1998).
15. V. Stamenkovic, T. J. Schmidt, P. N. Ross, and N. M. Markovic, Journal of Physical Chemistry B 106:11970 (2002).

16. J. Ge, A. Higier, and H. Liu, Journal of Power Sources 159:922 (2006).